

SOME ISSUES RELEVANT TO  
PROPAGATION OF LIGHTWAVE SIGNALS  
IN OPTICAL FIBERS

Thesis by  
Eva M. Peral

In Partial Fulfillment of the Requirements  
for the Degree of  
Doctor of Philosophy

California Institute of Technology  
Pasadena, California  
2000

(Submitted November 24, 1999)





## ACKNOWLEDGEMENTS

It is a pleasure for me to acknowledge the support and encouragement of my advisor, Professor Amnon Yariv. He has been a continuous source of inspiration, fruitful discussions and knowledge.

I would also like to express my gratitude to the members of Prof. Yariv's research group for the stimulating environment they provided. In particular, I would like to thank Dan Provenzano, Reginald Lee and Dr. Matt McAdams, with whom I collaborated in some of the experimental work presented in this thesis, Dr. William Marshall, with whom I shared many interesting discussions, Dr. John Iannelli and Dr. T. R. Chen from Ortel Corporation, who provided many lasers and equipment for the experimental work, Dr. Danny Eliyahu and Dr. Avishay Eyal, with whom I had the pleasure to share the office as well as useful discussions, and group staff members Ali Ghafari, Kevin Cooper, the late Jana Mercado and Connie Rodriguez, for their invaluable help.

To my husband Alex, thanks for his love, his continuous support and interest in my work, and the so-many wonderful moments during these years in Pasadena. Also, thanks to my parents and my parents-in-law for their constant encouragement from overseas.

## ABSTRACT

Fiber optics is a promising technology that can enable the high bit rates and long spans that are on increasing demand. Although the fiber bandwidth is as large as several terahertz, there are several phenomena, related to both intrinsic fiber properties and characteristics of the state-of-the-art transmitters and receivers, which seriously degrade the performance of fiber communication systems, imposing limits on the transmission bandwidths and distances that can be achieved.

In this thesis, some of the issues affecting linear and nonlinear propagation in optical fiber will be theoretically and experimentally studied. Schemes for compensation of some of these phenomena or amelioration of their effects will be presented.

## TABLE OF CONTENTS

<i>Chapter I. Introduction</i> .....	1
<b>I.1 Propagation in optical fiber.</b> .....	2
<b>I.2 Dynamics of semiconductor lasers.</b> .....	3
<b>I.3 New optical components based on coupling among optical modes.</b> .....	4
<b>I.4 Outline of this thesis.</b> .....	5
<b>References</b> .....	7
<i>Chapter II. Dispersive propagation of lightwave signals</i> .....	9
<b>II.1 Small-signal theory of dispersive propagation of optical signals</b> .....	12
II.1.1 Small-signal propagation in a linear optical channel. ....	12
II.1.2 Small-signal systems description of an optical communications link.....	14
II.1.3 Small-signal propagation in optical fiber.....	16
II.1.4 Measurement of the baseband transfer function of an optical channel. ....	18
II.1.4.A Using a network analyzer. ....	18
II.1.4.B Using an electrical spectrum analyzer. ....	19
<b>II.2 Large-signal theory of propagation of directly-modulated light in dispersive fiber</b> .....	21
II.2.1 Theory .....	22
II.2.1.A 1-tone large-signal direct modulation. ....	22
II.2.1.B N-tone large-signal direct modulation.....	24
II.2.2 Simulation .....	25
II.2.3 Experiment .....	26
<b>II.3 Large-signal theory of propagation of externally-modulated light in dispersive fiber</b> .....	31

II.3.1 Theory .....	32
II.3.1.A 1-tone large-signal external modulation. ....	32
II.3.1.B N-tone large-signal external modulation. ....	33
II.3.2 Experiment .....	34
II.3.2.A Determination of the frequency dependence of the half-wave voltage.....	34
II.3.2.B Measurement of the modulation response and harmonic distortion. ....	36
<b>Appendix II.1 A more accurate and an exact large-signal theory for direct laser modulation .....</b>	<b>39</b>
<b>Appendix II.2 Intermodulation distortion in CATV systems with direct laser modulation .....</b>	<b>40</b>
<b>References .....</b>	<b>42</b>
<b><i>Chapter III. Dynamics of semiconductor lasers and effect of dispersive propagation .....</i></b>	<b>45</b>
<b>III.1 Precise measurement of semiconductor laser chirp using the effect of propagation in dispersive fiber .....</b>	<b>47</b>
III.1.1 Introduction .....	47
III.1.2 Theory .....	47
III.1.3 Description of methods .....	48
III.1.3.A Previous method for measuring the laser chirp [1]-[5].....	48
III.1.3.B Precise method for measuring the laser chirp [7] .....	49
III.1.4 Experiment .....	51
III.1.5 Application: transmission through fiber gratings .....	56
<b>III.2 Characterization of laser chirp for multi-quantum-well distributed-feedback lasers.....</b>	<b>59</b>
III.2.1 Analysis of the FM response of DFB lasers including longitudinal spatial hole burning. ....	60
III.2.1.A Theory of operation of DFB lasers. ....	60

III.2.1.B Characterization of DFB lasers using amplified spontaneous emission below threshold. ....	63
1) Theory of amplified spontaneous emission below-threshold.....	63
2) Modified Hakki-Paoli method for DFB lasers.....	64
3) Determination of laser parameters from ASE.....	66
III.2.1.C Experiment.....	67
III.2.2 Analysis of the FM response of MQW lasers including carrier transport and capture. ....	72
III.2.2.A Reservoir model for MQW lasers .....	73
1) Intensity modulation response.....	75
2) Frequency modulation response.....	76
3) Phase to intensity modulation index ratio.....	77
4) Linewidth. ....	77
5) Discussion. ....	78
III.2.2.B Experiment .....	79
<b>III.3 Effect of many weak side modes on relative intensity noise of distributed feedback semiconductor lasers.....</b>	<b>83</b>
III.3.1 Theory.....	83
III.3.2 Experiment.....	90
<b>III.4 Reduction of laser RIN and reshaping of modulation response using a fiber bragg grating. ....</b>	<b>94</b>
III.4.1 Theory.....	94
III.4.2 Experiment.....	96
<b>Appendix III.1 Comparison of modulation response and interferometer techniques for determination of laser chirp.....</b>	<b>101</b>
<b>References .....</b>	<b>103</b>

<i>Chapter IV. Nonlinear fiber propagation: effect of stimulated Brillouin scattering</i> .....	111
<b>IV.1 Scalar theory of the acoustooptic interaction in optical fiber.</b> .....	113
IV.1.1 Acoustic wave equation.....	114
IV.1.2 Acoustooptic interaction.....	116
IV.1.3 Numerical simulation.....	119
<b>IV.2 Effect of SBS on modulation response</b> .....	122
IV.2.1 Theory .....	122
IV.2.1.A Small-signal theory.....	122
IV.2.1.B Quasi-large-signal theory.....	123
IV.2.2 Experiment.....	124
IV.2.2.A Experimental set-up. ....	124
IV.2.2.B Small-signal experiments .....	125
IV.2.2.C Quasi-large-signal experiments .....	127
<b>IV.3 Effect of SBS on relative intensity noise</b> .....	130
IV.3.1 Theory. ....	130
IV.3.2 Experiment.....	131
<b>Appendix IV.1 Vector theory of the acoustooptic interaction in optical fiber</b> ...	135
<b>Appendix IV.2 Some useful integrals</b> .....	140
<b>References</b> .....	141
<i>Chapter V. New schemes of mode conversion</i> .....	143
<b>V.1 Supermodes of multimode waveguide structures.</b> .....	144
V.1.1 Introduction .....	144
V.1.2 Generalized coupled mode theory.....	145
V.1.3 On supermodes, orthogonality and power conservation.....	148
V.1.3.A Non grating-assisted coupling among the forward-propagating modes of several single-mode waveguide.....	149

1) Supermodes. ....	149
2) Orthogonality of supermodes. ....	150
3) Power conservation. ....	152
V.1.3.B Grating-assisted coupling among modes in one multimode waveguide. ....	152
1) Supermodes. ....	152
2) Supermode orthogonality and power conservation. ....	153
<b>V.2 Mode conversion between copropagating modes via a mediating mode. ...</b>	<b>154</b>
V.2.1 Principle of operation. ....	157
V.2.2 Adiabatic mode conversion mediated by a forward propagating mode. ....	159
V.2.2.A Theory.....	159
V.2.2.B On the adiabaticity condition.....	160
V.2.2.C Simulation. ....	162
1) Optical switch.....	167
2) Wavelength-selective coupler .....	169
V.2.3 Non-adiabatic mode conversion mediated by a Bragg backward propagating mode. ....	170
V.2.3.A Theory.....	170
V.2.3.B On the adiabaticity condition.....	173
V.2.3.C Simulation. ....	175
<b>References.....</b>	<b>178</b>

## LIST OF ILLUSTRATIONS

<i>Chapter II. Dispersive propagation of lightwave signals</i> .....	9
Figure 1: IM/DD system with direct-modulation of the semiconductor laser light. ....	10
Figure 2: IM/DD system with external-modulation of the semiconductor laser light. ....	10
Figure 3: Transfer function description of an optical communications system. ....	15
Figure 4: Experimental setup for measuring the system response with a network analyzer. ....	18
Figure 5: Experimental setup for measuring the system response with an electric spectrum analyzer. ....	19
Figure 6: Numerical simulations of fiber modulation transfer function after propagation in 85 km of fiber for different modulation indices. Dashed from Eq. (39), dotted from Eq. (56) and solid is exact. Curve for $m_{IM}=0.1$ nearly coincides with small-signal approximation Eq. (19).....	26
Figure 7: (a) Intensity modulation index measured at the laser output for several modulation powers. (b) Fiber modulation transfer function after propagation in 85km of fiber for the same modulation powers as in Figure 7a. Solid curve is theory. ....	28
Figure 8: Experimentally detected power in signal (circles), second harmonic (crosses) and third harmonic (squares) normalized by the power in the optical carrier, (a) at the laser output, (b) after propagation in 85 km of fiber. Solid curve is theory. ....	29
Figure 9: Experimentally detected normalized power in dBc for 2-tone modulation at the laser output at $\Omega_1$ (open triangles) and $\Omega_2=0.9\Omega_1$ (open circles) and after propagation in 50km of fiber at $\Omega_1$ (solid triangles), $\Omega_2$ (solid triangles) and $\Omega_1-\Omega_2$ (solid squares). Solid curve is theory.....	30



Figure 10: Experimental set-up for measuring the frequency dependence of the half-wave voltage for an EO-MZM. SG=Signal generator, ESA=electrical spectrum analyzer, A=ampmeter, PC=personal computer. ....	35
Figure 11: Measured half-wave power of EO-MZM as a function of the modulation frequency. ....	36
Figure 12: Experimental set-up for measuring the modulation response and harmonic distortion for externally-modulated light after propagation in fiber. ....	37
Figure 13: Experimentally detected power normalized by the power in the optical carrier at the modulator output in signal (empty circles) and third harmonic (empty squares), and after propagation in 105 km of fiber at signal (solid circles) and second harmonic (solid triangles). Solid curve is theory.....	38

***Chapter III. Dynamics of semiconductor lasers and effect of dispersive propagation*** ..... 45

Figure 1: Experimental change in modulation response after 2.3km (circles) and 50.5km (triangles) of fiber. The parameters $\kappa$ and $\alpha$ are determined that best fit the change in modulation response after 2.3 km (solid), 50.5 km (dashed) and both lengths of fiber (dotted). Output power at laser facet is 14.3mW... ..	52
Figure 2: Real (circles) and imaginary (triangles) part of $\kappa(\Omega)$ with $\alpha=-4.43$ obtained from $ H(\Omega, z) ^2$ for different combinations of fiber. Solid and dashed are the result from using magnitude and phase of $H(\Omega, z)$ . Output power at laser facet is 14.3mW. ....	54
Figure 3: Real (circles) and imaginary (triangles) part of $\kappa(\Omega)$ at several laser output powers obtained from magnitude and phase of $H(\Omega, z)$ . $\alpha$ takes the values -4.37,-4.39,-4.43,-4.58,-4.57 with increasing output power. Solid corresponds to the theory in section III.2.2. ....	55

Figure 4: Measured $\kappa(\Omega)$ after 2.3km (circles), 11.1km (squares) and 50.5km (triangles) of standard fiber together with theoretical prediction (solid) using $\kappa(\Omega)$ in Figure 3. Output power at laser facet is 14.3mW. ....	57
Figure 5: Baseband transfer function after transmission through fiber grating predicted using the measured $\kappa(\Omega)$ in Figure 3 (solid) and constant $\kappa$ and $\alpha$ (dashed) compared to measurement (circles).....	58
Figure 6: DFB laser structure. ....	60
Figure 7: Flow chart for determination of laser parameters from measurements of below threshold ASE spectrum.....	67
Figure 8: Below threshold ASE spectrum at bias currents 14mA (circles) and 17mA (triangles). Solid is theory. ....	68
Figure 9: Gain spectrum at several bias currents.....	69
Figure 10: Logarithmic maximum gain-current relation. ....	69
Figure 11: Spatial dependence of the carrier density normalized by the carrier density at threshold for several bias currents.....	70
Figure 12: Spatial dependence of the photon density and the forward and backward field amplitudes normalized by the photon density at the left facet. Bias current is 85mA. ....	71
Figure 13: Real (circles) and imaginary (triangles) part of $\kappa(\Omega)$ at several bias currents. We assumed $\alpha_N = -4.5$ at all bias currents.....	71
Figure 14: Reservoir model for quantum well lasers. ....	72
Figure 15: Coefficients from fitting $\kappa(\Omega)$ in Figure 3 to polynomial in equations (50). ....	80
Figure 16: Measured $\xi\tau_{cap}$ for three MQW-DFB lasers with different threshold intensities.....	81
Figure 17: Linewidth enhancement factor as determined from $c_0$ (circles), $c_1$ (squares), RIN after fiber (triangles) and linewidth (diamonds). The inset shows the measured linewidth, and the expected linewidth (solid) with power independent $\alpha_N$ . ....	82

Figure 18: RIN at laser output (crosses) and after 4.4 km and 25.3 km of fiber (circles). The laser output power is  $P_{out}=3.4\text{mW}$ ,  $I_{bias}=1.6I_{th}$  and SMSR=27dB. The solid curve is the multimode (MM) theory and the dashed curve is the single-mode (SM) theory.....90

Figure 19: RIN after 4.4 km of fiber. The laser output power is  $P_{out}=16.4\text{mW}$ ,  $I_{bias}=4.1I_{th}$  and SMSR=39dB. Same notation as in Figure 18. ....91

Figure 20: Measured optical spectrum at  $P_{out}=3.4\text{mW}$  (solid) and  $P_{out}=16.4\text{mW}$  (dashed) vs. wavelength.....92

Figure 21: Side mode suppression ratio at  $P_{out}=3.4\text{mW}$  (circles) and  $P_{out}=16.4\text{mW}$  (crosses) vs. frequency deviation from the main mode.....93

Figure 22: Reflection spectrum around the laser optical frequency.....97

Figure 23: Laser RIN and modulation response at 50mA bias current. ....99

Figure 24: Laser RIN and modulation response at 110mA bias current. ....100

Figure 25: Real and imaginary part of  $\kappa(\Omega)$  obtained from modulation response (solid and dotted, respectively) and from optical spectrum side bands (circles and triangles, respectively).....102

**Chapter IV. Nonlinear fiber propagation: effect of stimulated Brillouin scattering..... 111**

Figure 1: Generation of an acoustic wave with frequency  $\Omega_B$  traveling at the speed of sound,  $v_s$ , and a backward propagating optical wave, downshifted by  $\Omega_B$  from the incident wave by the process of stimulated Brillouin scattering.....114

Figure 2: Dispersion map of longitudinal acoustic modes for  $v_l / v_t = 1.6032$  .....119

Figure 3: Normalized overlap integral between the optical and acoustic modes,  $\frac{\beta}{\omega\mu} a_{cl} \langle E_0^2, \rho_n \rangle$ , as a function of the (arbitrary) mode number,  $n$ , for three different values of the normalized frequency,  $\Omega_s a_{cl} / v_l$ . ....120

Figure 4: Real and imaginary part of the normalized gain,  $\frac{g_B A_{eff}}{g_{B0}}$ , for  $\nu_l / \nu_s = 1.6032$  as a function of deviation in frequency from that of maximum Brillouin gain,  $\Omega_{s,max}$ . ..... 121

Figure 5: Experimental set-up. LD=laser diode, L=variable optical attenuator, OMM=optical multimeter, PD=photodetector, NA=network analyzer, ESA=electric spectrum analyzer. .... 125

Figure 6: Change in modulation response,  $|H(\Omega, z)|^2$ , for 50 km of fiber, -28dBm modulation power, and several launched powers into the fiber. Diamonds is measured  $|H(\Omega, z)|^2$  in the absence of nonlinear effects. Solid is theory. .... 126

Figure 7: Left axis: forward (solid) and backscattered (dashed) optical powers for 50 km of fiber. Right axis: nonlinear phase change (solid is experimental, dotted is theoretical prediction as described in text)..... 127

Figure 8: (a) Change in modulation response,  $|H(\Omega, z)|^2$  and (b) received power, as function of modulation frequency for 50km of fiber, 18mW of launched optical power and several modulation powers. Diamonds is measured data in the absence of nonlinear effects. Solid is theory. The inset in (a) shows  $|H(\Omega, z)|^2$  in an extended frequency range for 18mW optical power (triangles) and linear regime (solid) with 0dBm modulation power..... 129

Figure 9: Relative intensity noise (RIN) for 25 km of fiber and several launched powers into the fiber. Solid line is theory. The inset shows the nonlinear phase change as a function of launched power..... 131

Figure 10: RIN of forward, (a) and (b), and backward, (c) and (d), propagating waves after 50 km of fiber at low frequencies, (a) and (c), and around  $\Omega_B$ , (b) and (d). The laser light was directly modulated at 300MHz with modulation powers (MP) -20dBm (circles) and -10dBm (triangles)..... 132

Figure 11: Factor  $|\gamma_r|^2 |c_n|^2$  derived from the measured RIN power of the backward propagating field at the fiber input at  $\Omega_B + n\Omega$  as a function of modulation frequency,  $\Omega/2\pi$ , for two different modulation powers (MP) after 75 km of fiber. The dashed line is obtained with  $|\gamma_r|^2 = -35.5$  dB and  $|c_n|^2$  as determined from the laser chirp and modulation power. .... 134

**Chapter V. New schemes of mode conversion ..... 143**

Figure 1: Adiabatic mode converter in adjacent waveguides through the evanescent fields.....156

Figure 2: Mode converter mediated by backward Bragg scattering.....156

Figure 3: Mode power (bottom plots) on two-photon resonance, i.e.,  $\beta_a = \beta_c$ , as a function of the detuning between mode A and B for the two coupling coefficients displayed in the upper plots. Input mode A is solid, mediating mode B is dotted and output mode C is dashed curve. ....163

Figure 4: Power in input mode A (bottom left) and output mode C (bottom right) on two-photon resonance, i.e.,  $\beta_a = \beta_c$ , as a function of the detuning between mode A and B for the coupling coefficients displayed in the upper plot. All coupling coefficients have the same shape and area, but different overlap. The number in the upper plot is the ratio between  $\kappa_{cb}$  and  $\kappa_{ab}$  at the point where  $\kappa_{ab}$  is maximum for the different coupling coefficients. ....164

Figure 5: Contour plots of mode power in input mode A (a), mediating mode B (b) and output mode C (c) as a function of detuning between A and B (horizontal axis) and detuning between A and C (vertical axis).....167

Figure 6: Mode power in modes A (circles), B (triangles) and C (squares) for  $\beta_a = \beta_c$  (empty), and  $\beta_a \neq \beta_c$  (solid). (a) is for  $\beta_c L - \beta_a L = 12.5$  and (b) is for

- $\beta_c L - \beta_a L = 25$ . The coupling coefficients are those on the left upper plot in Figure 3. ....169
- Figure 7: Spatial evolution of mode power for adiabatic grating-assisted mode converter on resonance for several coupling strengths. Mode A is solid, mode B is dotted and mode C is dashed curve. The upper plot shows the coupling coefficients..176
- Figure 8: Contour plot of the reflection coefficient (in dB) at the input of a uniform grating-assisted mode converter with  $\kappa_{cb} L = \kappa_{ab} L = 20$ . The thick solid line indicates the boundary of the forbidden region. ....177

## GLOSSARY OF SYMBOLS

$A_k$	amplitude of waveguide mode $k$
$\hat{A}_k$	amplitude of supermode $k$
$a$	vector of waveguide mode amplitudes $a_k$
$a_k$	amplitude of waveguide mode $k$ when oscillatory term is removed
$a_1$	electric field envelope amplitude of forward-propagating wave
$a_2$	electric field envelope amplitude of backward-propagating wave
$a_{cl}$	radius of the acoustic guide
$a(\Omega)$	thermal noise coefficient in noise spectrum
$B$	diagonal matrix of waveguide mode propagation constants
$\hat{B}$	diagonal matrix of supermode propagation constants
$B_N$	noise bandwidth
$b(\Omega)$	shot noise coefficient in noise spectrum
$b_n(z, t)$	acoustic wave mode coefficients
$c$	elastic stiffness tensor
$c_n$	electric field sideband amplitudes
$c(\Omega)$	excess noise coefficient in noise spectrum
$D$	diagonal matrix of reference detunings
$D$	diffusion coefficient
$D_0(\Omega)$	laser dynamics resonant denominator for bulk laser
$\mathbf{E}$	electric field vector
$E_A$	canonical vector for mode A in mode converter
$E_B$	canonical vector for mode B in mode converter
$E_C$	canonical vector for mode C in mode converter

$\hat{E}_k$	eigenvector for supermode $k$
$\tilde{E}_B$	complex time-dependent envelope of backward propagating wave in fiber
$E_0(r)$	transverse distribution of the fundamental mode in single mode optical fiber
$\tilde{E}(t, z)$	time-varying electric field propagating in an optical channel
$\bar{E}_k(x, y)$	transverse profile of waveguide mode $k$
$\bar{\bar{E}}_k(x, y)$	transverse profiles of supermode $k$
$\bar{E}_k(x, y, z, t)$	time-varying vectorial electric field in waveguide
$e$	electron charge
$\hat{e}_1$	unit vectors in the direction of the forward propagating fields
$\hat{e}_2$	unit vectors in the direction of the backward propagating fields
$K$	matrix of coupling coefficients
$k_0$	wavevector in free space
$k_n$	longitudinal propagation constant of the acoustic modes
$k_{ln}$	transverse propagation constant of the acoustic modes
$k_s$	wavevector of acoustic wave
$F_N$	Langevin carrier noise source
$F'_N$	Langevin carrier noise source uncorrelated with photon noise
$F_P$	Langevin photon noise source
$F_{P_i}$	Langevin photon noise source in mode $i$
$F_\phi$	phase Langevin noise source
$F_{\phi_i}$	Langevin phase noise source in mode $i$
$G$	stimulated recombination rate



$G_N$	differential gain
$G_{N_i}$	differential gain for mode $i$
$G_P$	gain compression
$g$	laser material gain
$g_B$	Brillouin power gain
$H$	system matrix describing multimode waveguide structure
$H_{ad}$	adiabatic system matrix in mode converter
$H(\Omega, z)$	baseband transfer function
$H_e(\Omega, z)$	conjugate-symmetric part of $t(\omega)t^*(\omega_0)$ around $\omega_0$
$H_o(\Omega, z)$	conjugate-antisymmetric part of $t(\omega)t^*(\omega_0)$ around $\omega_0$
$H_T(\Omega, z)$	total baseband transfer function including receiver and transmitter response
$H_{Tx}(\Omega)$	transmitter response function
$H_{Rx}(\Omega)$	receiver response function
$I$	laser current injection
$I_{bias}$	laser bias current
$I_{DC}(z)$	DC photocurrent
$I_{in}(\Omega)$	modulation current input in transmitter
$I_{out}(\Omega, z)$	received current at after receiver electronics
$\tilde{I}(t, z)$	time-varying detected photocurrent
$\text{Im}\{x\}$	imaginary part of $x$
$J_n$	Bessel functions of order $n$
$k_B$	Boltzmann's constant
$L$	laser cavity length
$L_{DC}$	DC grating insertion loss

$L_{eff}$	fiber effective length
$L_{SCH}$	length of the SCH region
$L(\Omega, z)$	frequency dependent loss in propagation
$L_{DC}(z)$	DC loss in propagation
$L_{Lin}(z)$	linear fiber loss in propagation
$L_{NL}(z)$	nonlinear fiber loss due to SBS
$m_{IM}$	intensity modulation index
$m_{FM}$	frequency modulation index
$m_l$	Fourier coefficients of laser IM response
$N$	number of waveguide modes
$N_b$	unconfined carrier density
$N_{th}$	carrier density at threshold
$N_w$	confined carrier density
$N(t, z)$	carrier density
$N_n(\Omega)$	number of beats for intermodulation product order $n$
$n'$	real part of the effective modal refractive index
$n''$	imaginary part of the effective refractive index
$n_0$	fiber modal index
$n_g$	group index
$n_k$	refractive index of the isolated and unperturbed waveguide $k$
$n_{sp}$	spontaneous emission factor
$n(x, y, z)$	refractive index of the perturbed dielectric structure
$P_0$	average optical power
$\bar{P}_0$	integrated power of forward propagating wave in fiber

$P_S$	power of backreflected Stokes wave
$\mathbf{P}^{NL}$	nonlinear polarization vector
$P(t, z)$	photon density
$P_N(\lambda)$	laser spontaneous emission noise power
$P_N(\Omega)$	electrical noise spectrum
$PIR_{F_p}(\Omega)$	PIR corresponding to photon noise source
$PIR_{\Delta I}(\Omega)$	PIR corresponding to modulation current
$\mathbf{p}$	strain-optic tensor
$Q(\lambda)$	Q-function in modified Hakki-Paoli method
$R$	matrix of overlap coefficients
$R$	parameter appearing in modified Hakki-Paoli method
$R_2$	magnitude of the reflection coefficient at the right facet
$R(\Omega)$	photodiode responsivity
$R_{sp_i}$	spontaneous emission rate per unit volume into the mode $i$
$R^\pm(t, z)$	complex amplitudes of the forward (+) and backward (-) propagating waves in DFB laser structure
$r$	radial coordinate in a cylindrical coordinate system
$r_1$	laser left facet complex facet reflectivity
$r_2$	laser right facet complex facet reflectivity
$\text{Re}\{x\}$	real part of $x$
$S$	diagonal matrix of sign indicating power flux direction
$s_k$	propagation sign of mode $k$ ; equals +1 for forward propagating modes and -1 for backward propagating modes
$T$	Kelvin temperature
$t(\omega)$	transmission coefficient of optical filter
$\mathbf{u}(\mathbf{r}, t)$	acoustic particle displacement vector

$V$	laser volume
$V_\pi$	half-wave voltage of the EO-MZM
$V_{QW}$	volume of the quantum wells
$V_{SCH}$	volume of the SCH region
$V(t)$	voltage applied to the EO-MZM
$v$	amplitude of the modulation tone applied to EO-MZM normalized by $V_\pi$
$v_0$	DC bias applied to EO-MZM normalized by $V_\pi$
$v_g$	group velocity
$v_l$	longitudinal sound velocity
$v_t$	transverse sound velocity
$W$	Wronskian
$w$	fiber mode beam waist
$Z_1(z)$	Green function satisfying left boundary condition
$Z_2(z)$	Green function satisfying left boundary condition
$z$	propagation distance (in general, it indicates optical channel output)
$\alpha$	linewidth enhancement factor
$\alpha_f$	fiber power attenuation coefficient
$\alpha_i$	linewidth enhancement factor for mode $i$
$\alpha_m$	laser material background loss
$\alpha_N$	linewidth enhancement factor (as defined by Henry)
$\alpha_p$	Agrawal's parameter related to refractive index change due to change in photon density
$\beta''$	first-order group velocity dispersion parameter
$\beta_1$	inverse of the group velocity,

$\beta_1$	propagation constant of forward-propagating wave
$\beta_2$	first-order group velocity dispersion parameter
$\beta_2$	propagation constant of backward-propagating wave
$\beta_3$	second-order group velocity dispersion parameter
$\beta_i$	self-gain compression coefficient for mode $i$
$\beta_k$	propagation constants of the waveguide mode $k$
$\hat{\beta}_k$	propagation constant of supermode $k$
$\beta(\omega)$	propagation constant
$\Delta E$	energy separation of the quasi-Fermi level between the conduction and valence band
$\Delta I$	small-signal modulation current
$\Delta I_Q(\Omega)$	effective current injection into QW's
$\Delta N$	carrier density variation
$\Delta N_b$	small-signal unconfined carrier density variation
$\Delta N_w$	small-signal confined carrier density variation
$\Delta P$	small-signal photon density variation
$\Delta P_i$	photon density variation in mode $i$
$\Delta \phi_i$	phase density variation in mode $i$
$\Delta \omega$	small-signal frequency variation
$\Delta \omega$	deviation of the optical frequency from the Bragg frequency
$\Delta \tilde{\omega}$	complex angular frequency deviation
$\Delta \varphi$	dephasing angle between FM and IM
$\delta$	deviation of the propagation constant from the Bragg condition
$\delta_k$	reference detunings
$\delta_{jk}$	detuning from Bragg condition
$\varepsilon$	optical dielectric constant tensor

$\varepsilon$	gain compression parameter
$\Phi(x, y)$	laser cavity field transverse profile
$\Gamma$	optical confinement factor
$\Gamma_s$	acoustic-wave damping factor
$\Gamma_{sch}$	confinement factor of the unconfined carriers
$\Gamma_w$	confinement factor of the confined carriers
$\gamma$	electrostriction tensor
$\gamma$	electrostrictive coefficient
$\gamma_0$	laser damping coefficient
$\gamma_R$	field reflection coefficient due to Rayleigh scattering viscosity tensor
$\eta_V$	ratio between SCH volume and QW volume
$\varphi$	angular coordinate in a cylindrical coordinate system
$\varphi$	parameter appearing in modified Hakki-Paoli method
$\varphi_{IM}$	intensity modulation phase angle
$\varphi_{FM}$	frequency modulation phase angle
$\varphi(\Omega, z)$	propagation delay angle
$\kappa$	cross-over frequency between adiabatic and transient chirp regimes
$\kappa_g^\pm$	coupling coefficients of DFB laser structure
$\tilde{\kappa}_{jk}$	waveguide coupling coefficient
$\kappa_{jk}$	waveguide coupling coefficient when oscillatory term is removed
$\Lambda_{jk}$	period of quasi-periodic perturbation coupling modes $k$ and $j$
$\lambda$	Lamé's constant
$\lambda_{Bragg}$	Bragg wavelength
$\mu$	Lamé's constant
$\theta$	parameter appearing in modified Hakki-Paoli method

$\theta_{ij}$	gain compression for mode $i$ due to mode $j$
$\theta_{NL}$	nonlinear phase change due to SBS
$\theta(\Omega, z)$	dispersion angle
$\rho$	material density variation
$\rho_0$	material density
$\rho_{jk}$	overlap coefficient
$\rho_n(r, \varphi)$	acoustic wave modes
$\sigma(\mathbf{r}, t)$	strain tensor
$\tau(\mathbf{r}, t)$	stress tensor
$\tau_b$	differential carrier lifetime for unconfined carriers
$\tau_c$	differential carrier lifetime
$\tau_{cap}$	effective capture time
$\tau_{cap}^Q$	intrinsic quantum capture time
$\tau_{esc}$	effective escape time
$\tau_{esc}^Q$	intrinsic quantum escape time
$\tau_g$	group delay
$\tau_{ph}$	photon lifetime
$\tau_w$	differential carrier lifetimes for confined carriers
$\tau_Q(\Omega)$	effective non-radiative recombination time due to the finite effective capture time
$\Omega$	angular modulation frequency
$\Omega_{IMP}$	frequency of a given intermodulation product
$\Omega_s$	acoustic wave angular frequency
$\Omega_{s, \max}$	acoustic wave angular frequency for maximum Brillouin gain

$\Omega_0$	laser relaxation frequency
$\omega_0$	optical frequency
$\xi$	ratio between refractive index change due to change in confined and unconfined carrier density
$\nabla_s$	symmetric part of the displacement gradient
$\nabla_t^2$	Laplacian acting on the transverse coordinates



## GLOSSARY OF ABBREVIATIONS


Aampmeter

AM	amplitude modulation
ASE	amplified spontaneous emission
CATV	common-antenna television (or cable television)
DFB	distributed feedback
EO-MZM	electrooptic-Mach Zehnder modulator
ESA	electric spectrum analyzer
FM	frequency modulation
FP	Fabry-Perot
FWM	four-wave mixing
IM	intensity modulation
IMD	intermodulation distortion
IMP	intermodulation product
LD	laser diode
MQW	multi-quantum well
MR	modulation response
NA	network analyzer
OMM	optical multimeter
PC	personal computer
PD	photodetector
QW	quantum well
RIN	relative intensity noise
RINP	RIN power
SBS	stimulated Brillouin scattering
SCH	separate confinement heterostructure
SG	signal generator

SMSR	side mode suppression ratio
SPM	self-phase modulation
SRS	stimulated Raman scattering
XPM	cross-phase modulation

# Chapter I.

## Introduction

 Fiber-optic communications systems use high carrier frequencies ( $\sim 100\text{THz}$ ) in the near-infrared region to transmit information over distances ranging from a few kilometers to several hundreds or even thousands of kilometers. Two breakthroughs contributed to the success of the new technology: the invention of the laser during the 1960s [1] and the reduction of the fiber loss to about 20 dB/km in the wavelength region near  $1\mu\text{m}$  in 1970 [2]. The simultaneous availability of a reliable optical source and a low-loss optical guiding medium led to a rapid development of lightwave communication systems, and the first generation of fiber-optic systems operating near  $0.8\mu\text{m}$  began to be deployed in 1978 [3].

The two main limitations of these first lightwave systems were fiber loss and dispersion. Further development of new laser sources and improvement of optical fiber transmission properties has enabled several-orders-of-magnitude increase in the bit rate-distance product over a period of 20 years. Thus, InGaAsP lasers and detectors were developed operating in the wavelength regions near  $1.3\mu\text{m}$  and  $1.55\mu\text{m}$  where the fiber loss is minimum. The problem of modal dispersion was overcome by the use of single-mode fibers and nearly-single-mode lasers, although group velocity dispersion remains an important issue. Recently, the invention of new optical devices such as optical fiber amplifiers and fiber Bragg gratings has further enhanced the capabilities of lightwave systems.

This thesis deals with the study of the propagation characteristics of light produced by semiconductor lasers in optical fiber. For this purpose, the dynamics of semiconductor lasers need to be well understood. In fact, the transmission properties in optical fiber also reveal important features of the semiconductor laser physics. In addition, some new components based on coupling among several waveguide modes are proposed and a theory is developed to describe their operation.

## **I.1 PROPAGATION IN OPTICAL FIBER.**

In the second communications window around  $1.3\mu\text{m}$ , the fiber loss is typically  $0.4\text{dB/km}$ . Furthermore, optical fibers exhibit minimum dispersion in this wavelength region. Despite this advantage, communication systems are migrating towards the third communications window at wavelengths near  $1.55\mu\text{m}$  where silica fiber loss exhibits a global minimum (typically  $0.2\text{dB/km}$ ). Another factor that has largely contributed to the deployment of systems operating at  $1.55\mu\text{m}$  is the invention of the erbium-doped fiber amplifier (EDFA), for which there is no ready equivalent at  $1.3\mu\text{m}$ .

The dispersion problem at  $1.55\mu\text{m}$  can be overcome by using dispersion-shifted fibers designed to have minimum dispersion at  $1.55\mu\text{m}$ . However, the huge number of kilometers of standard single-mode fiber already deployed make it a practical necessity to devise ways to deal with the group velocity dispersion. The consequences of fiber dispersion are especially severe with frequency chirping of the lightwave signal. Chirp-free external modulators can be used to combat this degradation.

Once the fiber loss cannot be further reduced, the other way to enhance the repeater spacing is to increase the launched optical power in the fiber. This can be achieved by the use of high-power lasers and also of power-booster optical amplifiers. As a consequence of these high optical powers nonlinear effects can become important. Even though fused silica has very small nonlinear coefficients compared with other common nonlinear media, nonlinear effects can be observed at relatively low optical

powers due to the small fiber spot size and extremely low fiber loss. Fiber nonlinearities can result in degradation of the propagation characteristics of lightwave signals. It has become necessary in state-of-the-art systems to assess the extent of this degradation and to devise methods to combat it.

The lowest-order elastic nonlinear effects in optical fiber originate from the third-order susceptibility, which is responsible for phenomena such as self-phase modulation (SPM), cross-phase modulation (XPM) and four-wave mixing (FWM). A second class of nonlinear effects results from stimulated inelastic scattering in which the optical field transfers part of its energy to the non optical excitations in the medium. Two important phenomena in this category are stimulated Raman scattering (SRS) and stimulated Brillouin scattering (SBS), both of which are related to vibrational excitation modes of silica. The main difference between them is that optical phonons participate in SRS whereas acoustic phonons participate in SBS.

## **I.2 DYNAMICS OF SEMICONDUCTOR LASERS.**

Most fiber-optic communication systems use semiconductor lasers as an optical source due to their compact size, high efficiency, good reliability, emission at the communications wavelengths, small area compatible with that of single-mode fiber, and possibility of direct modulation at relatively high frequencies. Nearly-single-mode operation can be achieved by using a distributed feedback structure. In addition, superior performance can be obtained with quantum well lasers, which have lower threshold current, high modulation speed, low chirp and narrow linewidth.

There is a fundamental relationship between the gain and refractive index of a semiconductor medium. The index changes that accompany modulation of gain in a laser result in frequency modulation, which is referred to as laser chirp. This frequency modulation has major consequences in the laser intensity modulation response after propagation in a dispersive optical channel. Dispersive propagation results in part of the frequency modulation (FM) converted into intensity modulation (IM). Depending on the

amount of dispersion, the FM can either add to or subtract from the IM, resulting in either enhancement or reduction of the intensity modulation response. This analysis is valid for variations in gain due to both current injection modulation and noise processes. The effect that dispersion has on the laser intensity modulation response and intensity noise can thus be used to improve the laser transmission characteristics by enhancing the intensity modulation response and reducing the laser intensity noise.

In addition, the laser chirp is closely related to the physics of the semiconductor lasers and in particular to different damping mechanisms affecting the laser dynamics. These include spectral hole-burning, carrier heating, quantum capture, carrier diffusion and spatial hole-burning. Precise measurements of laser chirp can lead to better characterization of these mechanisms.

### **I.3 NEW OPTICAL COMPONENTS BASED ON COUPLING AMONG OPTICAL MODES.**

Basic communication systems simply consist of transmitter, channel and receiver. However, other capabilities are necessary for the operation of more complicated networks, such as routing and switching. Although these can be performed in the electrical format, there is an advantage in reducing the electronics to a minimum and performing these functions in the optical domain. Most of the devices that achieve these operations, as well as others even more basic such as modulation and filtering, are based on coupling between the different optical modes that can propagate in one or several optical waveguides.

The general principle of operation is as follows. Optical waveguides can confine optical energy in one or more optical modes. Two different modes may couple with each other to exchange their energy under proper conditions. This energy exchange can have a frequency dependence, which leads to filtering of the signals travelling in each mode. In addition, the coupling strength can be affected by electrical signals in electrooptic

materials and by optical signals in nonlinear materials. This can be used to build electrically-controlled or optically-controlled modulators and optical switches.

## I.4 OUTLINE OF THIS THESIS.

In Chapter II, linear propagation of lightwave signals in dispersive channels is discussed. The simple small-signal theory of propagation is extended to treat large-signal propagation in optical fiber, which more closely approximates the conditions in practical systems. The theory is applied to light produced by direct modulation of semiconductor lasers [4] and systems using external modulation of the laser light. The degradations resulting from fiber first-order group-velocity dispersion are highlighted.

In Chapter III, the models developed in the previous chapter are applied to the characterization of the laser dynamics and also to the development of new techniques to improve the laser transmission properties. First, a method is presented to accurately measure the laser chirp using propagation in fiber [5], and a model is developed including the different damping mechanisms in distributed-feedback multi-quantum-well lasers that explains the measurement [6]. Then, the fiber propagation theory is applied to the characterization of laser noise. It is shown that the many weak side modes that always accompany the main mode of nearly-single-mode DFB lasers contribute to an enhancement of the laser noise that is not predicted by single-mode theories [7]. Finally, some earlier results on the effect of fiber Bragg gratings on modulation response [8] and noise [9] are extended to demonstrate that a properly designed fiber grating can produce major reduction of the laser intensity noise and at the same time shape the modulation response in an almost arbitrary way [10].

Chapter IV deals with the effect of stimulated Brillouin scattering (SBS) on the intensity modulation and noise characteristics after fiber propagation. It will be shown that in addition to a power loss, SBS can induce a phase shift of the optical carrier relative to its sidebands. This phase shift can lead to severe distortion of the modulation response and increase in intensity noise (RIN) [11].

In Chapter V, a new approach for mode conversion between copropagating modes is proposed. In this device the coupling is mediated by a third mode. This additional mode gives additional flexibility and as a result the devices are less sensitive to fabrication parameters compared to other devices. Low insertion loss and low polarization sensitivity can be obtained. The mode of operation of this device is theoretically explained by using a generalized coupled mode theory [12]-[13].



## REFERENCES

- [1] T. H. Maiman, *Nature*, 187, pp. 493, 1960.
- [2] F. P. Kapron, D. B. Keck, R. D. Maurer, *Appl. Phys. Lett.*, 17, pp. 423, 1970.
- [3] T. C. Cannon, D. L. Pope, D. D. Sell, *IEEE Trans. Commun.*, 26, pp. 1045, 1978.
- [4] E. Peral, A. Yariv, "Large-signal theory of the effect of dispersive propagation on the intensity modulation response of semiconductor lasers," *to be published in J. Lightwave Technol.* Presented at CLEO'99 (Baltimore, Maryland).
- [5] E. Peral, W. K. Marshall, A. Yariv, "Precise measurement of semiconductor laser chirp using effect of propagation in dispersive fiber and application to simulation of transmission through fiber gratings," *J. Lightwave Technol.*, vol. 16, 10, pp. 1874-1880, Oct., 1998. Presented at ECOC'98 (Madrid, Spain).
- [6] E. Peral, A. Yariv, "Measurement and characterization of laser chirp of multiquantum-well distributed-feedback lasers," *IEEE Photon. Tech. Lett.*, 11: (3) pp. 307-309, Mar., 1999.
- [7] E. Peral, W. K. Marshall, D. Provenzano, A. Yariv, "Effect of many weak side modes on relative intensity noise of distributed feedback semiconductor lasers," *Appl. Phys. Lett.*, vol. 72, 8, pp. 888-890, Feb., 1998. Presented at CLEO'98 (San Francisco, California).
- [8] M. McAdams, E. Peral, D. Provenzano, W. K. Marshall, A. Yariv, "Improved laser modulation response by frequency modulation to amplitude modulation conversion in transmission through a fiber grating," *Appl. Phys. Lett.*, vol. 71, 7, pp. 879-881, Aug., 1997.
- [9] M. McAdams, D. Provenzano, E. Peral, W. K. Marshall, A. Yariv, "Effect of transmission through fiber gratings on semiconductor laser intensity noise," *Appl. Phys. Lett.*, vol. 23, 8, pp. 3341-3343, Dec., 1997.
- [10] E. Peral, A. Yariv, P. Y. Fonjallaz, "Major reduction of laser RIN and flattening of modulation response using a fiber grating designed by use of the iterative

Gel'fand-Levitan-Marchenko method," BGPP'99 (Indian Plantation Marriott Resort, Florida).

- [11] E. Peral, A. Yariv, "Degradation of modulation and noise characteristics of semiconductor lasers after propagation in optical fiber due to a phase shift induced by stimulated Brillouin scattering," *IEEE. J. Quantum. Electron.*, 35, 8, pp. 1185-1195, Aug. 1999.
- [12] E. Peral, A. Yariv, "Supermodes of grating-coupled multimode waveguides and application to mode conversion between co-propagating modes mediated by backward Bragg scattering," *J. Lightwave Technol.*, 17, 5, pp. 942-947, May 1999.
- [13] E. Peral, A. Yariv, "Optical devices based on energy transfer between different modes in optical waveguides," *Patent pending*, 1999.

## Chapter II.

# Dispersive propagation of lightwave signals

The preferred scheme for transmission of signals in lightwave communication systems is based on intensity modulation (IM) of the optical carrier by an electrical signal and direct detection (DD) by a photodiode at the receiver end to convert the optical signal back to the original electrical format. An alternative approach transmits the information in the frequency or the phase of the optical signal and requires the use of homodyne or heterodyne detection techniques. Although this scheme, known as coherent transmission system, offers better theoretical sensitivity, it has been largely superseded by intensity-modulation direct-detection (IM/DD) systems due to their simplicity and better performance.

There are two schemes for intensity modulation of the light produced by a semiconductor laser, which compete in terms of simplicity and performance. High-speed modulation of semiconductor lasers can be achieved by varying the drive current. This modulation scheme, referred to as *direct-modulation* (see Figure 1), has for long been the preferred method due to its simplicity and large bandwidth. However, variations in the drive current not only modulate the light intensity, but also the optical frequency. As will be explained below, this frequency modulation, also known as laser “chirp,” can cause severe degradation of the transmitted signal when the optical channel is dispersive. *External-modulation* of the laser light (see Figure 2) using chirp-free external

modulators such as electrooptic Mach-Zehnder modulators has been proposed as a solution to this problem. However, the external modulator introduces not only a large optical loss due to coupling to the modulator and waveguide losses but also an additional cost to the system.

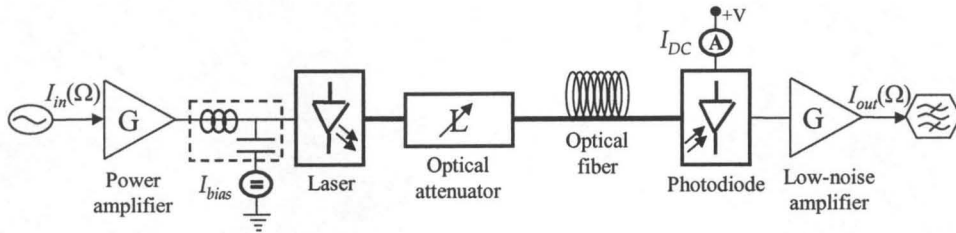


Figure 1: IM/DD system with *direct-modulation* of the semiconductor laser light.

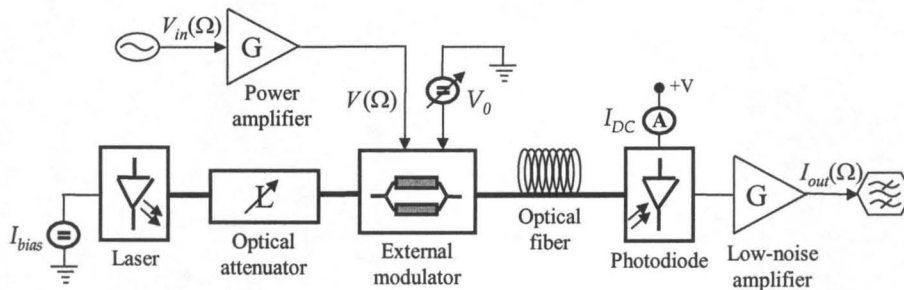


Figure 2: IM/DD system with *external-modulation* of the semiconductor laser light.

The transmission of signals in IM/DD systems is strongly affected by the dispersion of the optical channel. There are two types of dispersion, *group-velocity dispersion*, i.e., different frequency components travel at different group velocities, and *gain dispersion*, i.e., different frequency components experience different gain or loss. The effect of dispersion on lightwave signals is magnified when not only the intensity but also the frequency of the optical signal is modulated, as is usually the case for light

produced by direct modulation of semiconductor lasers. As a consequence of dispersion, part of the frequency modulation (FM) is converted into intensity modulation (IM), which is detected at the receiver end. This FM-to-IM conversion can result in signal distortion, which is manifested as, for example, pulse broadening for digital signals [1]-[2], intermodulation distortion for analog CATV signals [3]-[4], or noise enhancement for modulation driven by noise processes in the laser [5]-[6]. However, FM-to-IM conversion can also be used to advantage to improve the laser modulation response and/or reduce the laser intensity noise, and is the basis of a new transmission system known as dispersion supported transmission (DST) [7], which has been recently receiving increased attention.

Section II.1 presents the small-signal theory of propagation of optical signals in optical channels exhibiting both gain and group-velocity dispersion. It is shown how the small-signal approximation leads to a simple description of optical communication systems in terms of cascaded transfer functions, similar to the ones widely used in linear system theory.

The small-signal approximation provides some insight to the characteristics of the optical transmission. However, it can fail to describe large-signal propagation, which more closely approximates the conditions in practical IM/DD systems. In section II.2, the large-signal theory of propagation of light produced by direct modulation of semiconductor lasers in optical fiber with first order group-velocity dispersion is derived. It will be shown that some of the conclusions extracted from the small-signal theory are not valid in the large-signal regime. Section II.3 extends the previous large-signal analysis to the case of IM/DD systems using external modulation of the laser light. Even though, ideally, external intensity modulators do not induce frequency modulation, the modulator nonlinearity results in enhanced distortion after propagation in fiber.

## II.1 SMALL-SIGNAL THEORY OF DISPERSIVE PROPAGATION OF OPTICAL SIGNALS

### II.1.1 Small-signal propagation in a linear optical channel.

In this section, small-signal modulation of the optical carrier by a sinusoidal tone at a frequency  $\Omega/(2\pi)$  is considered. In general, both intensity and frequency modulation can be present, and the complex electric field amplitude,  $\tilde{E}$ , can be expressed in the form:

$$\tilde{E}(t, z = 0) = P_0^{1/2} (1 + m_{IM} \cos(\Omega t + \varphi_{IM}))^{1/2} e^{im_{FM} \sin(\Omega t + \varphi_{FM})} \quad (1)$$

where  $P_0$  is the average output power,  $m_{IM}$  and  $m_{FM}$  are the intensity modulation (IM) and frequency modulation (FM) indices, respectively, and  $\varphi_{IM}$  and  $\varphi_{FM}$  are the corresponding phases.

In the small-signal regime, i.e., when the modulation indices  $m_{IM}$  and  $m_{FM}$  are much less than unity, equation (1) can be linearized as follows:

$$\tilde{E}(t, z) \cong P_0^{1/2} \left( c_0 + c_{+1} e^{i(\Omega t + \varphi_{IM})} + c_{-1} e^{-i(\Omega t + \varphi_{IM})} \right) \quad (2)$$

where

$$c_0(z = 0) = 1 \quad (3)$$

$$c_{\pm 1}(z = 0) = \frac{m_{IM}}{4} \pm \frac{m_{FM}}{2} e^{\pm i \Delta \varphi} \quad (4)$$

where  $\Delta \varphi = \varphi_{FM} - \varphi_{IM}$  is the dephasing angle between FM and IM.

Thus, in the small-signal approximation, the optical field consists of a main peak corresponding to the optical carrier centered at the laser optical frequency,  $\omega_0$ , accompanied by two modulation sidebands separated from the carrier by  $\pm\Omega$  and with amplitude  $c_{\pm 1} e^{\pm i \varphi_{IM}}$  relative to the amplitude of the carrier.

The signal propagation from the transmitter at  $z = 0$  to the receiver end at  $z$  can be equivalently described as transmission through an optical filter with transmission coefficient  $t(\omega)$ , where  $\omega$  is the optical frequency. The amplitude of the modulation sidebands,  $c_{\pm n}$ , at optical frequency  $\omega_0 \pm n\Omega$  after transmission through  $t(\omega)$  is given by:

$$c_{\pm n}(z) = c_{\pm n}(z = 0)t(\omega_0 \pm n\Omega) \quad (5)$$

At the photodiode, the incoming photons are absorbed and generate electron-hole pairs. This is a square-law detection process. Only the light intensity is detected and the information possibly contained in the phase of the optical signal is lost. Mathematically, the detected photocurrent is proportional to the magnitude squared of the complex electric field amplitude. The proportionality function is called responsivity,  $R$ , and is directly proportional to the absorption quantum efficiency of the electrons in the photodiode. In addition, the response time of the photodiode is limited by the transit time for the photogenerated electrons and holes to reach the electrodes and contribute to the current flow. As a consequence, the responsivity is a function of the modulation frequency, typically introducing a low-pass filtering.

The detected photocurrent,  $\tilde{I}(t, z)$ , is obtained by squaring the electric field magnitude. By keeping only the linear terms in the modulation frequency,  $\Omega$ ,

$$\tilde{I}(t, z) = \left| \tilde{E}(t, z) \right|^2 \cong I(0, z) + I(\Omega, z)e^{i(\Omega t + \varphi_{IM})} + I(-\Omega, z)e^{-i(\Omega t + \varphi_{IM})} \quad (6)$$

By using (1) and keeping only the linear terms in the modulation frequency,  $\Omega$ , we obtain that the photocurrent at  $\Omega$  is given by:

$$I(\Omega, z) \cong R(\Omega)P_0 \left( c_0^* c_{+1} + c_0 c_{-1}^* \right) \quad (7)$$

The DC photocurrent,  $I_{DC}(z) = I(\Omega = 0, z)$ , is given by:

$$I_{DC}(z) \cong R(0)P_0 |c_0|^2 \quad (8)$$

If the photodetector is placed at the transmitter output, then the detected photocurrent is:



$$I(\Omega, z = 0) \cong R(\Omega)P_0 \frac{m_{IM}}{2} \quad (9)$$

After propagation through an optical filter with an optical transfer function  $t(\omega)$ , the detected photocurrent is:

$$I(\Omega, z) \cong I(\Omega, z = 0)H(\Omega, z) \quad (10)$$

where  $H(\Omega, z)$  is the equivalent baseband transfer function that models transmission through the optical channel, and is given by:

$$H(\Omega, z) = H_e(\Omega, z) + 2i H_o(\Omega, z) PIR(\Omega) \quad (11)$$

The functions  $H_e(\Omega, z)$  and  $H_o(\Omega, z)$  are the conjugate-symmetric and conjugate-antisymmetric parts of  $t(\omega)t^*(\omega_0)$  around  $\omega_0$ , that is,

$$H_e(\Omega, z) = \frac{1}{2} [t(\omega_0 + \Omega)t^*(\omega_0) + t^*(\omega_0 - \Omega)t(\omega_0)] \quad (12)$$

$$H_o(\Omega, z) = \frac{1}{2} [t(\omega_0 + \Omega)t^*(\omega_0) - t^*(\omega_0 - \Omega)t(\omega_0)] \quad (13)$$

The  $PIR$  is phase-to-intensity (modulation index) ratio and is given by:

$$PIR = \frac{m_{FM}}{im_{IM}} e^{i\Delta\phi} \quad (14)$$

For light produced by a semiconductor laser, the  $PIR$  is a function of the modulation frequency and is determined by several laser intrinsic parameters.

Equations (11)-(13) indicate that the amount of FM-to-IM conversion is determined by the function  $H_o(\Omega, z)$ , which in turn depends on the amount of gain and group velocity dispersion.

## II.1.2 Small-signal systems description of an optical communications link.

The small-signal approximation allows a simple description of the optical communication system in terms of transfer functions. Each component in the system can be replaced by a "black-box" (see Figure 3) with a particular transfer function and the



total system response is obtained by cascading the different “black-boxes,” i.e., multiplying the corresponding transfer functions. This representation is valid to study both the modulation response when the light is driven by information signals and the noise performance for random noise signals.

The transmitter response in the absence of a dispersive channel is characterized by its intensity modulation (IM) response function,  $H_{IM}(\Omega)$ . This transfer function relates the change in optical power to the small-signal change in the driving source. The driving source can be an injection of electrons from a current generator, the electric field induced by a voltage generator in an electrooptic material, a flux of optically injected photons, or random generation of electrons or photons due to a Langevin noise source. The frequency dependence of  $H_{IM}(\Omega)$  depends on the type of transmitter and driving source.

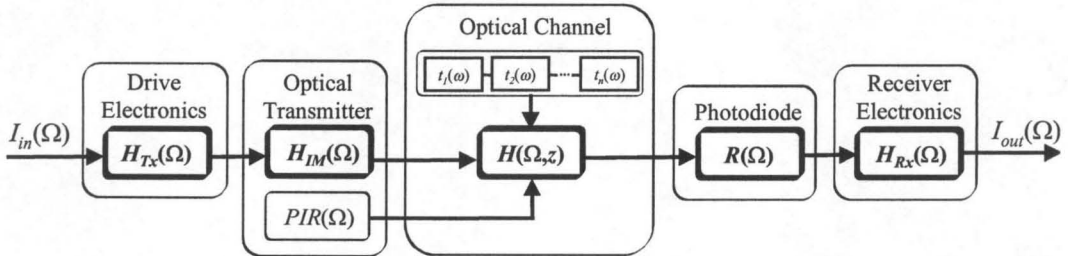


**Figure 3: Transfer function description of an optical communications system.**

The baseband transfer function for the optical channel is given by (11). It is worth noting that this response function does not only depend on the transmission coefficient of the channel but also on the  $PIR$  of the transmitter. In addition, when several optical components are cascaded, the baseband transfer function is not the multiplication of all the corresponding baseband transfer functions. Instead, it is the total transmission coefficient that can be found by cascading the different components, and the resulting transfer function is calculated from (11).

Finally, the photodiode responsivity function,  $R(\Omega)$ , relates the photocurrent and the optical power incident in the photodetector. In addition, the driving and receiving electronics might affect the total system response with transfer functions  $H_{Tx}(\Omega)$  and  $H_{Rx}(\Omega)$ , respectively.

The total baseband transfer function is given by:

$$H_T(\Omega, z) = H_{Rx}(\Omega)R(\Omega)H(\Omega, z)H_{IM}(\Omega)H_{Tx}(\Omega) \quad (15)$$

If the transmitter is modulated with a small-signal current,  $I_{in}(\Omega)$ , then the received current  $I_{out}(\Omega, z)$  is given by:

$$I_{out}(\Omega, z) = H_T(\Omega, z)I_{in}(\Omega) \quad (16)$$

### II.1.3 Small-signal propagation in optical fiber.

A case of special interest is propagation in optical fiber. Due to the large bandwidth of the optical fiber at the wavelengths of interest, the fiber gain dispersion can be neglected for the modulation speeds that can be achieved by state-of-the-art transmitters. On the contrary, the group velocity dispersion of the fiber can be quite large. The fiber dispersion is due to the intrinsic material dispersion of the silica and to the waveguide dispersion of the fiber. At wavelengths near  $1.3\mu\text{m}$ , the so-called second transmission window, both forms of dispersion have the same magnitude but opposite sign, and the total group velocity dispersion is close to zero. Despite this advantage, communication systems are migrating to the third communications window at wavelengths near  $1.55\mu\text{m}$  due to the global minimum in the fiber attenuation at this wavelength, and to the development of the erbium-doped fiber amplifier (EDFA), for which there is no ready equivalent at  $1.3\mu\text{m}$ . However, at  $1.55\mu\text{m}$ , standard optical fiber exhibits large dispersion and its effect needs to be taken into account.

Thus, the transmission coefficient of the optical fiber is well described by a phase filter and a wavelength independent attenuation as follows:

$$t_{fib}(\omega) = e^{-\frac{\alpha_f}{2}z - i\beta(\omega)z} \quad (17)$$

where  $\alpha_f$  is the fiber power attenuation coefficient,  $\beta(\omega)$  is the propagation constant, and  $z$  is the fiber length. Near the laser optical frequency  $\omega_0$ ,  $\beta(\omega)$  can be Taylor series expanded as:

$$\beta(\omega) = \beta(\omega_0) + \beta'(\omega_0)(\omega - \omega_0) + \frac{1}{2}\beta''(\omega_0)(\omega - \omega_0)^2 + \frac{1}{6}\beta'''(\omega_0)(\omega - \omega_0)^3 + \dots \quad (18)$$

For most cases of interest, this series can be truncated after three terms. The three coefficients,  $\beta(\omega_0)$ ,  $\beta_1 \equiv \beta'(\omega_0)$  and  $\beta_2 \equiv \beta''(\omega_0)$  will determine the phase velocity, the group velocity and the first order group velocity dispersion, respectively. When  $\beta_2$  is close to zero, the next term,  $\beta_3 \equiv \beta'''(\omega_0)$ , corresponding to second order group velocity dispersion, can become important.

Due to group velocity dispersion, linear propagation in a dispersive optical fiber produces a phase change of the sidebands relative to the optical carrier, which results in partial conversion of FM into IM, which is then photodetected at the fiber output. Substitution of (17)-(18) into (11)-(13) yields the fiber baseband transfer function:

$$H(\Omega, z) \cong [\cos\theta - 2\sin\theta PIR(\Omega)]e^{-\alpha_f z + i\varphi} \quad (19)$$

If only first-order group velocity dispersion is included, then

$$\theta(\Omega, z) = -\frac{1}{2}\beta_2\Omega^2 z \quad (20)$$

$$\varphi(\Omega, z) = -\beta_1\Omega z \quad (21)$$

When higher-order group velocity dispersion cannot be neglected,

$$\theta(\Omega, z) = -\frac{1}{2}\beta_2\Omega^2 z - \frac{1}{24}\beta_4\Omega^4 z - \dots \quad (22)$$

$$\varphi(\Omega, z) = -\beta_1\Omega z - \frac{1}{6}\beta_3\Omega^3 z - \dots \quad (23)$$

## II.1.4 Measurement of the baseband transfer function of an optical channel.

### II.1.4.A Using a network analyzer.

A network analyzer (NA) allows easy determination of the phase and magnitude of the system response to a deterministic sinusoidal tone. The experimental set-up is shown in Figure 4. The laser light is directly or externally modulated and coupled to the optical channel. The received signal is detected with a PIN photodetector. Measurements of the  $S_{21}$  parameter at the laser output and after propagation in the channel yield  $H_T(\Omega, z = 0)$  and  $H_T(\Omega, z)$ , respectively. From (15),  $H(\Omega, z)$  is obtained as:

$$H(\Omega, z) = \frac{H_T(\Omega, z)}{H_T(\Omega, z = 0)} \quad (24)$$

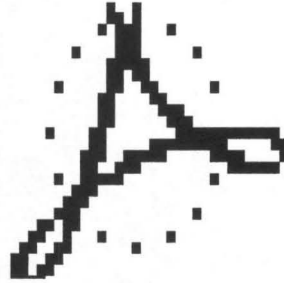


Figure 4: Experimental setup for measuring the system response with a network analyzer.

The value of the DC photocurrent,  $I_{DC}(z) = I(\Omega = 0, z)$ , can also be measured with a current meter, and the system DC attenuation,  $L_{DC}$ , can be determined as:

$$L_{DC}(z) = \frac{I_{DC}(z = 0)}{I_{DC}(z)} \quad (25)$$

### II.1.4.B Using an electrical spectrum analyzer.

For noise signals, or when additional spectral information, such as harmonic distortion, is needed, an electrical spectrum analyzer (ESA) can be used. In this case, however, the phase information is lost. The experimental set-up is shown in Figure 5.

In some cases, it is necessary to determine the spectrum of the receiver power without the effect of photodiode responsivity and receiver electronics. In the following, a method is presented that allows determination of the combined effect of the photodiode responsivity and receiver electronics on the received power spectrum, which can then be subtracted to obtain an accurate spectral response of the optical system.

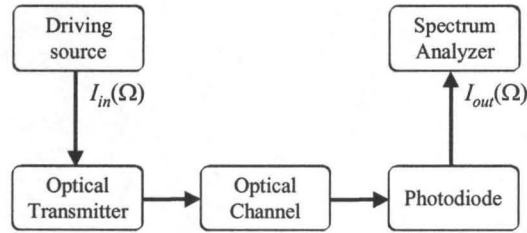


**Figure 5: Experimental setup for measuring the system response with an electric spectrum analyzer.**

The light produced by an unmodulated semiconductor laser is photodetected and the noise spectrum,  $P_N(\Omega)$ , is measured.  $P_N(\Omega)$  can be expressed as a quadratic function of the DC photocurrent,  $I_{DC}$ , as follows:

$$P_N(\Omega) = a(\Omega) + b(\Omega)I_{DC} + c(\Omega)I_{DC}^2 \quad (26)$$

The term independent of the DC photocurrent is mainly due to thermal noise from the amplifier and is given by:

$$a(\Omega) = |H_{Rx}(\Omega)|^2 F_N(\Omega) N_{th} \quad (27)$$

where  $N_{th}$  is the input thermal noise power,  $F_N$  is the amplifier noise figure and  $H_{Rx}(\Omega)$  is the transfer function of the receiver electronics.

The shot noise power, which originates from the random creation of electrons in the photodiode, varies linearly with the DC photocurrent. The coefficient  $b(\Omega)$ , for single-sided noise power computation, is given by:

$$b(\Omega) = |H_{Rx}(\Omega)|^2 \left| \frac{R(\Omega)}{R(0)} \right|^2 2e\Delta f \quad (28)$$

where  $\Delta f$  is the electrical bandwidth.

The last term is the excess intensity noise, which comes from fluctuations in the received optical power,  $\Delta P$ , and is given by:

$$c(\Omega) = |H_{Rx}(\Omega)|^2 \left| \frac{R(\Omega)}{R(0)} \right|^2 \frac{\langle |\Delta P|^2 \rangle}{P_0^2} \Delta f \quad (29)$$

where  $P_0$  is the average received optical power.

The relative weight of the different noise contributions can be controlled by adjusting the received optical power, that is  $I_{DC}$ , with an optical attenuator. Thus, the thermal noise contribution,  $a(\Omega)$ , can be measured by blocking the light, i.e.,  $a(\Omega) = P_N(\Omega)|_{I_{DC}=0}$ . The coefficients  $b(\Omega)$  and  $c(\Omega)$  are functions of frequency and can be found at each frequency  $\Omega$  by measuring  $P_N(\Omega)$  for several values of  $I_{DC}$  and fitting it to a parabola as in (26).

The relative excess intensity noise ( $RIN$ ) is defined as the spectral density of the excess noise power divided by the average received power. Once  $a(\Omega)$  and  $b(\Omega)$  are known at each frequency for a particular combination of photodiode and receiver, the  $RIN$  for any noise power measurement,  $P_N$ , is computed as:

$$RIN(\Omega) \equiv \frac{\langle |\Delta P|^2 \rangle}{P_0^2} = 2e \frac{P_N(\Omega) - a(\Omega) - b(\Omega)I_{DC}}{b(\Omega)I_{DC}^2} \quad (30)$$

The small-signal  $RIN$  after propagation through an optical channel with baseband transfer function  $H(\Omega, z)$  and DC attenuation  $L_{DC}(z)$  is given by:

$$RIN(\Omega, z) = L_{DC}^2(z) |H(\Omega, z)|^2 RIN(\Omega, z = 0) \quad (31)$$

## II.2 LARGE-SIGNAL THEORY OF PROPAGATION OF DIRECTLY-MODULATED LIGHT IN DISPERSIVE FIBER

Semiconductor lasers have the very useful property that they can be modulated at high speed by varying the drive current. Changes in the number of injected electrons are followed by changes in the gain, and thus in the number of photons that are being generated. In addition, there is a fundamental relationship between the gain and the refractive index of a semiconductor medium. As a consequence, variations in the drive current not only modulate the light intensity, but also the optical path length and thus the optical frequency. This frequency modulation that always accompanies the intensity modulation is referred to as laser chirp, and has major consequences in the laser intensity modulation response after propagation in dispersive fiber.

The technologically important problem of the effect of dispersive fiber propagation on the intensity modulation response of semiconductor lasers was treated in the past by assuming either small-signal modulation [7]-[8], in a similar way to the description presented in section II.1.3, or low dispersion [9]. The small-signal theory is a reasonable approximation for transmitters with no chirp, but it can fail to describe semiconductor laser light, which usually exhibits large frequency modulation even for relatively small intensity modulation. In this section, the analysis in section II.1.3 is extended to include large-signal and arbitrary dispersion, which more closely approximates conditions in IM/DD systems, for the case of direct-modulation of the laser light.

For certain values of the laser chirp and the fiber length, the small-signal theory developed in the previous section predicts an enhancement of the laser intensity



modulation response up to a cut-off frequency [7] due to conversion of part of the FM into IM. This high-pass characteristic is the basis of operation for a new type of transmission system known as dispersion supported transmission (DST) [7]. In this section, it is shown that the highpass behavior of the fiber transfer function that is predicted by the small-signal theory is degraded as the amplitude of the modulation signal is increased, which could affect the performance of DST systems.

## II.2.1 Theory

### II.2.1.A 1-tone large-signal direct modulation.

First, direct modulation of the laser by a single sinusoidal tone at a frequency  $\Omega/(2\pi)$  is considered. Semiconductor lasers are nonlinear devices, and the intensity modulation and frequency modulation responses contain harmonics of the modulation frequency. However, to a first approximation it can be assumed that the intensity and frequency of the light vary linearly with modulation (the general case is considered below). The complex electric field amplitude,  $\tilde{E}$ , at the laser output can be expressed as in (1).

In the analysis presented here it is assumed that the IM can be linearized as in section II.1.3, but the exact form of the FM is maintained. Thus, the IM is approximated by an amplitude modulation (AM) as follows:

$$\left(1 + m_{IM} \cos(\Omega t + \varphi_{IM})\right)^{1/2} \cong m_0 \left(1 + m_{AM} \cos(\Omega t + \varphi_{IM})\right) \quad (32)$$

where, as a first approximation,  $m_0 \cong 1$  and the AM index  $m_{AM} \cong m_{IM}/2$  (see Appendix II.1 for a more accurate expression for  $m_0$  and  $m_{AM}$ ). By using (32) and expanding the FM as a series of Bessel functions [13], the electric field amplitude can be written as:

$$\begin{aligned} \tilde{E}(t, z = 0) &\cong P_0^{1/2} \left(1 + \frac{m_{IM}}{2} \cos(\Omega t + \varphi_{IM})\right) e^{im_{FM} \sin(\Omega t + \varphi_{FM})} \\ &= P_0^{1/2} \sum_{n=-\infty}^{\infty} c_n(z = 0) e^{in(\Omega t + \varphi_{IM})} \end{aligned} \quad (33)$$



$$c_n(z=0) = e^{in\Delta\varphi} \left[ J_n(m_{FM}) + \frac{m_{IM}}{4} \left( J_{n+1}(m_{FM})e^{i\Delta\varphi} + J_{n-1}(m_{FM})e^{-i\Delta\varphi} \right) \right] \quad (34)$$

where  $\Delta\varphi = \varphi_{FM} - \varphi_{IM}$ .

In propagation through the fiber the different harmonics acquire different phase changes due to dispersion according to (17). In order to simplify notation, the effect of the fiber attenuation,  $\alpha_f$ , and the group delay,  $\tau_g = \beta_1 z$ , will be omitted in the following derivation. They contribute to a frequency-independent power loss and a linear phase delay, respectively. Thus, the amplitude of the  $n^{\text{th}}$  harmonic at  $z$  can be expressed as:

$$c_n(z) = e^{in^2\theta(z)} c_n(0) \quad (35)$$

where  $\theta(z)$  is given in (20).

The detected photocurrent,  $\tilde{I}(t, z)$ , is obtained by squaring the electric field magnitude,

$$\tilde{I}(t, z) = \left| \tilde{E}(t, z) \right|^2 = \sum_{n=-\infty}^{\infty} I(n\Omega, z) e^{in(\Omega t + \varphi_{IM})}, \quad (36)$$

and the photocurrent at the  $n^{\text{th}}$  harmonic  $I(n\Omega, z)$ , is given by

$$I(n\Omega, z) = R(n\Omega) P_0 \sum_k c_{n+k}(z) c_k^*(z) \quad (37)$$

where  $R(n\Omega)$  is the photodiode responsivity at frequency  $n\Omega$ .

In previous analyses,  $I(n\Omega, z)$  was calculated either numerically [14] or by using the small-signal approximation. Here, we have applied a summation theorem of the Bessel functions [13] to derive the *exact*  $I(n\Omega, z)$  for an electric field with AM and FM as in equation (33), and is given by:

$$I(n\Omega, z) = R(n\Omega) P_0 i^n e^{in\Delta\varphi} \left[ J_n(u) - i \frac{m_{IM}}{2} \cos n\theta \left( J_{n-1}(u) e^{-i\Delta\varphi} - J_{n+1}(u) e^{i\Delta\varphi} \right) \right] \quad (38)$$

where  $u = 2m_{FM} \sin n\theta$ .

The fiber modulation transfer function relates the photodetected current at the modulation frequency after and before propagation in dispersive fiber. From (38), we obtain:

$$H(\Omega, z) = \cos\theta \left( J_0(u) - J_2(u)e^{i2\Delta\varphi} \right) - 2 \frac{e^{i\Delta\varphi}}{im_{IM}} J_1(u) \quad (39)$$

where  $u = 2m_{FM} \sin\theta$ , which simplifies in the small-signal limit to (19).

Equation (19) indicates that the small-signal fiber transfer function only depends on known fiber properties, namely  $\beta_2$  and fiber length, and the laser *PIR*, which is a laser intrinsic property. In the next chapter, it will be shown how the *PIR* can be determined by measuring the small-signal fiber transfer function for several lengths of fiber [11]. In addition, from equations (38) (or (56) in Appendix II.1) and (39) we observe that the large-signal response of the laser after propagation in fiber is also fully characterized by the laser *PIR* and the laser intensity modulation index,  $m_{IM}$ .

### II.2.1.B *N*-tone large-signal direct modulation.

The analysis presented in the previous section can be extended to the case of an input signal consisting of an arbitrary number  $N$  of tones at angular frequencies  $\Omega_k$  (which is also the case when the laser nonlinear dynamics cannot be neglected and harmonics of the laser IM and FM response need to be included). The complex electric field envelope can be expressed as:

$$\tilde{E}(t, z = 0) \cong P_0^{1/2} \left( 1 + \sum_{k=1}^N \frac{m_{IM_k}}{2} \cos(\Omega_k t + \varphi_{IM_k}) \right) e^{i \sum_{k=1}^N m_{FM_k} \sin(\Omega_k t + \varphi_{FM_k})} \quad (40)$$

By using the same type of analysis as above, we obtain that the detected signal after propagation in dispersive fiber is given by:

$$\tilde{I}(t, z) = \sum_{n_1, n_2, \dots, n_N = -\infty}^{\infty} I\left(\sum_{k=1}^N n_k \Omega_k, z\right) e^{i \sum_{k=1}^N n_k (\Omega_k t + \varphi_{IM_k})} \quad (41)$$

The photodetected intensity for the intermodulation product (IMP)  $\Omega_{IMP} \equiv \sum_{k=1}^N n_k \Omega_k$  is given by:

$$I(\Omega_{IMP}, z) = R(\Omega_{IMP}) P_0 i^{\sum_{k=1}^N n_k} e^{i \sum_{k=1}^N n_k \Delta \varphi_k} \prod_{k=1}^N (J_{n_k}(u_k)) \left[ 1 - \sum_{k=1}^N i \frac{m_{IMk}}{2} \cos \theta_k \left( J_{n_k-1}(u_k) e^{-i \Delta \varphi_k} - J_{n_k+1}(u_k) e^{i \Delta \varphi_k} \right) / J_{n_k}(u_k) \right] \quad (42)$$

where

$$u_k = 2m_{FMk} \sin \theta_k \quad (43)$$

$$\theta_k(\Omega_{IMP}, z) = -1/2 \beta_2 \Omega_k \Omega_{IMP} z \quad (44)$$

The total intermodulation distortion at a particular frequency is equal to the sum of all the IMP's in (41) that fall onto that frequency.

In Appendix II.2 the theory here developed is applied to the case of a typical CATV transmission system.

## II.2.2 Simulation

In this section the validity of the approximation in (32), i.e., linearization of the laser IM, is verified by comparison with the exact analysis. The laser *PIR* is assumed to be that of the MQW-DFB laser tested below ( $\alpha \cong -4$ ). Figure 6 shows the modulation transfer function after 85 km of standard fiber for several intensity modulation indices. It is observed that the large-signal fiber transfer function deviates significantly from the small-signal model for intensity modulation indices greater than 0.2. On the contrary, equation (56) remains accurate even for intensity modulation indices close to unity. The major discrepancy occurs at the dips of the transfer function, where the received intensity is very small and the effect of the small IM harmonics becomes more important.

Comparison of (39) and (19) (as can also be observed in Figure 6) indicates that the maximum of the fiber transfer function for any given laser parameters occurs at the

*smallest* intensity modulation. Thus, the enhancement of modulation response due to propagation that is attained in the small-signal regime is suppressed as  $m_{IM}$  is increased. This could pose severe limitations to systems such as dispersion supported transmission [7] that rely on the improvement in the modulation response to combat dispersion.

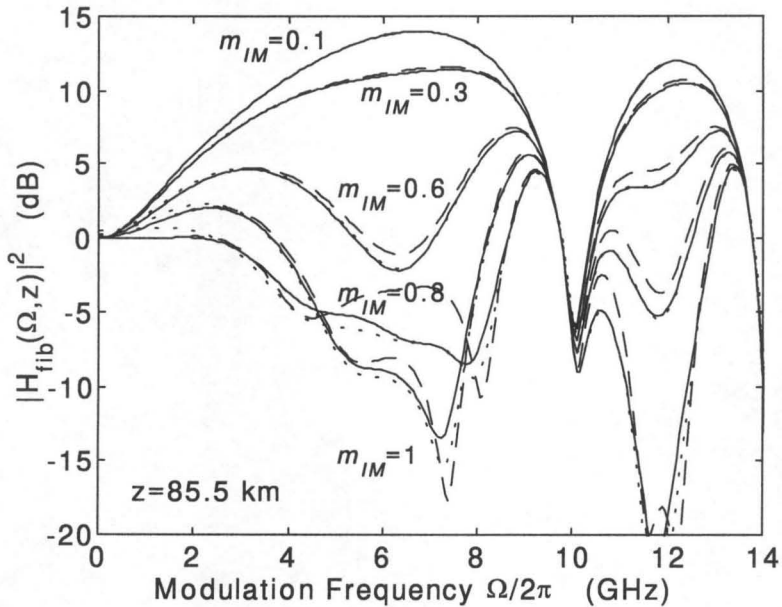


Figure 6: Numerical simulations of fiber modulation transfer function after propagation in 85 km of fiber for different modulation indices. Dashed from Eq. (39), dotted from Eq. (56) and solid is exact. Curve for  $m_{IM} = 0.1$  nearly coincides with small-signal approximation Eq. (19).

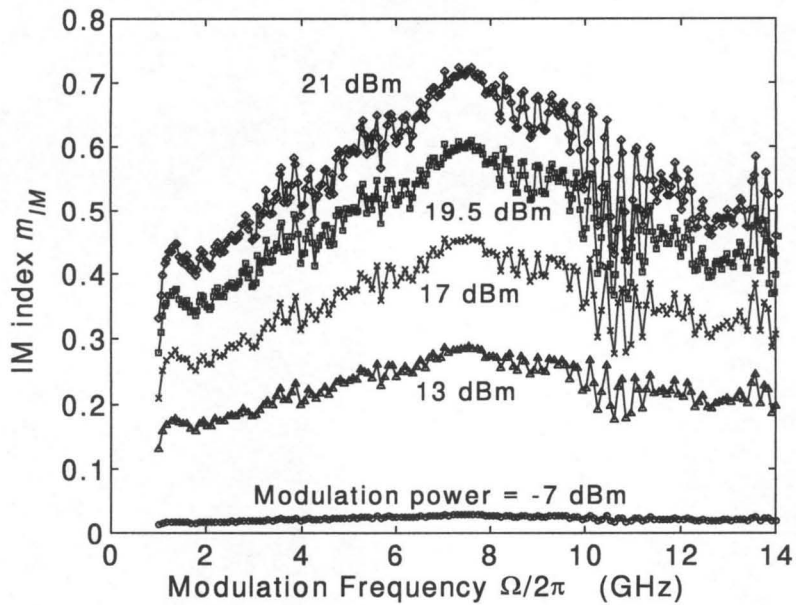
### II.2.3 Experiment

The predictions of this large-signal theory have been compared to the measured photocurrent of light from a directly-modulated MQW-DFB laser at  $1.55\mu\text{m}$  after propagation in several lengths of standard fiber. The experimental set-up is shown in Figure 1. Measurements were performed for single-tone modulation using a network

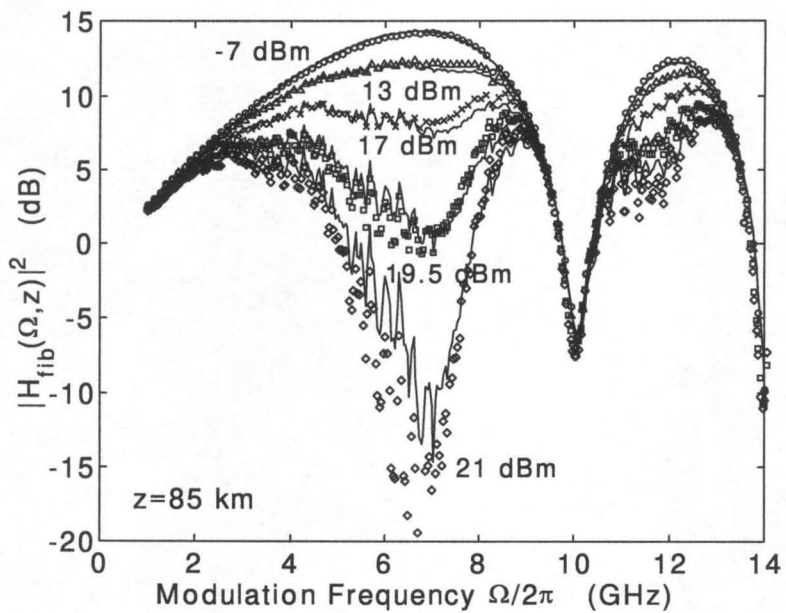
analyzer (NA) as signal generator, and for two-tone modulation using the combined signal from the NA and a signal generator (SG). The modulation response was measured with the NA and the intermodulation distortion with the electric spectrum analyzer (ESA). The electrical signal,  $I_{in}(\Omega)$ , was amplified and combined with the laser bias current,  $I_{bias}$ , to directly modulate the laser. The laser light was coupled to an optical fiber, attenuated to avoid the effect of fiber nonlinearities (see Chapter IV), and propagated through fiber. The detected photocurrent was amplified and measured with the NA or ESA.

The *PIR* was determined using a measurement based on small-signal fiber propagation and equation (19), that will be fully described in the next chapter. The intensity modulation index,  $m_{IM}$ , was determined by measuring the modulation response before propagation in fiber and subtracting the receiver (photodiode + amplifier + network analyzer) response.

Figure 7a shows the measured intensity modulation index,  $m_{IM}$ , as a function of modulation frequency at the laser output for several modulation powers. The frequency dependence of  $m_{IM}$  is due to the combined effect of the driving electronics,  $H_{Tx}(\Omega)$ , and the laser dynamics,  $H_{IM}(\Omega)$ . This  $m_{IM}$  together with the *PIR* were used to predict the large-signal fiber transfer function,  $H(\Omega, z)$ , for 85km of fiber. This is plotted in Figure 7b (solid) together with the experimental data points. As  $m_{IM}$  increases, the highpass behavior that is attained with small-signal modulation (circles) is degraded. At very large  $m_{IM}$ , equation (39) does not perfectly agree with the experiment due to the presence of IM harmonics (and consequently FM harmonics) at the laser output that were neglected in (39), and not to the approximation in (32). This was verified by estimating the effect of these higher order terms in the modulation response (a complete determination of the modulation response including these terms was not possible because the relative phase between the IM harmonics was not known).

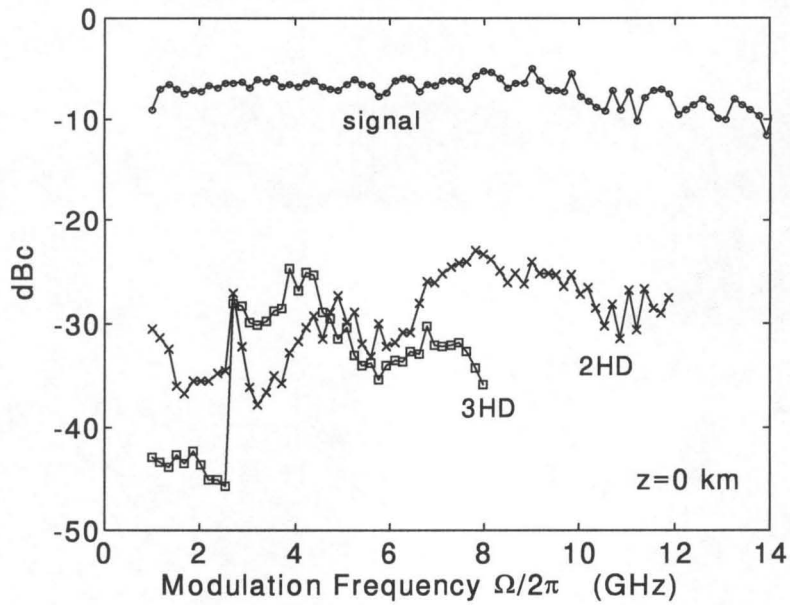


(a)

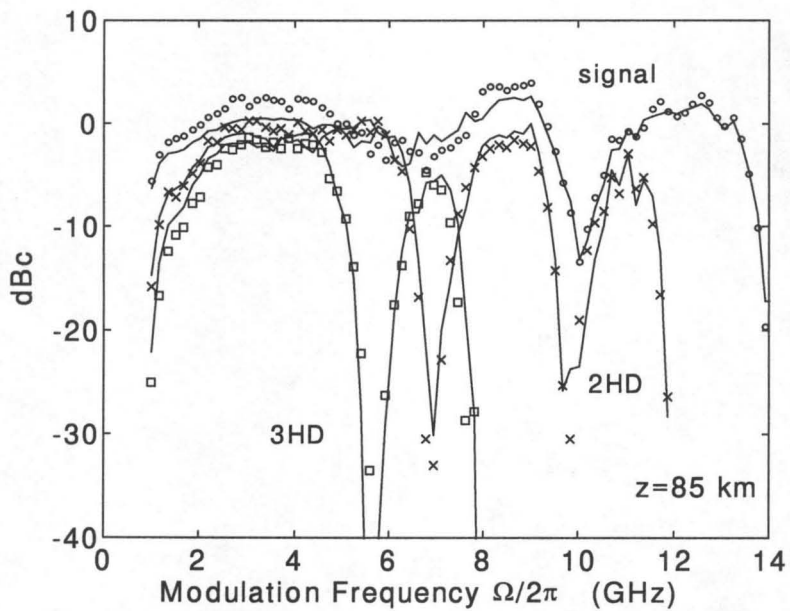


(b)

Figure 7: (a) Intensity modulation index measured at the laser output for several modulation powers. (b) Fiber modulation transfer function after propagation in 85 km of fiber for the same modulation powers as in Figure 7a. Solid curve is theory.



(a)



(b)

Figure 8: Experimentally detected power in signal (circles), second harmonic (crosses) and third harmonic (squares) normalized by the power in the optical carrier, (a) at the laser output, (b) after propagation in 85 km of fiber. Solid curve is theory.



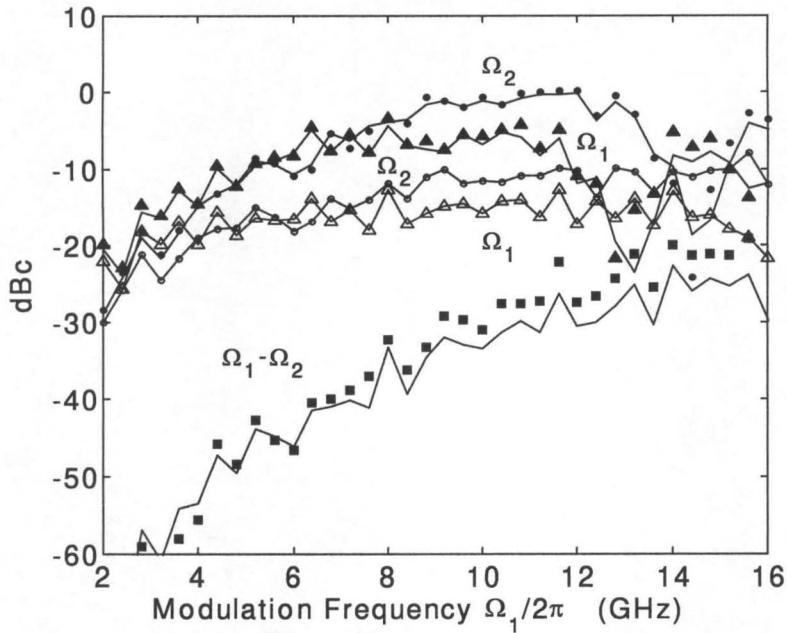


Figure 9: Experimentally detected normalized power in dBc for 2-tone modulation at the laser output at  $\Omega_1$  (open triangles) and  $\Omega_2=0.9\Omega_1$  (open circles) and after propagation in 50km of fiber at  $\Omega_1$  (solid triangles),  $\Omega_2$  (solid triangles) and  $\Omega_1-\Omega_2$  (solid squares). Solid curve is theory.

The harmonic distortion was also measured after propagation in fiber. Figure 8a shows the power in the modulation frequency,  $\Omega$ , and in higher-order harmonics of  $\Omega$  normalized by the power in the optical carrier (denoted in log scale by dBc) at the laser output ( $z = 0$ ). The harmonic distortion at the laser output comes from the poor spectral purity of the signal generator, and also to a smaller degree from the nonlinearity of the laser dynamics. The measured power in the modulation tone at  $\Omega$  (higher order IM harmonics were not included in the analysis) together with the *PIR* were used to predict harmonic distortion after propagation in 85km of fiber. This theory is shown in Figure 8b (solid curve), and agrees well with the experiment. Thus, it can be concluded that in this case the main source of harmonic distortion after propagation comes from beating of the FM sidebands and is well described by (56). It is also observed in Figure 8b that the



power in the harmonics exhibits the same characteristics as that in the modulation tone, namely peaks and dips that repeat more rapidly as  $\Omega$  increases and as the order of the harmonic increases.

The intermodulation distortion was measured by modulating the laser with two tones at angular frequencies  $\Omega_1$  and  $\Omega_2=0.9\Omega_1$ . Figure 9 shows the detected signal before and after propagation in fiber (in dBc) at the modulation tone frequencies and in the IMP  $\Omega_2-\Omega_1$ , which agrees with the theoretical prediction (solid curve).

### II.3 LARGE-SIGNAL THEORY OF PROPAGATION OF EXTERNALLY-MODULATED LIGHT IN DISPERSIVE FIBER

Chirp-free external modulators have been proposed as a solution to the problem of signal distortion that arises from chirped signals propagating in dispersive fiber, such as the light produced by a directly-modulated laser. Among the different types of external modulators, electrooptic Mach-Zehnder modulators (EO-MZM) show particularly good performance. However, the modulation response of an ideal EO-MZM (even with no chirp) is highly nonlinear, and will exhibit large harmonic distortion, in fact larger than that that would be obtained with a directly-modulated laser with no chirp. In linear propagation through the fiber the different harmonics acquire different phase changes due to group velocity dispersion, and severe signal distortion can occur.

In this section, the large-signal theory of propagation of externally-modulated light in dispersive fiber is derived. The intensity modulation response after fiber propagation is shown to be similar to that of a directly-modulated laser, with dips that repeat more frequently as  $\Omega$  increases. However, since the modulator is chirp-free, there is never an enhancement of the modulation response, as opposed to the case of a directly modulated semiconductor laser.

## II.3.1 Theory

### II.3.1.A 1-tone large-signal external modulation.

The complex electric field amplitude,  $\tilde{E}$ , at the output of EO-MZM can be expressed in the form:

$$\tilde{E}(t, z = 0) = P_0^{1/2} \cos\left(\frac{\pi}{2} \frac{V(t)}{V_\pi}\right) \quad (45)$$

where  $P_0$  is the input optical power,  $V(t)$  is the voltage applied to the modulator, and  $V_\pi$  is the half-wave voltage of the EO-MZM.

If a sinusoidal tone is applied to the modulator such as

$$\frac{V(t)}{V_\pi} = v_0 + v \sin(\Omega t + \varphi) \quad (46)$$

where  $v_0$  is the normalized DC bias,  $v_0 = V_0/V_\pi$ , and  $v$  is the normalized amplitude of the modulation tone, then the electric field spectrum will consist of sidebands at harmonics of the modulation frequency centered around the laser optical frequency as follows:

$$\tilde{E}(t, z = 0) = P_0^{1/2} \sum_{n=-\infty}^{\infty} c_n(z = 0) e^{in(\Omega t + \varphi)} \quad (47)$$

where

$$c_n(z = 0) = \frac{1}{2} J_n\left(\frac{\pi}{2} v\right) \left[ e^{i\frac{\pi}{2} v_0} + (-1)^n e^{-i\frac{\pi}{2} v_0} \right] \quad (48)$$

In linear propagation through the fiber, the different harmonics acquire different phase changes according to (35).

The detected photocurrent,  $\tilde{I}(t, z)$ , is given by:

$$\tilde{I}(t, z) = |\tilde{E}(t, z)|^2 = \sum_{n=-\infty}^{\infty} I(n\Omega, z) e^{in(\Omega t + \varphi)} \quad (49)$$

From (36)-(37) and using the summation theorem of the Bessel functions [13],  $I(n\Omega, z)$  can be found as

$$I(n\Omega, z) = \frac{1}{2} R(n\Omega) P_0 \left[ \left\{ \begin{array}{c} 0 \\ (-1)^{n/2} \end{array} \right\} J_n(\pi v \sin n\theta) + \right. \\ \left. + \left\{ \begin{array}{c} i \sin(\pi v_0) \\ \cos(\pi v_0) \end{array} \right\} J_n(\pi v \cos n\theta) \right], \quad \text{for } \begin{cases} n \text{ odd} \\ n \text{ even} \end{cases} \quad (50)$$

If the EO-MZM is biased at quadrature, i.e.,  $v_0 = \pm 1/2$ , there is no even harmonic distortion at the output of the modulator. However, propagation in fiber produces a phase change of the sidebands relative to the optical carrier, which results in significant second harmonic distortion when the sidebands beat upon photodetection. Equation (50) indicates that for any  $v$  the maximum second harmonic distortion in a frequency range such that  $\theta \geq \pi/4$  is larger than the maximum third harmonic distortion.

### II.3.1.B $N$ -tone large-signal external modulation.

A similar analysis can be used for input signals consisting of an arbitrary number  $N$  of tones,

$$\frac{V(t)}{V_\pi} = v_0 + \sum_{k=1}^N v_k \sin(\Omega_k t + \varphi_k) \quad (51)$$

Following a similar derivation to that in the previous sections, it is found that the photodetected intensity for the intermodulation product (IMP)  $\Omega_{IMP} \equiv \sum_{k=1}^N n_k \Omega_k$  is given by:

$$I(\Omega_{IMD}, z) = \frac{1}{2} R(\Omega_{IMD}) P_0 \left[ \left\{ \begin{array}{c} 0 \\ (-1)^{\sum_{k=1}^N n_k / 2} \end{array} \right\} \prod_{k=1}^N J_k(\pi v_k \sin \theta_k) + \right. \\ \left. + \left\{ \begin{array}{c} i \sin(\pi v_0) \\ \cos(\pi v_0) \end{array} \right\} \prod_{k=1}^N J_k(\pi v_k \cos \theta_k) \right], \quad \text{for } \sum_{k=1}^N n_k \begin{cases} \text{odd} \\ \text{even} \end{cases} \quad (52)$$

where  $\theta_k$  is given in (44).

### II.3.2 Experiment

The general scheme for external modulation is shown in Figure 2. The DC bias,  $V_0$ , is controlled by using a programmable voltage source.

In the expression for the transfer function of an EO-MZM in (45), it was assumed that the modulator has infinite bandwidth, i.e., its response does not depend on the frequency of the input signal. In practice, the bandwidth of an EO-MZM is limited mainly by the group-velocity mismatch between electrical and optical signals. It can be shown that the frequency response of the modulator can be included in the analysis by letting the half-wave voltage be a function of the modulation frequency,  $V_\pi = V_\pi(\Omega)$ . In the next subsection a method is presented to determine the normalized amplitude of the modulation tone including the effect of the frequency dependence of  $V_\pi$ ,  $v = \frac{V(\Omega)}{V_\pi(\Omega)}$ . This is then used to compare the large-signal theory introduced in section II.2.1 with experimental measurements of modulation response and intermodulation distortion.

#### II.3.2.A Determination of the frequency dependence of the half-wave voltage.

From equation (50) it can be deduced that when the DC voltage is set such that  $v_0 = \pm 1$  or  $v_0 = 0$ , the detected signal at the modulation frequency vanishes. In addition, in the absence of fiber, the DC photocurrent reaches minimum and maximum values, respectively. These are given by:

$$\text{For } \begin{cases} v_0 = \pm 1, & I_{DCmin} = \frac{1}{2} R(0) P_0 (1 - J_0(\pi v)) \\ v_0 = 0, & I_{DCmax} = \frac{1}{2} R(0) P_0 (1 + J_0(\pi v)) \end{cases} \quad (53)$$

The ratio  $I_{DCmin}/I_{DCmax}$  only depends on the normalized amplitude of the modulation tone,  $v = \frac{V(\Omega)}{V_{\pi}(\Omega)}$ . From the value of this ratio for several values of  $V(\Omega)$ , i.e., of the modulation power, the value of  $V_{\pi}(\Omega)$  at a particular modulation frequency  $\Omega/2\pi$  can be fitted.

In practice, it is the RF power that is measured. Then, the half-wave power,  $P_{\pi}(\Omega)$ , is the RF power necessary to obtain a voltage equal to  $V_{\pi}(\Omega)$ . The experimental set-up used for determination of  $P_{\pi}(\Omega)$  is shown in Figure 10. A sinusoidal voltage from a signal generator (SG) and a DC voltage from a programmable voltage source were applied to the EO-MZM. The detected DC photocurrent and signal at the modulation frequency were measured. The instruments were controlled by means of a PC. At each modulation frequency, the value of the DC photocurrent was measured for applied DC voltages such that  $v_0 = 1$  and  $v_0 = 0$ . The DC voltage was precisely adjusted by suppressing the signal at the modulation frequency.

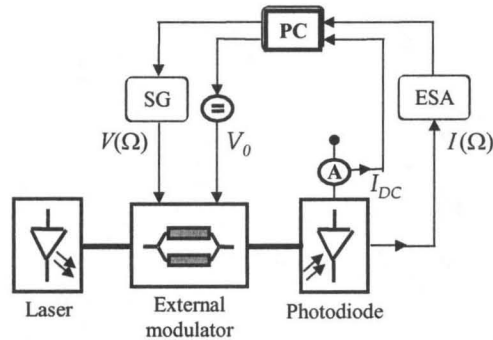


**Figure 10: Experimental set-up for measuring the frequency dependence of the half-wave voltage for an EO-MZM. SG=signal generator, ESA=electrical spectrum analyzer, A=ammeter, PC=personal computer.**

Figure 11 shows the measured  $P_\pi(\Omega)$  as a function of the modulation frequency.  $P_\pi(\Omega)$  increases as the modulation frequency increases, which indicates the typical low-pass filter behavior of EO-MZM's.

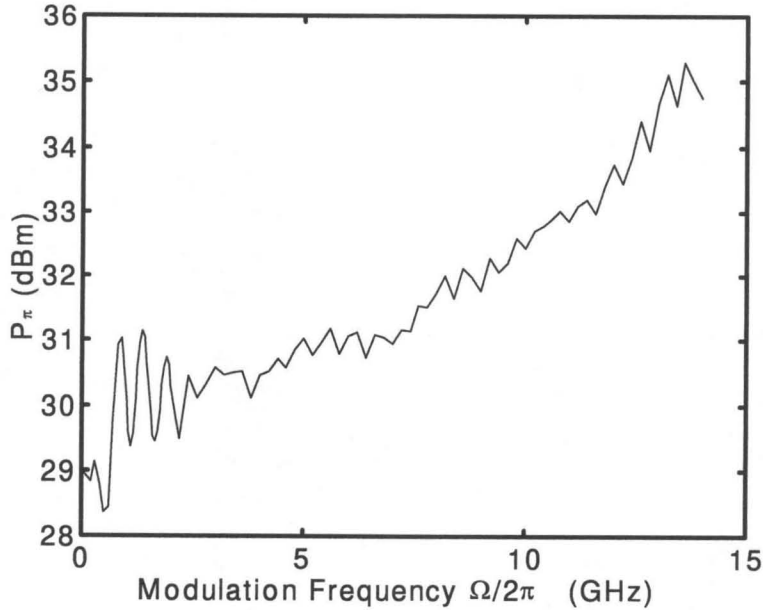
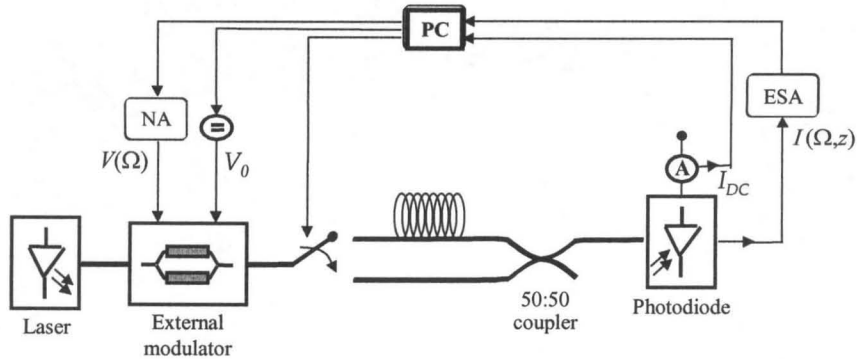


Figure 11: Measured half-wave power of EO-MZM as a function of the modulation frequency.

### II.3.2.B Measurement of the modulation response and harmonic distortion.

The modulation response and harmonic distortion was measured for single-tone external modulation of the light produced by an MQW-DFB semiconductor laser at 1.55  $\mu\text{m}$  after propagation in dispersive fiber. In practice, the DC voltage of an EO-MZM exhibits a drift, and as a consequence, has to be adjusted constantly by means of a control loop. The experimental set-up is shown in Figure 12. The DC operating point was adjusted at quadrature for each modulation frequency by suppressing the second harmonic distortion at the modulator output. Then, an electrically controlled optical

switch was activated to measure the received power in the signal and harmonics after propagation in fiber.



**Figure 12: Experimental set-up for measuring the modulation response and harmonic distortion for externally-modulated light after propagation in fiber.**

Figure 13 shows the received power at the modulation frequency normalized by the power in the optical carrier (in dBc) at the modulator output (empty circles) and after propagation in 105km of standard fiber (solid circles), the normalized power in the second harmonic after fiber (solid triangles) and the normalized power in the third harmonic at the modulator output (empty squares). The intensity modulation response after fiber propagation shows dips and peaks that repeat more frequently as  $\Omega$  increases. However, since the modulator is chirp-free, the modulation response is never greater than that at the modulator output. It is also observed that even though the even harmonic distortion vanishes at the modulator output, it can reach significant magnitude after propagation in dispersive fiber. This is due to the fact that the modulation sidebands of the electrical field out of an EO-MZM are very large, also for even harmonics. At the modulator output those contributing to even harmonic distortion add out of phase and cancel. However, in linear propagation through the fiber the different modulation sidebands acquire different phase changes due to group velocity dispersion. For sufficiently high modulation frequency or long distance, the

sidebands contributing to even harmonic distortion can add in phase giving rise to large harmonic distortion.

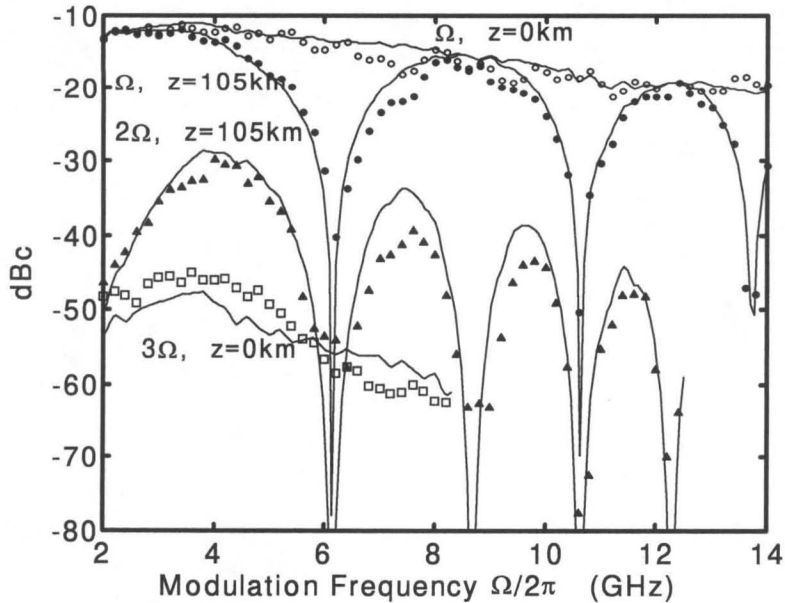


Figure 13: Experimentally detected power normalized by the power in the optical carrier at the modulator output in signal (empty circles) and third harmonic (empty squares), and after propagation in 105 km of fiber at signal (solid circles) and second harmonic (solid triangles). Solid curve is theory.



## Appendix II.1 A MORE ACCURATE AND AN EXACT LARGE-SIGNAL THEORY FOR DIRECT LASER MODULATION

In (33) the AM index was approximated by  $m_{IM}/2$ . We can instead expand the IM, i.e., the left-hand side of (32), as a Fourier series,

$$(1 + m_{IM} \cos(\Omega t + \varphi_{IM}))^{1/2} \cong \sum_l m_l e^{il(\Omega t + \varphi_{IM})} \quad (54)$$

where the Fourier coefficients,  $m_l$ , are given by [13],

$$m_l = (-1)^{l+1} \sum_{n=0}^{\infty} \frac{(4n+2l-3)!!}{(4n+2l)!!} \binom{2n+l}{n} \left( \frac{m_{IM}}{2} \right)^{2n+l} \quad (55)$$

By keeping only the AM sideband at the modulation frequency, i.e., by using the approximation (32) with  $m_{AM} = 2m_1$ , the detected photocurrent at frequency  $n\Omega$  is given by:

$$I(n\Omega, z) = R(n\Omega)P_0 i^n e^{in\Delta\varphi} \left[ m_0^2 J_n(u) + 2im_0 m_1 \cos n\theta (J_{n+1}(u)e^{i\Delta\varphi} - J_{n-1}(u)e^{-i\Delta\varphi}) + 4m_1^2 (2J_n(u) \cos 2n\theta - J_{n-2}(u)e^{-i2\Delta\varphi} - J_{n+2}(u)e^{i2\Delta\varphi}) \right], \quad n \geq 1 \quad (56)$$

In section II.2.2 it is shown that the above expression is very accurate even for intensity modulation indices close to unity.

If all the harmonic sidebands of the IM in (54) are taken into account, then:

$$I(n\Omega, z) = R(n\Omega)P_0 \sum_{l,l'=-\infty}^{\infty} i^{n+l-l'} m_l m_{l'} e^{i(n+l-l')\Delta\varphi} e^{in\theta(l+l')} J_{n+l-l'}(u) \quad (57)$$

Equation (57) is *exact* for an electric field with IM and FM. The double infinite sum in (57) converges fast and only a few terms are needed. This is simpler than previous formulations [14] that involved four infinite sums.

## Appendix II.2 INTERMODULATION DISTORTION IN CATV SYSTEMS WITH DIRECT LASER MODULATION

As an example of the theory developed in section II.2, transmission of  $N$  NTSC channels of CATV is considered. At the typical CATV frequencies, the laser chirp is mostly adiabatic, and can be approximated by:

$$PIR \cong -\frac{\alpha \kappa_0}{2 i\Omega} \quad (58)$$

For moderate propagation distances,

$$u_k \cong 2m_{FM_k} \theta_k \cong \frac{1}{2} m_{IM_k} \alpha \kappa_0 \beta_2 z \Omega_{IMP} = u_k(\Omega_{IMP}, z) \quad (59)$$

Thus, the value of the IMP's depends only on the frequency of the intermodulation product,  $\Omega_{IMP}$ , but not on the frequency of the beating tones.

In CATV systems, small intensity modulation indices are usually employed in order to avoid clipping of the signal. By substituting (59) into (42), and using a power series expansion of the Bessel functions, we obtain:

$$I(\Omega_{IMP}, z) \cong R(\Omega_{IMP}) P_0 e^{-\alpha z + i\varphi(\Omega_{IMP}, z)} \prod_{k=1}^N \left( \frac{m_{IM_k}^{|n_k|}}{|n_k|!} \right) (i\Omega_{IMP} \xi)^n \left( 1 + \frac{n}{2i\Omega_{IMP} \xi} \right) \quad (60)$$

where  $\xi = \frac{1}{4} \alpha \kappa_0 \beta_2 z$  and  $n = \sum_{k=1}^N |n_k|$  is the order of the IMP.

Assuming that all channels have the same intensity modulation index,  $m_{IM_k} = m_{IM}$ , the  $n^{\text{th}}$ -order intermodulation distortion ( $IMD_n$ ) normalized by the power in the RF carrier is approximately given by:

$$IMD_n(\Omega, z) \approx \frac{A_n(\Omega)}{(n-1)!} (m_{IM} i\Omega \xi)^{n-1} \quad (61)$$

where

$$A_n(\Omega) = \sum_{\substack{i_1, \dots, i_n=1 \\ \Omega = \pm\Omega_{i_1} \pm \dots \pm \Omega_{i_n}}}^N e^{i(\pm\varphi_{IM_{i_1}} \pm \dots \pm \varphi_{IM_{i_n}})} \quad (62)$$

From (62) it becomes evident that by proper management of the carrier phases it should be possible to affect the intermodulation distortion spectrum.

For uncorrelated carriers the total intermodulation distortion *IMD* is:

$$IMD(\Omega, z) \approx \sum_n N_n(\Omega) \left| \frac{(m_{IM} \Omega \xi)^{n-1}}{(n-1)!} \right|^2 \quad (63)$$

where  $N_n(\Omega) = \langle |A_n|^2 \rangle$  is the number of beats for that order.

## REFERENCES

- [1] D. Marcuse, "Pulse distortion in single-mode fibers," *Appl. Opt.*, vol. 19, 10, pp. 1653-1660, May, 1980.
- [2] D. Marcuse, "Pulse distortion in single-mode fibers. 3: Chirped pulses," *Appl. Opt.*, vol. 20, 20, pp. 3573-3579, Oct., 1981.
- [3] T. E. Darcie, G. E. Bodeep, "Lightwave subcarrier CATV transmission systems," *IEEE Trans. Microw. Theory & Tech.*, vol. 38, 5, pp. 524-533, May, 1990.
- [4] H. A. Blauvelt, N. S. Kwong, P. C. Chen, I. Ury, "Optimum range for DFB laser chirp for fiber-optic AM video transmission," *J. Lightwave Technol.*, vol. 11, 1, pp. 55-59, Jan., 1993.
- [5] K. Petermann, "FM-AM noise conversion in dispersive single mode fiber transmission lines," *Electron. Lett.*, vol. 26, 25, pp. 2097-2098, Dec., 1990.
- [6] W. K. Marshall, J. Paslaski, A. Yariv, "Reduction of relative intensity noise of the output field of semiconductor lasers due to propagation in dispersive optical fiber," *Appl. Phys. Lett.*, vol. 68, 18, pp. 2496-2498, Apr., 1996.
- [7] B. Wedding, "Analysis of fiber transfer function and determination of receiver frequency response for dispersion supported transmission," *Electron. Lett.*, vol. 30, 1, pp. 58-59, Jan., 1994.
- [8] A. R. Chraplyvy, R. W. Tkach, L. L. Buhl, R. C. Alferness, "Phase modulation to amplitude modulation conversion of cw laser light in optical fibers," *Electron. Lett.*, vol. 22, 8, pp. 409-411, Apr., 1986.
- [9] K. Petermann, J. Wang, "Large signal analysis of FM-AM conversion in dispersive optical fibers and its application to PCM systems," *Electron. Lett.*, vol. 27, 25, pp. 2347-2348, Dec., 1991.
- [10] M. McAdams, E. Peral, D. Provenzano, W. K. Marshall, A. Yariv, "Improved laser modulation response by frequency modulation to amplitude modulation

conversion in transmission through a fiber grating," *Appl. Phys. Lett.*, vol. 71, 7, pp. 879-881, Aug., 1997.

- [11] E. Peral, W. K. Marshall, A. Yariv, "Precise measurement of semiconductor laser chirp using effect of propagation in dispersive fiber and application to simulation of transmission through fiber gratings," *J. Lightwave Technol.*, Oct. 1998.
- [12] E. Peral, A. Yariv, "Measurement and characterization of laser chirp of multiquantum-well distributed-feedback lasers," *IEEE Photon. Tech. Lett.*, 11: (3) pp. 307-309, Mar., 1999
- [13] M. Abramowitz, I. Stegun, *Handbook of mathematical functions: with formulas, graphs, and mathematical tables*, Dover, New York, 1976.
- [14] G. J. Meslener, "Chromatic dispersion induced distortion of modulated monochromatic light employing direct detection," *IEEE Quantum Electron.*, vol. QE-20, 10, pp. 1208-1216, Oct., 1984.



## Chapter III.

# Dynamics of semiconductor lasers and effect of dispersive propagation

**A** good understanding of the different factors affecting the laser dynamics is critical to the laser design and also to the assessment of its performance in a communications system. In the previous chapter, theoretical models were presented that describe the effect of dispersive propagation on semiconductor laser light. In this chapter, these models are applied to the characterization of the laser dynamics and also to the development of new techniques to improve the laser transmission properties.

First, in section III.1 the concepts that were presented in the previous chapter about small-signal propagation in dispersive fiber are applied to the precise measurement of the laser chirp. Using this method, the laser chirp of several distributed-feedback multi-quantum-well (DFB-MQW) lasers is measured and it is found that the simple rate equations model that is commonly employed fails to accurately describe the measured laser chirp.

A number of possible mechanisms have been proposed to explain the damping that limits the modulation bandwidth of DFB-MQW lasers. These include spectral hole burning, carrier heating, quantum capture, carrier diffusion and spatial hole burning. In

section III.2, the effect of these different damping mechanisms on the laser chirp is evaluated. It is shown that the measured laser chirp can be well described by a simple model that includes the effect of carrier transport and quantum carrier capture into the quantum wells (QW's).

The performance of a lightwave communication system is often affected by the laser noise, which can be a critical factor in determining the system signal-to-noise ratio. When the link includes propagation in dispersive optical fiber, it is important to determine the laser intensity noise at the fiber output, which can be different from the intensity noise at the laser output due to frequency modulation to intensity modulation conversion. A single-mode theory of noise after propagation in dispersive fiber had been previously derived. However, in section III.3 it is shown that this theory might not accurately predict the detected noise, and that is necessary to include the existence of the many weak side modes that always accompany the main mode of nearly-single-mode DFB lasers.

The effect that dispersion has on the laser intensity modulation response and intensity noise can be used to improve the laser transmission characteristics. In section III.4 it is shown that a properly designed fiber grating can produce major reduction of the laser intensity noise and at the same time shape the modulation response in an almost arbitrary way.



### **III.1    PRECISE MEASUREMENT OF SEMICONDUCTOR LASER CHIRP USING THE EFFECT OF PROPAGATION IN DISPERSIVE FIBER**

#### **III.1.1    Introduction**

The performance of high-speed lightwave systems using 1.55  $\mu\text{m}$  semiconductor lasers with direct modulation is significantly affected by the laser chirp. Semiconductor laser chirp is commonly characterized by two parameters, the linewidth enhancement factor and the cross-over frequency between the adiabatic and transient regimes of chirp, which follow from a rate equation analysis of the laser. Recently, it has been demonstrated that the frequency modulation to intensity modulation (FM-to-IM) conversion effect due to propagation in dispersive optical fiber can be used conveniently to measure the linewidth enhancement factor and cross-over frequency of the laser [1]-[5]. In careful examination of data obtained with this technique, however, it is found that although a good fit to theory may be obtained when fitting results for a single length of fiber, for some lasers a large variation of the parameters occurs for results obtained with different lengths of fiber. This variation for different fibers is attributed to the more detailed dependence of laser chirp on modulation frequency.

In this section a new measurement technique is demonstrated that conveniently determines the precise characteristics of the laser chirp using the effect of propagation in optical fiber. Implications for simulation of high-speed lightwave systems are also considered.

#### **III.1.2    Theory**

A direct method for determining the laser chirp is to observe the sidebands of the optical field spectrum using an interferometer (see Appendix III.1). A more convenient

method, however, is to introduce some optical filtering to convert part of the frequency modulation (FM) to intensity modulation (IM) so that it can be photodetected. Propagation through dispersive optical fiber can be used to produce this filtering [1]-[5].

In the previous chapter, the fiber small-signal baseband transfer function was derived. In order to simplify the notation, the fiber attenuation can be omitted. Then, the small-signal baseband transfer function after propagation in standard fiber can be expressed as:

$$H(\Omega, z) \cong (\cos\theta - 2\sin\theta \text{ PIR}(\Omega))e^{i\varphi} \quad (1)$$

where the dispersion angle is given by:

$$\theta(\Omega, z) = -\frac{1}{2}\beta_2\Omega^2 z \quad (2)$$

and the propagation delay angle is:

$$\varphi(\Omega, z) = -\beta_1\Omega z \quad (3)$$

$H(\Omega, z)$  in equation (1) depends only on known or measurable fiber parameters, namely the inverse of the group velocity,  $\beta_1$ , the dispersion parameter,  $\beta_2$ , and the fiber length,  $z$ , and on the laser  $\text{PIR}$ . Therefore, measurements of  $H(\Omega, z)$  with a network analyzer as described in Chapter II can be used to determine the  $\text{PIR}$ .

### III.1.3 Description of methods

#### III.1.3.A Previous method for measuring the laser chirp [1]-[5].

The first reports of using propagation in dispersive fiber to determine the laser  $\text{PIR}$  [4], [5] start from the assumption that the  $\text{PIR}$  in the small-signal regime takes the form [6]:

$$\text{PIR} = -\frac{\alpha}{2} \left( 1 + \frac{\kappa}{i\Omega} \right) \quad (4)$$

This expression can be derived from the simple rate equation model of semiconductor lasers. Here,  $\alpha$  is the linewidth enhancement factor and  $\kappa$  is the cross-over frequency

between adiabatic and transient chirp regimes.  $\kappa$  is related to the gain compression parameter,  $\varepsilon$ , the photon lifetime,  $\tau_{ph}$ , and the optical power  $P_0$  through the expression  $\kappa = \varepsilon P_0 / \tau_{ph}$ .

In [1]-[5] the *PIR* is extracted from measurements of  $|H(\Omega, z)|^2$  as a function of frequency for a certain length of fiber,  $z$ . Using (1)-(4), the parameters  $\alpha$  and  $\kappa$ , together with  $\beta_2$  if it is unknown, are found by least squares fitting  $|H(\Omega, z)|^2$ . However, it will be shown in section III.1.4 that this procedure can yield very different values for  $\kappa$  and also to a lesser extent for  $\alpha$  for different lengths of fiber, which indicates that the model is not entirely correct.

### III.1.3.B Precise method for measuring the laser chirp [7]

In the method described above, a specific expression for the *PIR* was used to fit for the unknowns. However, for a more detailed laser model [8]-[11] equation (4) is only approximately correct. In this section a different approach will be used that consists of letting the unknowns be the real and imaginary part of the *PIR* at each modulation frequency, and then use equation (1) to derive the precise frequency dependence of the laser *PIR* from measurements of  $H(\Omega, z)$ .

If the value of the dispersion product  $\beta_2 z$  is known, measurements of  $|H(\Omega, z)|^2$  for two different lengths of fiber,  $z_1$  and  $z_2$ , result in two equations that can be solved for the *PIR*. Using (1), the real and imaginary parts of the *PIR* are given by:

$$\text{Re}\{PIR\} = \frac{|H(\Omega, z_2)|^2 \sin^2 \theta_1 - |H(\Omega, z_1)|^2 \sin^2 \theta_2 + \cos^2 \theta_1 \sin^2 \theta_2 - \cos^2 \theta_2 \sin^2 \theta_1}{4 \sin \theta_1 \sin \theta_2 (\cos \theta_1 \sin \theta_2 - \cos \theta_2 \sin \theta_1)} \quad (5a)$$

$$\text{Im}\{PIR\} = \pm \left[ |H(\Omega, z_1)|^2 - (\cos \theta_1 - 2 \text{Re}\{PIR\} \sin \theta_1)^2 \right]^{1/2} / (2 \sin \theta_1) \quad (5b)$$

where  $\theta_i = \theta(\Omega, z_i)$ . Equation (5b) indicates that the sign of the imaginary part of the *PIR* cannot be resolved by measurements of just the magnitude of  $H(\Omega, z)$ .

The sign of the imaginary part can be obtained by measuring the phase of  $H(\Omega, z)$ . In fact, measurements of phase and magnitude of  $H(\Omega, z)$  and the group delay,  $\beta_1 z$ , after a single length of fiber yield the *PIR* as:

$$\text{Re}\{PIR\} = \frac{\cos\theta - \text{Re}\{H(\Omega, z)e^{-i\varphi}\}}{2\sin\theta} \quad (6a)$$

$$\text{Im}\{PIR\} = -\frac{\text{Im}\{H(\Omega, z)e^{-i\varphi}\}}{2\sin\theta} \quad (6b)$$

However, it is not straightforward to determine the group delay, since it is strongly dependent on the optical frequency, which in turn varies with temperature and bias current.

In practice, the choice of fiber lengths determines at which frequencies a good measurement for the *PIR* is obtained. As an example,  $|H(\Omega, z)|^2$  is most sensitive to changes in the imaginary part of the *PIR* near frequencies such that,

$$\theta(\Omega, z) \approx \arctan(-1/\alpha) + n\pi \quad (7)$$

where  $n$  is an integer. Good accuracy for a wide range of modulation frequencies could be obtained by measuring  $H(\Omega, z)$  after several lengths of fiber. In addition, use of both phase and magnitude of  $H(\Omega, z)$  improves determination of the *PIR* because the phase of  $H(\Omega, z)$  is more sensitive to changes in the *PIR* at frequencies at which the magnitude is not so sensitive.

The procedure proposed here to measure the precise frequency dependence of the *PIR* is as follows. First, the magnitude and phase of  $H(\Omega, z)$  are measured after several lengths of fiber. Then, at each modulation frequency,  $\Omega$ ,  $|H(\Omega, z)|^2$  is fitted as a function of fiber length for a fixed value of  $\beta_2$  to yield real and imaginary parts of the *PIR*( $\Omega$ ). This *PIR* is substituted into (1) to find the theoretical phase of  $H(\Omega, z)$  in the absence of propagation delay. The linear phase term added in propagation can be determined by performing a linear fit to the difference between this phase and the experimental phase in a certain frequency range where there is confidence that the

previously measured  $PIR$  is sufficiently accurate. Once the propagation delay has been found, both magnitude and phase of  $H(\Omega, z)$  can be used to obtain a more precise measurement of the  $PIR$ . The dispersion parameter  $\beta_2$  can be measured independently or can be extracted from the same measurement by selecting the value that minimizes the quadratic error between theory and experiment.

In the following, it will be assumed with no loss of generality that the  $PIR$  can be expressed as in (4) but with  $\kappa$  a complex function of the modulation frequency. The results will display the real and imaginary parts of  $\kappa$  as a function of  $\Omega$  for a certain value of  $\alpha$ , which in principle can be chosen arbitrarily. Here,  $\alpha$  is chosen to be that obtained from measurements of relative intensity noise ( $RIN$ ) after propagation in fiber. In section III.2 it will be shown that this is a convenient description for a more detailed laser chirp analysis. In addition, this model makes it possible to visualize the frequency dependence of the imaginary part of the  $PIR$ , which would otherwise be masked by the strong adiabatic term that varies as  $1/\Omega$ , and also to compare the values for  $\kappa$  thus obtained with those of the simple model.

### III.1.4 Experiment

The fiber baseband transfer function,  $H(\Omega, z)$ , was measured for several lengths of fiber, and the methods presented above were used to determine the laser  $PIR$ . The laser used in the experiment was an MQW-DFB semiconductor laser at  $1.55 \mu\text{m}$ .

Figure 1 shows the phase and magnitude of  $H(\Omega, z)$  after propagation in 2km (circles) and 50km (triangles) of fiber. The method outlined in section III.1.3.A was used to find the parameters  $\alpha$  and  $\kappa$  for different fixed values of  $\beta_2$ . Values of  $\beta_2$  from  $-19$  to  $-21$  ps/km<sup>2</sup> were used and the value of  $\beta_2$  and corresponding  $\alpha$  and  $\kappa$  were selected that yielded the minimum quadratic error. This fitting procedure was not sensitive to the initial guesses for  $\alpha$  and  $\kappa$ . Good fits for each of the experimental curves can be obtained (solid in Figure 1), but each fiber yields very different values for  $\alpha$  and  $\kappa$ . These values, when used to describe propagation in the other fiber length, produce poor agreement

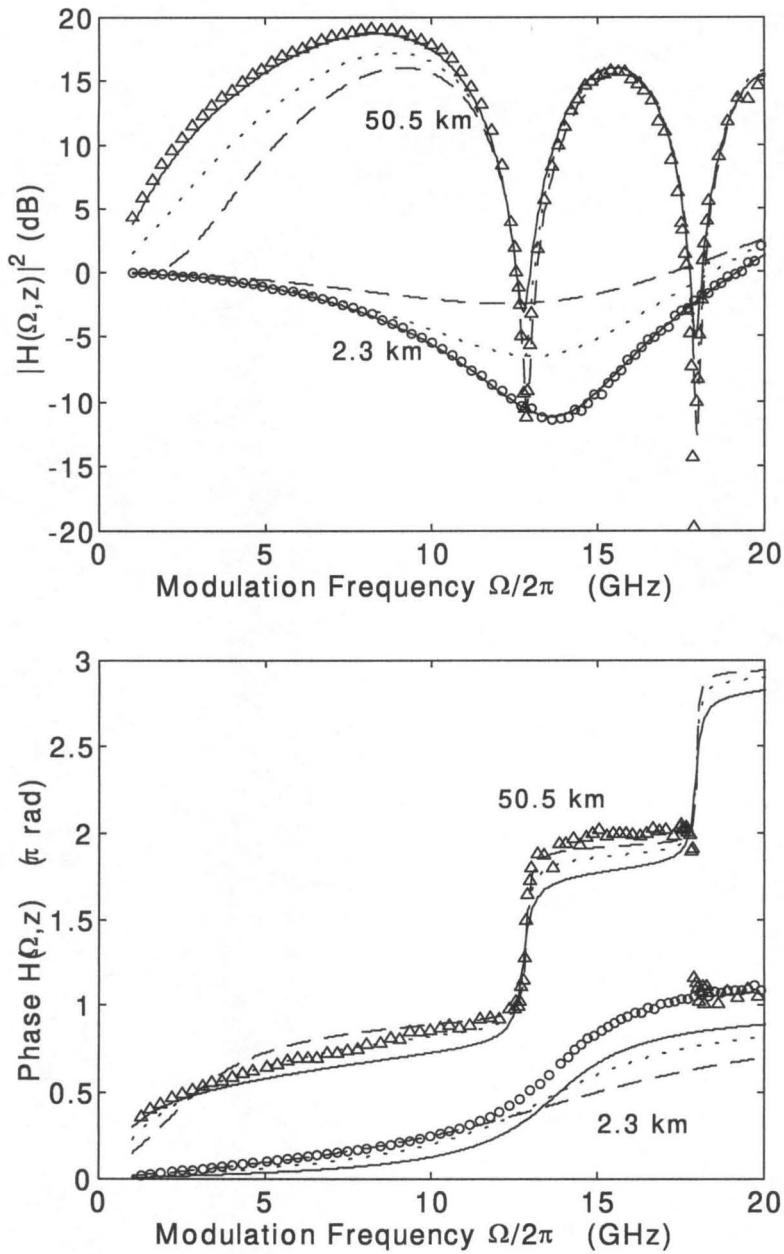


Figure 1: Experimental change in modulation response after 2.3km (circles) and 50.5km (triangles) of fiber. The parameters  $\kappa$  and  $\alpha$  are determined that best fit the change in modulation response after 2.3 km (solid), 50.5 km (dashed) and both lengths of fiber (dotted). Output power at laser facet is 14.3mW.

between theory and experiment (dashed). Values for  $\alpha$  and  $\kappa$  were also found by minimization of the combined error for both fiber lengths, but no good fits were obtained (dotted). In particular, the values found were:

$$\text{Fitting of } |H(\Omega, z)|^2 \text{ for } z=2\text{km} \quad \Rightarrow \quad \alpha=-5.8 \text{ and } \kappa=24.6 \text{ ns}^{-1}$$

$$\text{Fitting of } |H(\Omega, z)|^2 \text{ for } z=50\text{km} \quad \Rightarrow \quad \alpha=-4.9 \text{ and } \kappa=79.3 \text{ ns}^{-1}$$

$$\text{Fitting of } |H(\Omega, z)|^2 \text{ for both } z=2\text{km and } 50\text{km} \quad \Rightarrow \quad \alpha=-5.8 \text{ and } \kappa=42.8 \text{ ns}^{-1}$$

The discrepancy is due to the fact that the simple laser model used to derive (4) does not fully describe the laser FM response. The reason why good fits are obtained for single lengths of fiber is that the value of  $\kappa$  mainly determines the width and depth of the dips in  $|H(\Omega, z)|^2$  that for small  $\kappa$  occur near frequencies such that (7) is satisfied. The fitting procedure tends to adjust the value of  $\kappa$  so as to obtain small error near these dips. Since the position in frequency of these dips depends on the fiber length, and  $\kappa$  can be considered to be a function of the modulation frequency,  $\Omega$ , the fitted value changes for different lengths of fiber. In our experiment,  $\kappa$  was mainly determined by the first dip, because higher order dips are narrower, and therefore contained fewer (evenly spaced) data points. Thus, an estimate for the value of  $\kappa$  at a particular modulation frequency can be obtained by choosing a length of fiber,  $z$ , such that  $|H(\Omega, z)|^2$  has its first dip at the desired frequency.

The previous results will be now compared with the *PIR* obtained by using the method introduced in section III.1.3.B. Several spools of fiber with lengths 2, 4, 8 and 25km were used in the experiment. Figure 2 shows the real (circles) and imaginary (triangles) parts of  $\kappa(\Omega)$  for  $\alpha=-5.5$  obtained from  $|H(\Omega, z)|^2$  for different combinations of fibers. The measurement is compared with the results using both phase and magnitude (solid and dashed, respectively). In Figure 2 (a) and (b),  $\kappa(\Omega)$  was obtained from measurement of two fibers. The sets of fiber were selected to yield good results in the frequency range from 3.5 to 8GHz and 4 to 14GHz, respectively. It is observed that the

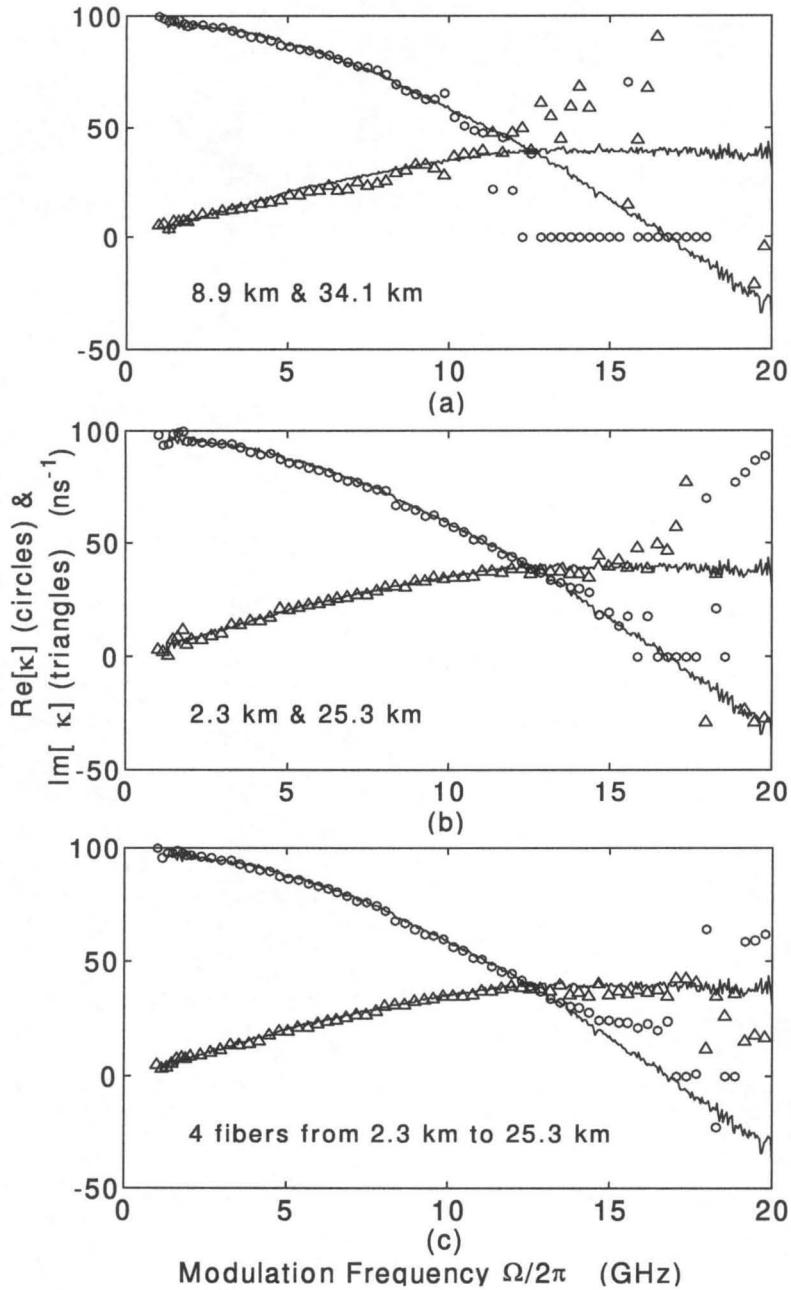


Figure 2: Real (circles) and imaginary (triangles) part of  $\kappa(\Omega)$  with  $\alpha=-4.43$  obtained from  $|H(\Omega, z)|^2$  for different combinations of fiber. Solid and dashed are the result from using magnitude and phase of  $H(\Omega, z)$ . Output power at laser facet is 14.3mW.



measured  $\kappa(\Omega)$  is noisier at low frequencies for the first set, and improves at higher frequencies with respect to the second set. Figure 2c shows the result when four fibers are employed. Above 14GHz the measurement is noisy because that is the limit set by the shortest fiber that was used. Thus, measurement of  $\kappa(\Omega)$  at higher modulation frequencies would require shorter fibers.

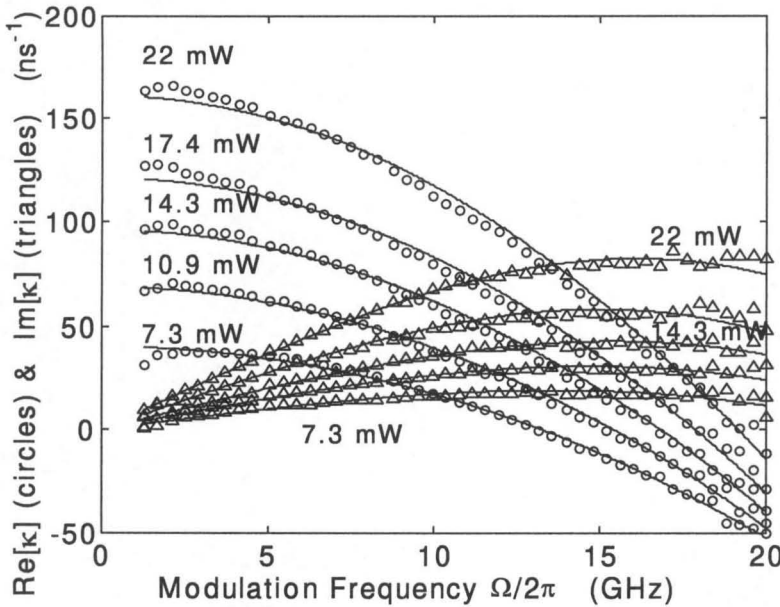


Figure 3: Real (circles) and imaginary (triangles) part of  $\kappa(\Omega)$  at several laser output powers obtained from magnitude and phase of  $H(\Omega, z)$ .  $\alpha$  takes the values  $-4.37, -4.39, -4.43, -4.58, -4.57$  with increasing output power. Solid corresponds to the theory in section III.2.2.

Figure 3 shows the measured  $\kappa(\Omega)$  for several optical powers using both phase and magnitude of  $H(\Omega, z)$ . The value of  $\kappa(\Omega)$  in Figure 2a was used in a frequency range from 1 to 7GHz to determine the propagation delay as described in section III.1.3.B, and then the *PIR* was extracted from magnitude and phase of  $H(\Omega, z)$  after 2km of fiber. The variance of the measured *PIR* for different fibers was very small. At

high frequencies, the real part of  $\kappa(\Omega)$  becomes negative, which cannot be determined from measurements of only  $|H(\Omega, z)|^2$ .

It is worth noting that the simple model predicts that the real part of  $\kappa$  is constant with modulation frequency, and that the imaginary part is zero or at most can vary linearly with  $\Omega$ . Figure 3 clearly indicates that at least for the laser tested, this is not a valid model.

The measured  $\kappa(\Omega)$  in Figure 3 was used in simulations of propagation through fibers of length 2, 11 and 50 km. Figure 4 shows agreement between the predicted magnitude and phase of  $H(\Omega, z)$  (solid) and the experiment. The two longest fibers had not been used in the original determination of  $\kappa(\Omega)$ .

In the simple rate equation model, the real part of  $\kappa$  is usually assumed to be positive. In this case it can be shown that the phase of  $H(\Omega, z)$  is increasing monotonic. However, as observed in Figure 3, the real part of  $\kappa$  can in fact become negative at some frequencies, at which the phase of  $H(\Omega, z)$  changes monotonicity. This can be observed in the experimental data in Figure 1 and Figure 4, which also indicate that the simple model fails to describe the phase of  $H(\Omega, z)$  at the frequencies at which the real part of  $\kappa$  becomes negative.

### III.1.5 Application: transmission through fiber gratings

As an example of the implications of the frequency dependence of  $\kappa$  in modeling lightwave systems, we consider transmission through fiber gratings. It is known that FM-to-IM conversion can be used to advantage to obtain an increase in modulation response [12] and/or decrease in laser relative intensity noise [13]. The baseband transfer function after transmission through the grating was derived in Chapter II. Given the transmission coefficient of the fiber grating and the laser chirp of the optical source, the separation between Bragg frequency and optical laser frequency that yields optimal performance can be determined.

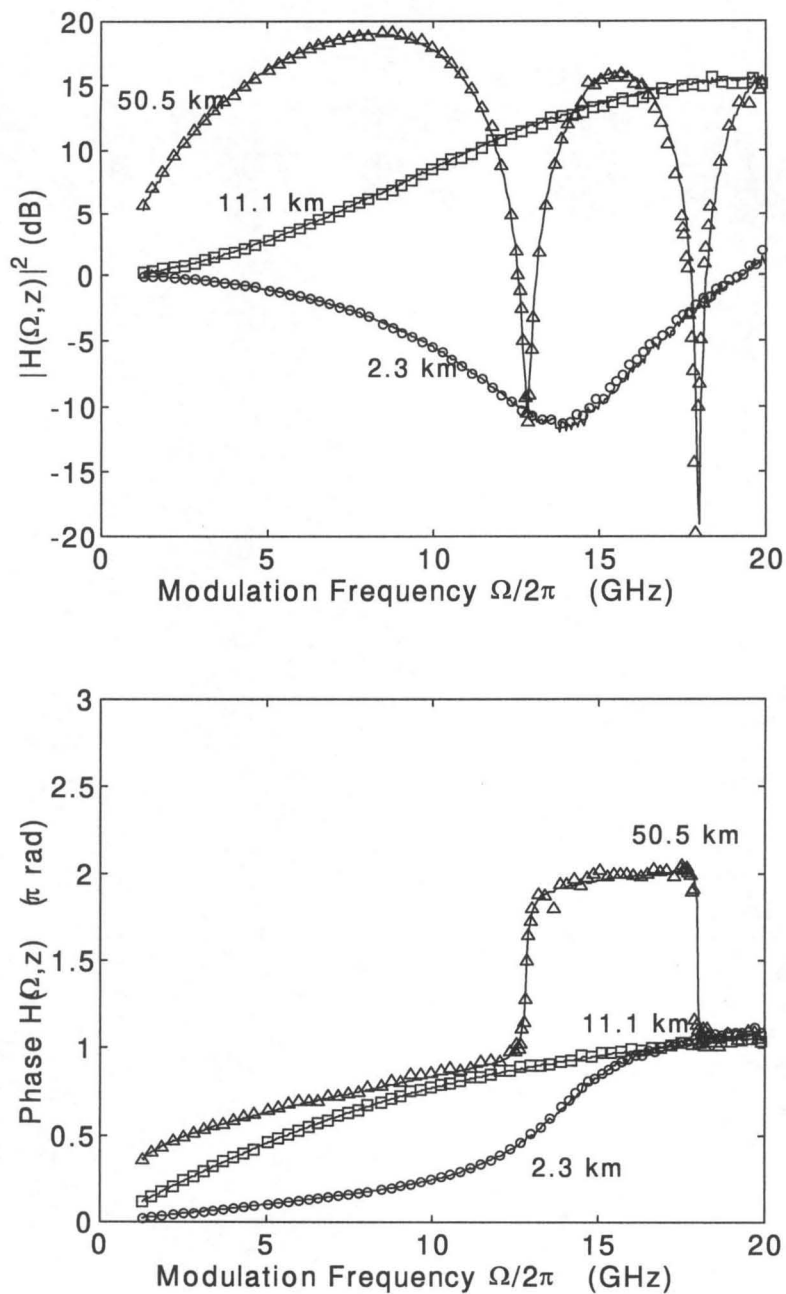


Figure 4: Measured  $H(\Omega, z)$  after 2.3km (circles), 11.1km (squares) and 50.5km (triangles) of standard fiber together with theoretical prediction (solid) using  $\kappa(\Omega)$  in Figure 3. Output power at laser facet is 14.3mW.

The amplitude of the transmission coefficient of a fiber grating vs. optical wavelength was measured using a tunable laser source and an optical power meter. The phase of the transmission coefficient was determined using a Kramers-Kronig transformation as described in [12]. Using this transmission coefficient,  $t(\omega)$ , and the previously determined  $\kappa(\Omega)$ , the baseband transfer function,  $H(\Omega, z)$  after transmission in the grating was predicted. Figure 5 shows  $H(\Omega, z)$  predicted by using the previously determined complex  $\kappa(\Omega)$  (solid) and a constant  $\alpha$  and  $\kappa$  that best fit the change in modulation response after several fiber lengths (dashed) in comparison to the transfer function experimentally measured (circles). Better agreement between simulation and experiment is achieved when precisely measured  $\kappa(\Omega)$  is used to describe the FM of the optical transmitter.

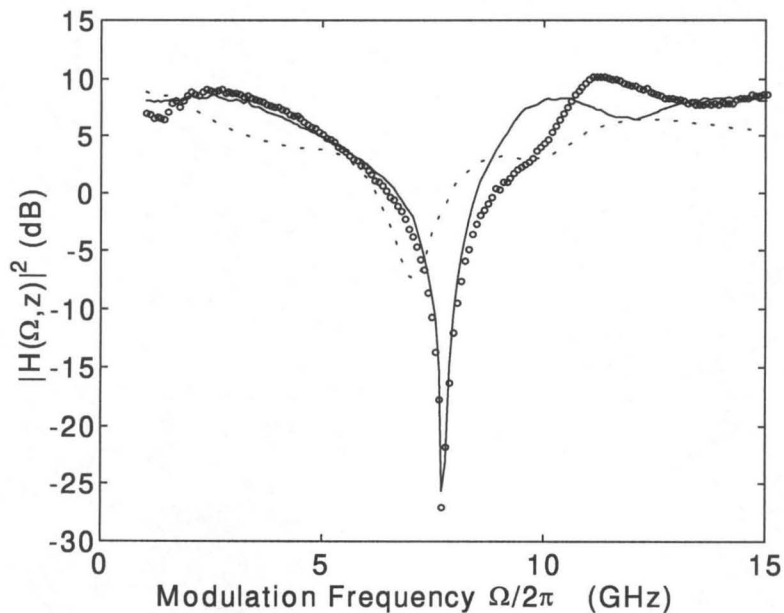


Figure 5: Baseband transfer function after transmission through fiber grating predicted using the measured  $\kappa(\Omega)$  in Figure 3 (solid) and constant  $\alpha$  and  $\kappa$  (dashed) compared to measurement (circles).

## III.2 CHARACTERIZATION OF LASER CHIRP FOR MULTI-QUANTUM-WELL DISTRIBUTED-FEEDBACK LASERS

Important effects that are not considered explicitly in simple laser rate equation analyses of laser chirp include the longitudinal and transverse spatial variations of the optical intensity and/or carrier density. Roughly speaking, these contribute to adiabatic chirp. Sophisticated, mostly numerical, analyses of the dynamic characteristics of multi-quantum well distributed-feedback (MQW-DFB) lasers considering spatial hole burning, carrier transport and carrier capture exist in the literature [8]-[11],[14]-[21], and it is possible to infer from these analyses that in a laser the adiabatic chirp is, in fact, not quite adiabatic.

In this section, the main objective is to determine the influence of the intraband damping mechanisms such as spectral hole burning and carrier heating, the DFB structure and the carrier transport and capture into the QW's on the laser chirp. First, the effect of the spatial hole burning resulting from the DFB laser structure will be evaluated by using numerical simulations for the spatial distribution of carrier and photon density. Next, an approximate unidimensional analytical model of carrier transport and capture in a MQW laser will be presented. From comparison of these models with experimental data it will be concluded that the main reason for the discrepancy between the simple laser chirp model and the measured chirp is the effect of the MQW structure.

The linewidth enhancement factor was determined from measurements of relative intensity noise, modulation response, and linewidth. By using the more detailed laser chirp model including carrier transport and capture, agreement was found among all data, which was not possible otherwise. In addition, the power dependence of the linewidth enhancement factor is shown to explain the saturation of the laser linewidth at high optical powers.

### III.2.1 Analysis of the FM response of DFB lasers including longitudinal spatial hole burning.

#### III.2.1.A Theory of operation of DFB lasers.

Long-haul communication systems usually require an optical source with good spectral purity. This is the main motivation for the use of distributed-feedback (DFB) lasers [22]. These lasers do not utilize the cavity mirrors, but provide the feedback via Bragg backscattering from periodic perturbations of the index and/or gain of the laser medium itself (Figure 6). Coupling between the waves going in the backward and forward direction only occurs for wavelengths satisfying the so-called Bragg condition, which results in enhanced mode selectivity.

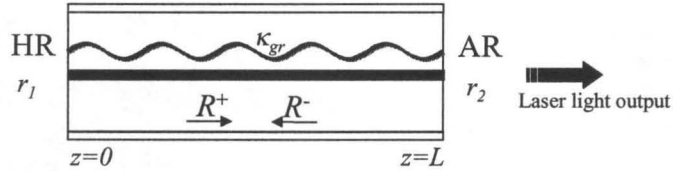


Figure 6: DFB laser structure.

From the wave equation it is possible to derive coupled-wave equations for the forward and backward propagating fields in a periodic structure. These are given by [9],[23]:

$$\pm v_g \frac{\partial R^\pm}{\partial z} + \frac{\partial R^\pm}{\partial t} = -i\Delta\tilde{\omega}R^\pm - i\kappa_g^\pm R^\mp \quad (8)$$

where  $R^\pm(t, z)$  are the complex amplitudes of the forward (+) and backward (-) propagating waves,  $v_g$  is the group velocity and  $\kappa_g^\pm$  are the coupling coefficients, which are related to the amplitude of the periodic perturbation and the overlap between the perturbation and the optical mode field. For a purely index-coupled laser diode,

$$\kappa_g^+ = \kappa_g^- \equiv \kappa_g \quad (9)$$

The complex angular frequency deviation,  $\Delta\tilde{\omega}$ , is given by:

$$-i\Delta\tilde{\omega} = \frac{\Gamma}{2}G - i\Delta\omega - i\frac{\alpha_N}{2}\Gamma G_N(N - N_{th}) \quad (10)$$

where  $\Gamma$  is the confinement factor,  $G$  is the stimulated recombination rate,  $\Delta\omega$  is the deviation of the optical frequency from the Bragg frequency,  $\alpha_N$  is the linewidth enhancement factor as defined by Henry [24]-[26],  $N(t,z)$  is the carrier density,  $G_N = \partial G / \partial N$  is the differential gain, and  $N_{th}$  is the carrier density at threshold.

The carrier density is also a function of time and position, and satisfies the following rate equation:

$$\frac{\partial N}{\partial t} = \frac{I}{eV} - \frac{N}{\tau_c} - GP \quad (11)$$

where  $I$  is the current injection,  $V$  is the laser volume,  $\tau_c$  is the carrier lifetime, and  $P$  is the photon density. In addition,  $G$  is a function of  $N(t,z)$  and  $P(t,z)$ , and  $\tau_c$  is a function of  $N(t,z)$ .

Due to the optical feedback induced by the corrugated structure, the optical field inside the laser cavity becomes intensified at some places, which is accompanied by carrier depletion. Such a local variation of carrier and photon density is known as longitudinal spatial hole burning, and can give rise to adverse effects such as longitudinal mode instability and multimode oscillation. In addition, such carrier and photon density nonuniformity can affect the laser frequency and intensity modulation response.

Equations (8)-(11) fully determine the static and dynamic behavior of the DFB laser. For our purposes, we only need to find the small-signal intensity modulation (IM) and frequency modulation (FM) responses. Then, it is not necessary to solve the nonlinear time-domain system above. It is sufficient to solve first the static laser problem at some bias point and then perform a small-signal analysis around that bias point.

The *static problem* [19] is obtained by omitting the time derivatives in (8)-(11). The resulting equations form a nonlinear boundary value problem, where the boundary

conditions are the facet reflectivities (magnitude and phase). This problem can be transformed into an initial value problem that is solved with an iterative shooting algorithm. The unknowns are the amplitude of the forward propagation field at the beginning of the structure (left facet),  $R^+(z=0)$ , and the lasing wavelength or, equivalently,  $\Delta\omega$ . We can take  $R^+(z=0)$  to be real with no loss of generality. The left boundary condition gives a starting value for  $R^-(z=0)$ . Then the forward and backward fields are propagated through the laser taking into account the photon-carrier interaction self-consistently, which involved solving a nonlinear equation at each step during propagation. At the right facet, another boundary condition must be satisfied. The error is used to give a new estimate for the two unknowns, and then proceed iteratively.

The *small-signal analysis* [17], [20]-[21] is performed, as usual, by assuming a sinusoidal variation of the different variables around the operation point, and linearizing the resulting equations. We will not give the linearized equations because they are too cumbersome although their derivation is straightforward. The equations obtained form a linear set that can be solved by using a finite element method. The FM response is described by the small-signal variation of the phase of the propagating fields at the laser output, and the IM response by the small-signal variation of the intensity.

Some approximate methods for analyzing the effect of spatial hole burning on the dynamic response of DFB lasers have been proposed [14]-[18]. The basic approach is to treat the carrier density as the sum of a spatial-independent term and a small spatial-dependent term, and then solve three spatial-averaged rate equations. However, in our experience, this method does not explain well the chirp of DFB lasers with high reflection (HR) and anti-reflection (AR) facets, as the ones tested in the experiments, and a numerical analysis will be employed.



### III.2.1.B Characterization of DFB lasers using amplified spontaneous emission below threshold.

#### 1) *Theory of amplified spontaneous emission below-threshold.*

In the previous section it was shown how to derive the laser IM and FM response taken into account the spatial hole burning. However, in order to solve the equations above, it is necessary to obtain some laser material and structural parameters. The gain spectrum [27]-[31] together with some structural laser parameters [32]-[34] can be found from measurements of the amplified spontaneous emission (ASE) below threshold. Other parameters such as gain compression and carrier and photon lifetime can be estimated from the laser modulation response and relative intensity noise at the laser output [35]-[38].

The laser spontaneous emission noise was derived by Henry [39] by solving the noise driven wave equation using the Green's function method. Assuming a single-transverse-mode index-guided laser cavity, the average noise power,  $P_N$ , out of the right facet (at  $z = L$ ) within a noise bandwidth  $B_N$  is given by:

$$P_N(z = L) = \hbar\omega B_N n_{sp} g(1 - R_2) \frac{\langle |\Phi(x, y)|^2 \rangle^2 \langle |Z_1(z)|^2 \rangle}{\langle |\Phi\Phi| \rangle^2 |W/(2\beta)|^2} \quad (12)$$

where  $n_{sp}$  is the spontaneous emission factor,  $g$  is the material gain,  $\Phi(x, y)$  is the field transverse profile,  $\beta$  is the propagation constant and  $R_2$  is the magnitude of the reflection coefficient at the right facet. The Green functions are  $Z_1(z)$  and  $Z_2(z)$ , which are solutions to the wave equation satisfying left and right boundary conditions, respectively, and  $W$  is the Wronskian [40].

The spontaneous emission factor is given by [28],[38]:

$$n_{sp} = \frac{1}{1 - e^{(\hbar\omega - \Delta E)/k_B T}} \quad (13)$$

where  $\Delta E$  is the energy separation of the quasi-Fermi level between the conduction and valence band,  $k_B$  is the Boltzmann's constant, and  $T$  is the Kelvin temperature. For a narrow wavelength range around the lasing wavelength, however, a linear approximation for  $n_{sp}(\lambda)$  can be used:

$$n_{sp} \approx n_{sp0} + n_{sp1}(\lambda - \lambda_{Bragg}) \quad (14)$$

where  $\lambda_{Bragg}$  is the Bragg wavelength.

For modes below threshold, the photon density  $P$  can be assumed to be nearly zero and the  $z$ -dependence of the carrier density can be neglected, which greatly simplifies the solution of the Green functions. In the following, we will only consider index-coupled standard DFB lasers with uniform gratings. In this case, analytical expressions for the Green functions below threshold can be found from the coupled wave equations (8).

## 2) *Modified Hakki-Paoli method for DFB lasers.*

Hakki and Paoli devised a simple method [27] to obtain the gain spectrum from measurements of the ASE from a Fabry-Perot (FP) cavity laser. Following the same lines, we have derived a modified Hakki-Paoli method, which can be used to obtain the gain spectrum for DFB cavity lasers.

For an FP laser, the  $P_N$  can be written as follows:

$$P_N(z=L) = \frac{A(\lambda)}{\left(1 - R e^{(g-\alpha_m)L}\right)^2 + 4R e^{(g-\alpha_m)L} \sin^2 \theta} \quad (15)$$

where  $\alpha_m$  is the material background loss and  $L$  is the laser cavity length. The parameters  $R$  and  $\theta$  are real quantities related as [27]:

$$R e^{i2\varphi} = r_1 r_2 \quad (16)$$

$$\theta = 2\delta L - 2\varphi \quad (17)$$

where  $r_1$  and  $r_2$  are the complex facet reflectivities and  $\delta$  is the deviation of the propagation constant from the Bragg condition, that is,

$$\delta = \frac{\Delta\omega}{v_g} \quad (18)$$

For a DFB laser, (15) is only approximately correct for wavelengths sufficiently far from the Bragg wavelength. By solving for the Green functions,  $Z_1(z)$  and  $Z_2(z)$ , and substituting in (12), the following expressions for  $R$  and  $\theta$  can be derived:

$$R e^{i\varphi} = \frac{r_1 r_2 + \frac{\kappa_g}{2\delta} (r_1 + r_2)}{1 - \frac{\kappa_g}{2\delta} (r_1 + r_2)} \quad (19)$$

$$\theta = 2\delta L \left( 1 - \frac{\kappa_g^2 + (g/2)^2}{2\delta^2} \right) - 2\varphi \quad (20)$$

The expression in (15) includes a Fabry-Perot type resonant denominator with maxima and minima for  $\theta = n\pi$  and  $\theta = \frac{\pi}{2} + n\pi$ , respectively, with  $n$  an integer. The spectral dependence of the function  $A(\lambda)$ , which is mainly due to the spectral dependence of  $n_{sp}(\lambda)$  and  $g(\lambda)$ , is much slower than the rapid variation of the denominator. As a consequence, the wavelength dependence of  $A(\lambda)$  for adjacent maxima and minima can be neglected. Then, a function  $Q(\lambda)$  can be defined as:

$$Q(\lambda) = \frac{P_{N_{\max}}^{1/2}(\lambda) - P_{N_{\min}}^{1/2}(\lambda)}{P_{N_{\max}}^{1/2}(\lambda) + P_{N_{\min}}^{1/2}(\lambda)} \quad (21)$$

where  $P_{N_{\max}}$  and  $P_{N_{\min}}$  are the values of adjacent maxima and minima, which can be shown to yield the laser material gain and loss as follows:

$$g(\lambda) - \alpha_m = \frac{1}{L} \ln \frac{Q(\lambda)}{\sqrt{R_1 R_2}} \quad (22)$$

$$\alpha_m = -\frac{1}{L} \ln \frac{Q(\infty)}{\sqrt{R_1 R_2}} \quad (23)$$

In addition, the group refractive index,  $n_g$ , can be obtained far from the Bragg wavelength from the Fabry-Perot mode spacing.

### 3) *Determination of laser parameters from ASE.*

With all the previous elements it is now possible to outline a procedure to extract several important laser parameters. First, the ASE spectrum,  $P_N(\lambda)$ , has to be measured, and from that the Hakki-Paoli function  $Q(\lambda)$  in (21) has to be computed. Another known laser parameter is usually the cavity length,  $L$ . The unknowns are the complex facets reflectivities,  $r_1$  and  $r_2$ , the grating coupling coefficient,  $\kappa_g$ , the material gain,  $g(\lambda)$ , and loss,  $\alpha_m$ , the group refractive index,  $n_g$ , the Bragg wavelength,  $\lambda_{Bragg}$ , and the spontaneous emission factor,  $n_{sp}(\lambda)$ .

The algorithm to obtain all these laser parameters is described in the flow-chart in Figure 7.

Good initial guesses are necessary for rapid convergence of the search algorithm. Some of these can be obtained from knowledge of the laser structure or from simple observation of the ASE spectrum. As an example, the lasers that were tested had high-reflection (HR) and anti-reflection (AR) coatings at the facets. For this type of lasers, it is found that:

- The phase of  $r_1$  (HR facet) determines the position of the lasing wavelength inside the stopband.
- The phase of  $r_2$  (AR facet) determines the peak-to-valley ratio for the side modes.
- The magnitude of  $\kappa_g$  determines the width of the stopband.

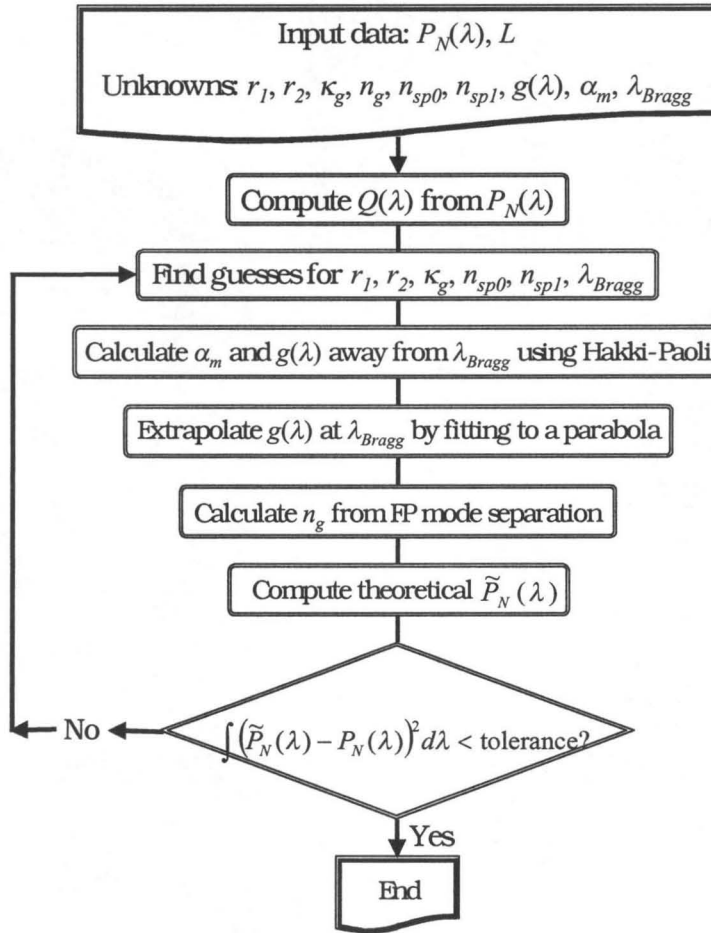


Figure 7: Flow chart for determination of laser parameters from measurements of below threshold ASE spectrum.

### III.2.1.C Experiment

In order to evaluate the effect of spatial hole burning on the laser chirp of the laser tested in section III.1.4, first the laser was characterized using measurements of ASE below threshold, and modulation response and relative intensity noise above threshold. These laser parameters were used for simulations of the DFB structure as explained in section III.2.1.A.

Figure 8 shows the measured ASE spectrum at two bias currents and the fitting to the theory above (solid). The laser threshold current was 23mA. The measured gain spectrum at several bias currents is shown in Figure 9. It is observed that the gain at the lasing wavelength is clamped above threshold.

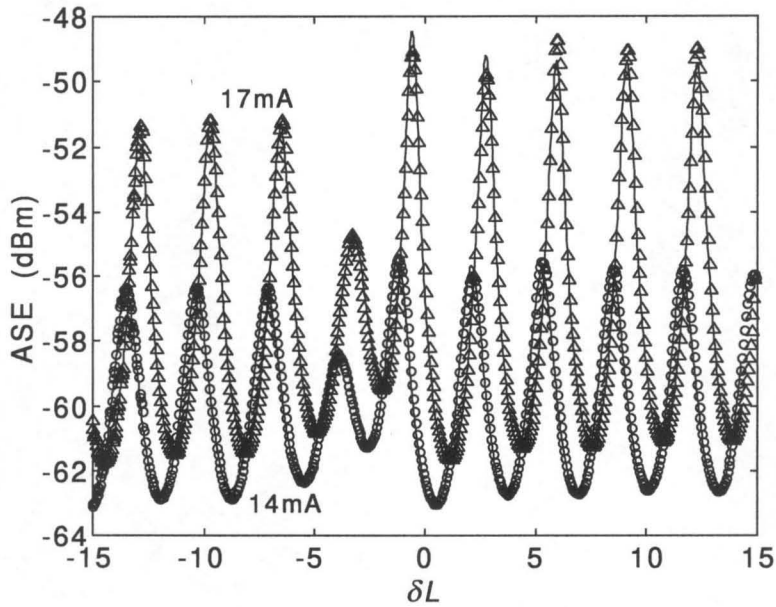


Figure 8: Below threshold ASE spectrum at bias currents 14mA (circles) and 17mA (triangles). Solid is theory.

It has been shown that the maximum material gain for a quantum well laser follows a simple logarithmic relation with the current density below threshold [41]-[42]. This can be expressed as:

$$g - \alpha_m = \sigma_i \ln \frac{I}{I_0} \quad (24)$$

where  $I_0$  is the injection current at which the gain equals the material loss. This expression has been confirmed in our experiments, as shown in Figure 10.

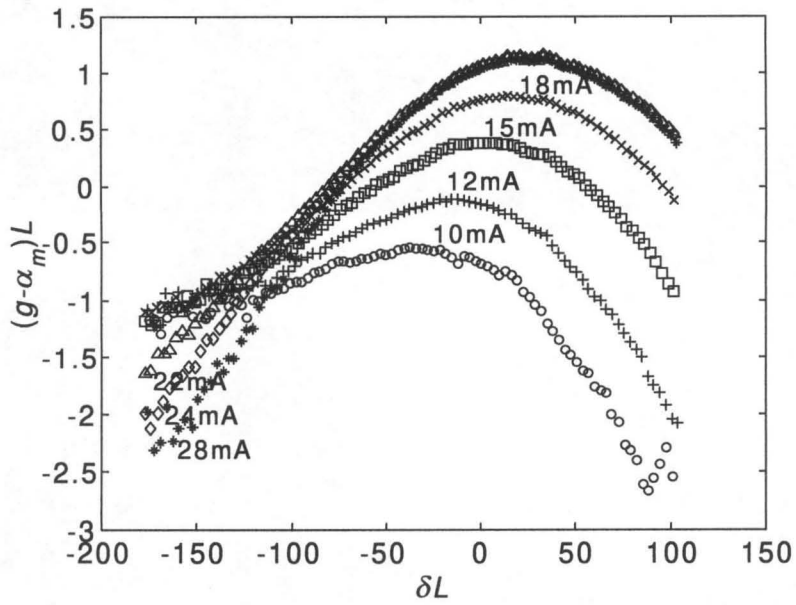


Figure 9: Gain spectrum at several bias currents.

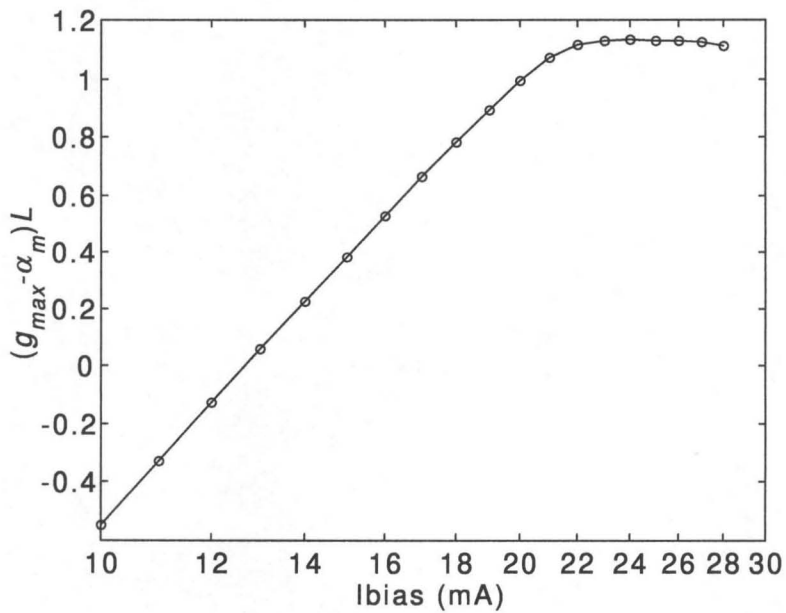


Figure 10: Logarithmic maximum gain-current relation.

The steady state analysis yields the spatial distribution of the carrier density (Figure 11) and of the photon density (Figure 12). The photon density is maximum at the left HR facet, and then decreases to reach a minimum near the right AR facet. The carrier density is maximum at this spatial "hole" of the photon density. A small-signal analysis around the bias current yields the *PIR*, and from that and using (4) the equivalent frequency-dependent  $\kappa$  can be extracted (Figure 13). Comparison of Figure 3 and Figure 13 clearly indicates the spatial hole burning cannot explain the measured frequency dependence of  $\kappa$ . In fact, the approximate analyses in [14]-[18] indicate that the effect of spatial hole burning can only be observed at low frequencies, since the dynamics of the carrier density are limited by the large carrier lifetime.

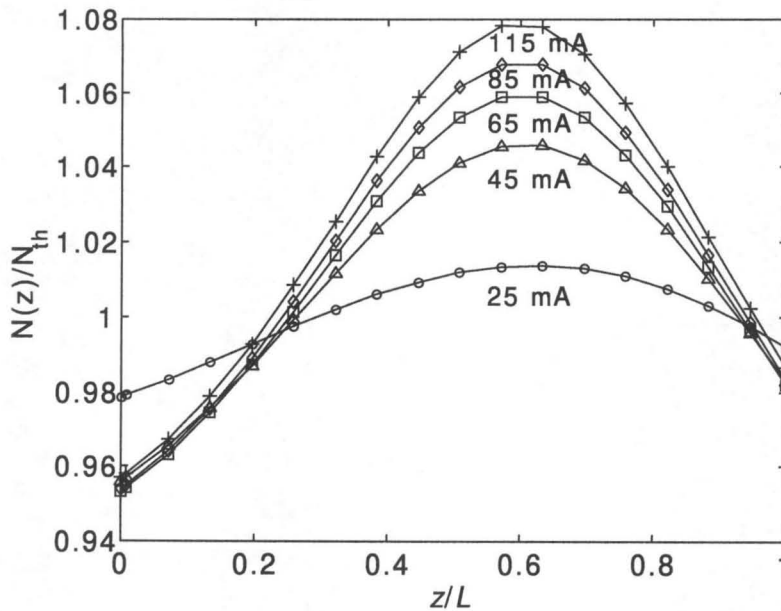


Figure 11: Spatial dependence of the carrier density normalized by the carrier density at threshold for several bias currents.



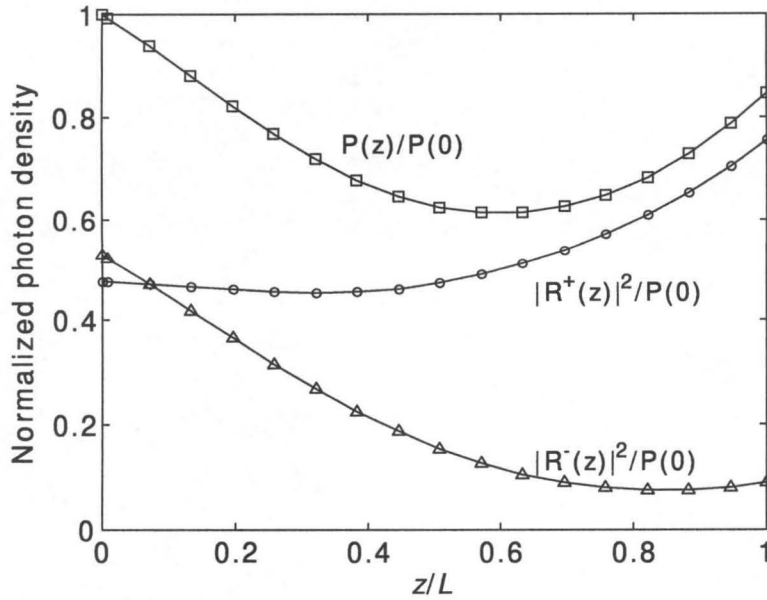


Figure 12: Spatial dependence of the photon density and the forward and backward field amplitudes normalized by the photon density at the left facet. Bias current is 85mA.

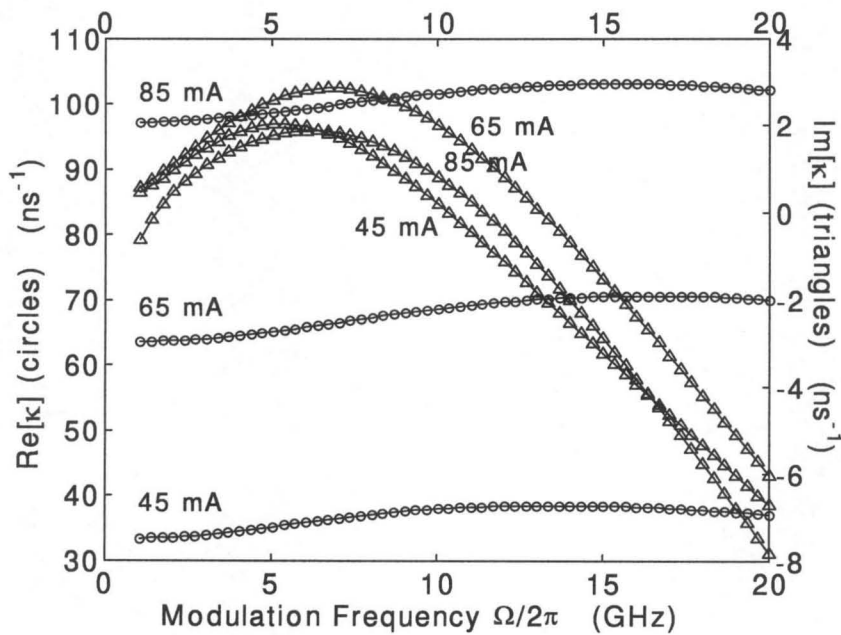


Figure 13: Real (circles) and imaginary (triangles) part of  $\kappa(\Omega)$  at several bias currents. We assumed  $\alpha_N=-4.5$  at all bias currents.

### III.2.2 Analysis of the FM response of MQW lasers including carrier transport and capture.

Multi-quantum well lasers are expected to possess very large modulation bandwidths owing to a large differential gain. However, large gain compression had been observed for these lasers, which limits the predicted advantages. A new phenomenological model, the “reservoir” model, considered the consequence of a capture and escape time of the carrier between the separate confinement (SCH) region and the quantum wells [43]. This model has been further expanded to accurately explain the carrier dynamics of MQW lasers and results in analytical expressions for the intensity modulation (IM) [44]-[50] and frequency modulation (FM) [10],[51] of the laser.

In this section, the reservoir model is introduced and used to derive expressions for the *PIR* of MQW lasers. The predictions from this model are then compared with experimental data of modulation response after propagation in fiber. The relative importance of intraband damping mechanisms, carrier transport and capture and spatial hole burning is evaluated. In addition, this model allows precise determination of the linewidth enhancement factor,  $\alpha$ , from measurements modulation response after fiber that agrees well with the values obtained from relative intensity noise after fiber and linewidth. The power dependence of  $\alpha$  is shown to explain the saturation of linewidth at high optical powers.

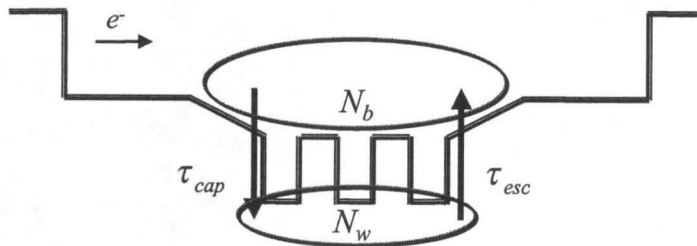


Figure 14: Reservoir model for quantum well lasers.

### III.2.2.A Reservoir model for MQW lasers

The reservoir model is illustrated in Figure 14. There are two distinct reservoirs, one for the confined electrons in the quantum wells,  $N_w$ , and another for the unconfined electrons in the SCH region,  $N_b$ . The exchange of carriers between these two reservoirs is characterized by time constants  $\tau_{cap}$  and  $\tau_{esc}$  for effective capture and escape from the quantum wells, respectively. The rate equations describing small variations in unconfined carrier density,  $\Delta N_b$ , and confined carrier density,  $\Delta N_w$ , are given by:

$$\frac{d\Delta N_b}{dt} = \frac{\Delta I}{eV_{SCH}} - \left( \frac{\Delta N_b}{\tau_{cap}} - \frac{\Delta N_w}{\eta_V \tau_{esc}} \right) - \frac{\Delta N_b}{\tau_b} \quad (25)$$

$$\frac{d\Delta N_w}{dt} = \eta_V \left( \frac{\Delta N_b}{\tau_{cap}} - \frac{\Delta N_w}{\eta_V \tau_{esc}} \right) - \frac{\Delta N_w}{\tau_w} - G_N P_0 \Delta N_w - \left( \frac{1}{\Gamma_w \tau_{ph}} - G_P P_0 \right) \Delta P + \frac{F'_N}{V_{QW}} - \frac{F_P}{V_{QW}} \quad (26)$$

Here,  $\Delta P$  is the small-signal photon density variation,  $\Delta I$  is the modulation current;  $F'_N$  and  $F_P$  are uncorrelated Langevin carrier and photon noise sources (see section III.3);  $P_0$  is the average photon density;  $G_N = \partial G / \partial N_w$  is the differential gain with  $G$  the stimulated recombination rate in the wells;  $G_P = -\partial G / \partial P$  describes the dependence of  $G$  on photon density or gain compression,  $\Gamma_w$  is the confinement factor of the confined carriers in the quantum wells,  $\tau_{ph} = 1 / \Gamma_w G$  is the photon lifetime and  $\tau_w$  and  $\tau_b$  are the differential carrier lifetimes for confined and unconfined carriers, respectively. The parameter  $\eta_V$  expresses the fact that the confined carrier density is assumed to occupy the volume of the quantum wells, whereas the unconfined carrier density is assumed to be contained in the SCH region. Thus,

$$\eta_V = \frac{V_{SCH}}{V_{QW}} \quad (27)$$

where  $V_{SCH}$  is the volume of the SCH region and  $V_{QW}$  is the total volume of the quantum wells.

The photon density in the quantum wells is described by the standard rate equation, with only the confined carriers participating in the lasing transitions,

$$\frac{d\Delta P}{dt} = \Gamma_w G_N P_0 \Delta N_w - \Gamma_w G_P P_0 \Delta P + \Gamma_w \frac{F_P}{V_{QW}} \quad (28)$$

There are two contributions to the capture and escape times. One is the carrier diffusion time across the SCH region, and the other is phonon-assisted quantum transitions between confined and unconfined states. For lasers with a very wide SCH region, the capture time can be primarily due to carrier diffusion in the SCH region.

The problem of carrier transport within the SCH region is not a simple one, since electrons and holes are injected separately from opposite ends of this region. However, experimental evidence such as in [48] and later in this section indicate that a simple ambipolar unidimensional model might suffice to explain the key features of the intensity and frequency modulation response. In the case of single quantum well lasers it has been shown [45]-[46] that solution of this simple classical diffusion model along with a phenomenological model for the quantum capture and escape at the quantum well leads to effective capture and escape times that can be used in the reservoir model. Following the same approach, and neglecting diffusion along the barriers, it can be shown that the same equations apply to MQW lasers with effective capture and escape times related as:

$$\tau_{cap} = \eta_V \tau_{cap}^Q + \frac{L_{SCH}^2}{8D} \quad (29)$$

$$R_{ce} = \frac{\tau_{cap}}{\tau_{esc}} = \eta_V \frac{\tau_{cap}^Q}{\tau_{esc}^Q} \quad (30)$$

where  $\tau_{cap}^Q$  and  $\tau_{esc}^Q$  are the intrinsic quantum capture and escape times,  $L_{SCH}$  is the length of the SCH region and  $D$  is the diffusion coefficient.

1) *Intensity modulation response.*

Solution of the small-signal rate equations (25)-(28) for a sinusoidal current at modulation angular frequency  $\Omega$  yields:

$$\Delta P = \frac{\Gamma_w G_N P_0 \left( \frac{\Delta I_Q(\Omega)}{eV_{QW}} + \frac{F'_N}{V_{QW}} \right) + \frac{\Gamma_w F_P}{V_{QW}} \left( i\Omega + \frac{1}{\tau_w} + \frac{1}{\tau_Q(\Omega)} \right)}{D_0 + \frac{1}{\tau_Q(\Omega)} (i\Omega + \Gamma_w G_P P_0)} \quad (31)$$

$$\Delta N_w = \frac{1}{\Gamma_w G_N P_0} \left[ (i\Omega + \Gamma_w G_P P_0) \Delta P - \frac{\Gamma_w F_P}{V_{QW}} \right] \quad (32)$$

$$\eta_V \Delta N_b = \frac{R_{ce}}{1 + \tau_{cap} / \tau_b + i\Omega \tau_{cap}} \Delta N_w + \tau_{cap} \frac{\Delta I_Q(\Omega)}{eV_{QW}} \quad (33)$$

where

$$D_0 = (i\Omega)^2 + i\Omega\gamma_0 + \Omega_0^2 \quad (34)$$

is the resonant denominator of the modulation response when carrier transport and capture effects are neglected, with the relaxation frequency,  $\Omega_0$ , and the damping coefficient,  $\gamma_0$ , given by:

$$\Omega_0^2 = \frac{G_N P_0}{\tau_{ph}} + \frac{\Gamma_w G_P P_0}{\tau_w} \quad (35)$$

$$\gamma_0 = \frac{1}{\tau_w} + \Gamma_w G_P P_0 + G_N P_0 \quad (36)$$

Comparison of (31)-(32) with the results for bulk lasers indicate that  $\Delta I_Q(\Omega)$  can be considered the effective current injection into the quantum wells, and  $\tau_Q(\Omega)$  is an additional effective non-radiative recombination time due to the finite effective capture time. They are given by:

$$\Delta I_Q(\Omega) = \frac{\Delta I}{1 + \tau_{cap} / \tau_b + i\Omega \tau_{cap}} \quad (37)$$

$$\frac{1}{\tau_Q(\Omega)} = R_{ce} \frac{i\Omega + 1/\tau_b}{1 + \tau_{cap}/\tau_b + i\Omega\tau_{cap}} \quad (38)$$

For frequencies smaller than the inverse of the effective capture time,  $\tau_{cap}$ , the photon density,  $\Delta P$ , and confined carrier density,  $\Delta N_w$ , variations can be well modeled by the same two-pole expressions as for a bulk laser.

## 2) Frequency modulation response.

Changes in confined and unconfined carrier density,  $\Delta N_w$  and  $\Delta N_b$ , and photon density,  $\Delta P$ , affect the gain or absorption in a semiconductor material, and through a Kramers-Kronig relation, also the optical frequency,  $\omega_0$ . Thus, frequency variations,  $\Delta\omega$ , obey the equation:

$$\Delta\omega = \frac{d\Delta\phi}{dt} = -\frac{\omega_0}{n_g} \Delta n' = -\frac{\omega_0}{n_g} \left[ \Gamma_w \frac{\partial n'}{\partial N_w} \Delta N_w + \Gamma_{sch} \frac{\partial n'}{\partial N_b} \Delta N_b + \Gamma_w \frac{\partial n'}{\partial P} \Delta P \right] + F_\phi \quad (39)$$

where  $n_g$  is the group index,  $n'$  is the real part of the effective modal refractive index,  $\Gamma_{sch}$  is the confinement factor of the carriers in the SCH region, and  $F_\phi$  is a Langevin noise source for phase fluctuations.

From (39), the small-signal phase variation in the frequency domain can be expressed as:

$$i\Omega\Delta\phi = -\frac{\alpha_N}{2} \Gamma_w G_N (\Delta N_w + \xi\eta_V \Delta N_b) + \frac{\alpha_P}{2} \Gamma_w G_P \Delta P + F_\phi \quad (40)$$

Here,  $\alpha_N$  is the linewidth enhancement factor as defined by Henry [24]-[26],

$$\alpha_N = \frac{\partial n'}{\partial N_w} / \frac{\partial n''}{\partial N_w} \quad (41)$$

with  $n''$  the imaginary part of the effective refractive index. The parameter  $\alpha_P$  was first introduced by Agrawal [52]-[54], and gives the change in refractive index with a change in photon density as follows:

$$\alpha_p = \frac{\partial n'}{\partial P} \bigg/ \frac{\partial n''}{\partial P} \quad (42)$$

Finally,  $\xi$  is related to the ratio between the refractive index change due to a change in confined and unconfined carrier densities,

$$\xi = \frac{1}{\eta_V} \frac{\Gamma_{sch}}{\Gamma_w} \frac{\partial n'}{\partial N_b} \bigg/ \frac{\partial n'}{\partial N_w} \cong \frac{\partial n'}{\partial N_b} \bigg/ \frac{\partial n'}{\partial N_w} \quad (43)$$

### 3) Phase to intensity modulation index ratio.

The phase to intensity (modulation index) ratio (*PIR*) determines, as explained in Chapter II, the intensity modulation response of the laser after transmission in a dispersive channel. Uncorrelated driving sources will not beat at the receiver, and can thus be considered separately. Substitution of Eq. (31)-(33) into (40) yields the *PIR* due to current variations,  $\Delta I$ :

$$i\Omega PIR|_{\Delta I} = i\Omega \frac{\Delta\phi}{\Delta P/P_0} \bigg|_{\Delta I} = -\frac{\alpha_N}{2} (1 + R_{ce}\xi) (i\Omega + \Gamma_w G_P P_0) - \frac{\alpha_N}{2} \xi \tau_{cap} D_0 + \frac{\alpha_P}{2} \Gamma_w G_P P_0 \quad (44)$$

and the *PIR* due to the photon noise source,  $F_p$ ,

$$\begin{aligned} i\Omega PIR|_{F_p} &= i\Omega \frac{\Delta\phi}{\Delta P/P_0} \bigg|_{F_p} = \\ &= \frac{\alpha_N}{2} G_N P_0 \frac{i\Omega + 1/\tau_{ph}}{i\Omega + 1/\tau_w + 1/\tau_Q} \left[ 1 + \frac{R_{ce}\xi}{1 + i\Omega\tau_{cap} + \tau_{cap}/\tau_b} \right] + \frac{\alpha_P}{2} \Gamma_w G_P P_0 \end{aligned} \quad (45)$$

### 4) Linewidth.

The laser linewidth is given by [55]:

$$\Delta\nu = \frac{\langle |\Delta\omega(\Omega)|^2 \rangle \big|_{\Omega=0}}{2\pi} \quad (46)$$

From (31),(40) it can be shown that:

$$\Delta\nu = \Delta\nu_{ST} \left[ 1 + \alpha_N^2 (1 + R_{ce}\xi)^2 \right] \quad (47)$$

where  $\Delta v_{ST}$  is the Schawlow-Townes linewidth and the contribution from the second term in (40) corresponding to  $\beta$  was neglected.

### 5) Discussion.

Equation (33) indicates that the carrier density in the barrier,  $\Delta N_b$ , is comprised of two terms. The first one follows the dynamics of the confined carrier density whereas the second follows the current modulation signal. The first term contributes a factor  $(1 + R_{ce}\xi)$  to the linewidth enhancement factor, as can be observed in the first part of (44) and in (47). From equation (45), this is also the main consequence in the RIN for frequencies smaller than the inverse of the capture time. The second term in (33) only affects the modulation response, since it is proportional to the current modulation. Since it does not follow the photon density dynamics, the resonance denominator that describes the photon density variation appears in the numerator of the *PIR* in (44).

Comparison of (44) and (4) yields the following expression for the equivalent  $\kappa(\Omega)$ ,

$$\kappa(\Omega) = \Gamma_w G_P P_0 + \frac{\xi \tau_{cap}}{1 + R_{ce}\xi} \left( (i\Omega)^2 + i\Omega\gamma_0 + \Omega_0^2 \right) = \Gamma_w G_P P_0 + \frac{\xi \tau_{cap}}{1 + R_{ce}\xi} D_0 \quad (48)$$

where  $\alpha$  was defined as that that would be directly measured from linewidth (and RIN for small  $\tau_{cap}$ ), that is:

$$\alpha = \alpha_N (1 + R_{ce}\xi) \quad (49)$$

The first term in (48) is the same that arises from the standard rate equations. If the gain is expressed as  $G(N, P) = G_N (N - N_{th})(1 - \varepsilon P)$ , then the well-known expression [6] for a bulk laser  $\kappa = \Gamma_w G_P P_0 = \varepsilon P_0 / \tau_{ph}$  is obtained. The second term comes from the fact that, as explained above, the unconfined carrier density does not completely follow the photon dynamics. Three effects can be derived from (48), first a parabolic decrease of the real part of  $\kappa$  as the modulation frequency increases, second an increase in the transient chirp proportional to the damping factor, and third an increase in the low-frequency



adiabatic chirp proportional to the relaxation frequency squared. The parabolic characteristic of the real part of  $\kappa$  could well explain the features observed in Figure 3.

### III.2.2.B Experiment

According to equation (48),  $\kappa(\Omega)$  is described by a second order polynomial in  $(i\Omega)$ . However, it was found that the experimental data is more precisely described by a higher order polynomial such as

$$\kappa(\Omega) = \kappa_0 + \kappa_1(i\Omega) + \kappa_2(i\Omega)^2 + \kappa_3(i\Omega)^3 \quad (50)$$

The additional coefficient,  $\kappa_3$ , gives some curvature to the imaginary part of  $\kappa(\Omega)$  that is also observed in the numerical simulations including spatial hole burning in Figure 13. This, in addition to the conclusions that are extracted from approximate analyses of the DFB structure [14]-[18], suggests that spatial hole burning could be the explanation for this coefficient. Figure 3 shows the fitting of the measured  $\kappa(\Omega)$  to an expression such as in (50).

Identification of the coefficients  $\kappa_0$ ,  $\kappa_1$  and  $\kappa_2$  in (50) with the parabolic expression of  $\kappa(\Omega)$  in (48) yields:

$$\kappa_0 = \Gamma_w G_p P_0 + \kappa_2 \Omega_0^2 \quad (51)$$

$$\kappa_1 = \kappa_2 \gamma_0 \quad (52)$$

$$\kappa_2 = \frac{\xi \tau_{cap}}{1 + R_{ce} \xi} \quad (53)$$

Figure 15 shows the coefficients  $\kappa_0$ ,  $\kappa_1$  and  $\kappa_2$  as a function of laser output power for the laser chirp measured in section III.1.4 and displayed in Figure 3. Since  $\Omega_0^2$  and  $\gamma_0$  increase linearly with laser power, so do  $\kappa_0$  and  $\kappa_1$ . According to Figure 15 the coefficient  $\kappa_2$  also increases with output power, and this will be justified below.

The laser linewidth was measured using a self-heterodyne technique [56]. The white and 1/f components of the frequency noise spectrum were estimated by fitting the

lineshape to a Voigt profile [57], and  $\alpha$  was obtained from the white component using (47) and (49). Measurements of relative intensity noise (RIN) at the laser output, which are parasitic-free as opposed to the modulation response, were used to determine  $\Omega_0$ ,  $\gamma_0$ ,  $\tau_w$ , and  $\Delta v_{ST}$ . Fitting of the RIN to the expression in (31) is very sensitive to initial guesses and does not always converge. Instead,  $\Omega_0$  and  $\gamma_0$  were obtained from the RIN for fixed values of  $\tau_{cap}$  and  $R_{ce}$ .  $\tau_{cap}$  and  $R_{ce}$  were determined so as to obtain best agreement among the values for  $\alpha$  obtained from the coefficients  $\kappa_0$  and  $\kappa_1$ , from measurement of RIN after propagation in dispersive fiber [58] and from linewidth. The values reported for  $R_{ce}$  in the literature vary from 0.01 to 0.5. For our lasers,  $R_{ce}$  was negligibly small and, as a consequence, it was possible to approximate  $1/\tau_Q \approx 0$  in equations (31), (45) and  $\alpha \approx \alpha_N$ .

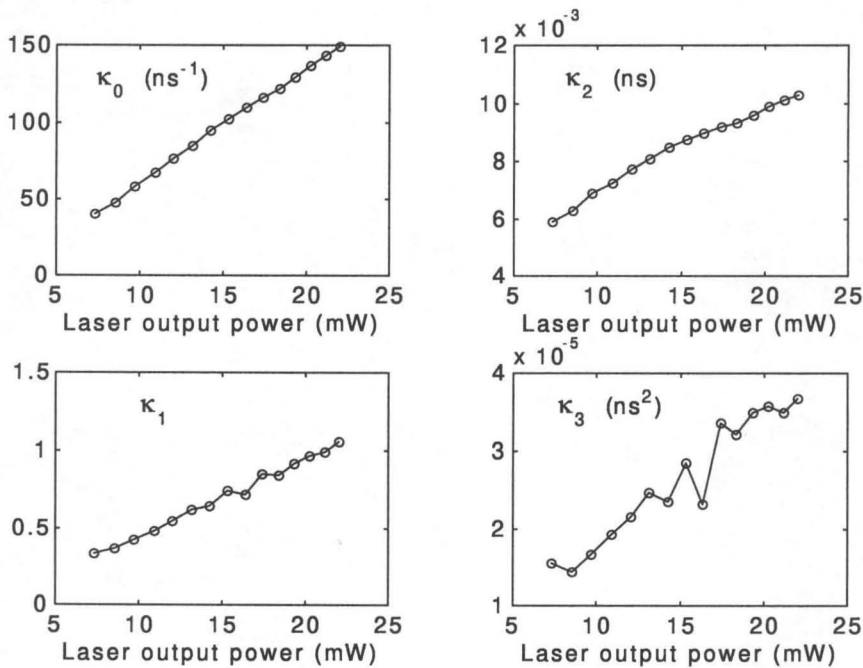


Figure 15: Coefficients from fitting  $\kappa(\Omega)$  in Figure 3 to polynomial in equations (50).

Figure 16 shows  $\xi\tau_{cap}$  for three different lasers. The value of  $\xi\tau_{cap}$  increases as the optical power increases, and seems to correlate with the laser threshold intensity, i.e., carrier density. As opposed to the carrier density in the wells,  $N_w$ , the carrier density in the barriers,  $N_b$ , is not clamped, but increases with current injection,  $I$ , as  $\eta_V N_b \cong R_{ce} N_w + \tau_{cap} I / eV_{sch}$ . Above a critical carrier density, which for our lasers is estimated at  $N_b \approx 5 \times 10^{16} \text{ cm}^{-3}$ , band-gap shrinkage effects contribute to a strong increase of the magnitude of  $\partial n' / \partial N_b$  with carrier density in the barrier [59]. On the other hand,  $\tau_{cap}$  is expected to increase for larger carrier density in barrier due to a smaller diffusion coefficient and a larger quantum capture time [60]. A combination of both effects can explain the power dependence of  $\xi\tau_{cap}$  in Figure 16. However, both contributions are difficult to separate and an independent measurement of  $\xi$  or  $\tau_{cap}$  would be necessary.

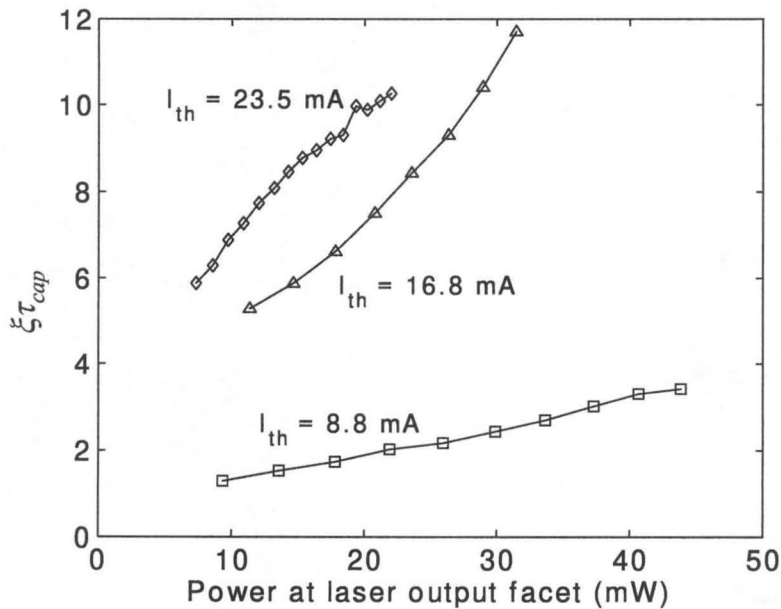


Figure 16: Measured  $\xi\tau_{cap}$  for three MQW-DFB lasers with different threshold intensities.

The values for  $\alpha$  obtained from measurements of linewidth,  $\kappa_0$ ,  $\kappa_1$  and RIN after fiber are shown in Figure 17 as a function of laser output power. Agreement of all the four measurements is found. The power dependence of  $\alpha$  can explain the saturation of the linewidth at high optical powers. It was found that the power dependence of  $\alpha$  originates mainly from the power dependence of  $G_N$ , as determined from  $\Omega_0$ , which is also expected theoretically, since the carrier density in the wells is clamped and as a consequence  $\partial n' / \partial N_w$  is practically independent of optical power.

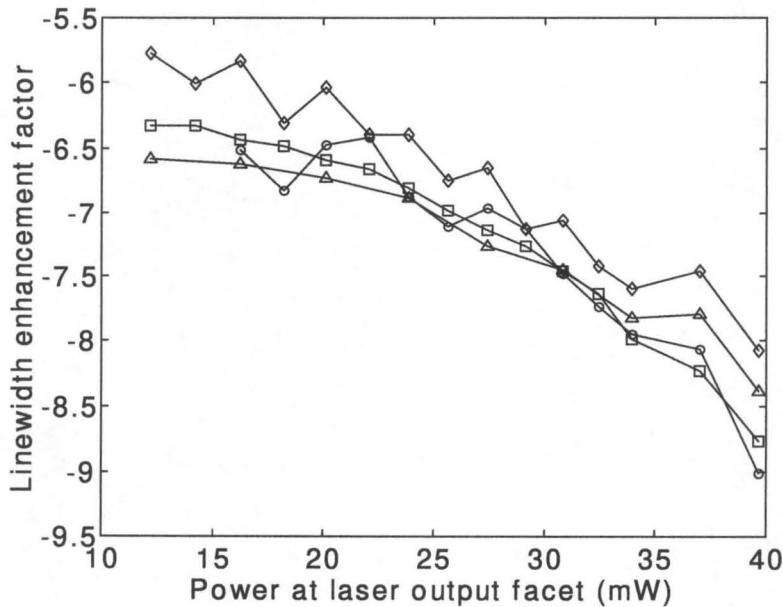


Figure 17: Linewidth enhancement factor as determined from  $c_0$  (circles),  $c_1$  (squares), RIN after fiber (triangles) and linewidth (diamonds). The inset shows the measured linewidth, and the expected linewidth (solid) with power independent  $\alpha_N$ .

### III.3 EFFECT OF MANY WEAK SIDE MODES ON RELATIVE INTENSITY NOISE OF DISTRIBUTED FEEDBACK SEMICONDUCTOR LASERS

When the link includes propagation in dispersive optical fiber, the relative intensity noise (RIN) at the fiber output (i.e., at the receiver) can be different from the RIN at the laser due to phase noise to intensity noise conversion.

In addition to effects which can be described by a single-mode laser theory [61], the side modes in a nearly-single-mode laser contribute to RIN. Mode partition noise (MPN) in a laser is the fluctuation of optical power among the modes in such a way that the total power remains unchanged. After propagation in dispersive fiber, MPN can be converted to laser excess noise and hence, increased RIN at the receiver [62]-[63]. This is one of the factors that lead to the choice of nearly-single-mode DFB lasers in communication applications.

An effect of MPN has been observed that affects RIN in low noise lasers even when the side-mode suppression ratio (SMSR) is greater than 35 dB. Since the gain spectrum in semiconductor lasers is broad, there usually exists a broad spectrum of weak Fabry-Perot side modes. These modes, while greatly suppressed relative to the main mode, together can contribute enough power to affect the RIN in some circumstances. In this section, experimental evidence is given for this effect and a theory that accounts well for the observed phenomenon is presented.

#### III.3.1 Theory

Any laser mode,  $i$ , is driven by its spontaneous emission, which can be considered as a Langevin noise source acting on that mode,  $F_p$  for photon noise source and  $F_\phi$ . If the photon number, as driven by spontaneous emission, is raised, more

carriers are consumed. Since there is essentially only one carrier reservoir for all laser modes, and above threshold this carrier population is clamped, spontaneous emission into one mode will reduce spontaneous emission in the other modes. Thus, a spontaneous emission event into one mode is anticorrelated with a spontaneous emission event in another mode, yielding a low total relative intensity noise.

The carrier density fluctuations,  $\Delta N$ , and photon density and phase fluctuations,  $\Delta P_i$  and  $\Delta \phi_i$ , at each mode  $i$ , at modulation frequency  $\Omega$  can be obtained by using small-signal rate equations. Nonlinear phenomena such as spectral and spatial hole burning are included here phenomenologically by using an expression for the gain which includes dependence on the photon density of each cavity mode:

$$G_i = \overline{G}_i + G_{N_i} \Delta N - \beta_i \Delta P_i - \sum_{j \neq i} \theta_{ij} \Delta P_j \quad (54)$$

where  $G_{N_i} = \frac{\partial G_i}{\partial N}$  is the differential gain for mode  $i$ , and  $\beta_i = -\frac{\partial G_i}{\partial P_i}$  governs nonlinear self-compression of the gain for mode  $i$ , whereas  $\theta_{ij} = -\frac{\partial G_i}{\partial P_j}$  accounts for the fact that gain in one mode  $i$  is affected by the optical power in the other modes  $j \neq i$ . Since these derivatives are evaluated at the steady-state operation point, they can be laser output power dependent. The resulting small-signal rate equations are [61]:

$$(j\Omega + \Gamma_N) \Delta N = \frac{F_N}{V} - \sum_i \overline{G}_i \Delta P_i \quad (55)$$

$$(j\Omega + \Gamma_{P_i}) \Delta P_i = \frac{\Gamma F_{P_i}}{V} + \Gamma G_{N_i} P_i \Delta N - \sum_{j \neq i} \Gamma \theta_{ij} P_i \Delta P_j \quad (56)$$

$$j\Omega \Delta \phi_i = -\frac{\alpha_i}{2} \Gamma G_{N_i} \Delta N + F_{\phi_i} \quad (57)$$

with  $\Gamma_N = \frac{1}{\tau_c} + \sum_i G_{N_i} P_i$ ,  $\Gamma_{P_i} = \frac{R_{sp_i}}{P_i} + \Gamma \beta_i P_i$  and  $\overline{G}_i = \overline{G}_i - \beta_i P_i - \sum_{j \neq i} \theta_{ji} P_j$ .

In the above equations  $\Gamma$  is the optical confinement factor,  $\tau_c$  is the differential spontaneous carrier lifetime,  $R_{sp_i}$  is the spontaneous emission rate per unit volume into the mode  $i$ , and  $\alpha_i$  is the linewidth enhancement factor. The terms  $F_N$ ,  $F_{P_i}$  and  $F_{\phi_i}$  are Langevin noise sources associated with carrier recombination and spontaneous emission into mode  $i$ .

Equations (55)-(57) can be easily solved numerically. However, more insight is gained by making some approximations that are valid in the case of nearly-single-mode lasers. The gain margin of the  $i^{\text{th}}$  mode,  $\overline{\Delta G_i}$ , which is defined as the difference between the inverse of the photon lifetime and the gain for that mode, is related to the CW photon density,  $P_i$ , according to  $\overline{\Delta G_i} = \frac{R_{sp_i}}{P_i}$  [64]. For side modes below threshold, the gain margin is large compared to dynamic variations in the gain and dominates the rate at which the photon density fluctuations are damped. Hence, for a side mode,  $\Delta P_i$  is approximately independent of fluctuations in the carrier density and the photon density of the other modes. From (56) we get:

$$\Delta P_i \cong \frac{\Gamma F_{P_i}}{V} \left/ \left( j\Omega + \frac{R_{sp_i}}{P_i} \right) \right., \quad i \neq 0 \quad (58)$$

where the main lasing mode has been assigned the subscript zero.

The photon density fluctuations of each of the side modes,  $\Delta P_i$ , affect the carrier density and photon density and phase of the main mode,  $\Delta P_0$ . Since the Langevin forces  $F_{P_i}$  of different modes are uncorrelated, the  $\Delta P_i$  (for  $i \neq 0$ ) can then be considered as independent noise sources in (55)-(57) (for  $i = 0$ ). Using the approach adopted in [61] we eliminate the correlation between  $F_{P_i}$  and  $F_N$  by using  $F_N = F'_N - \sum_i F_{P_i}$ , where  $F'_N$  is the part of the noise not involving spontaneous emission of photons into one of the longitudinal modes.

The photon and carrier density variations in the main mode are given by:

$$\Delta P_0 = \Delta P_0^{N'} + \Delta P_0^{P_0} + \sum_{i \neq 0} \Delta P_0^{P_i} \quad (59)$$

$$\Delta N = \Delta N^{N'} + \Delta N^{P_0} + \sum_{i \neq 0} \Delta N^{P_i} \quad (60)$$

Here, two superscripts are used to denote the different contributions to the fluctuations  $\Delta N$ ,  $\Delta P_0$  and  $\Delta \phi_0$ . The first superscript indicates the physical origin of the noise term, either carrier noise ( $N'$ ) or spontaneous emission originating photon density noise ( $P$ ) and phase noise ( $\phi$ ). In the case of spontaneous emission, a second superscript shows in which mode,  $0$  or  $i$ , the spontaneous emission takes place.

Upon substitution of (58) into the rate equations (55) and (56), the contributions originating from carrier noise,  $\Delta P_0^{N'}$  and  $\Delta N^{N'}$ , and from spontaneous emission in the main mode,  $\Delta P_0^{P_0}$  and  $\Delta N^{P_0}$ , are found to be approximately the same as those obtained with single-mode theory. The additional fluctuations caused by the side modes are given by

$$\Delta P_0^{P_i} = - \left[ G_{N_0} P_0 \frac{j\Omega + \Gamma_{P_i} + \Gamma \overline{G_i}}{D(\Omega)} + \Gamma \theta_{0i} P_0 \frac{j\Omega + \frac{1}{\tau_c} + G_{N_0} P_0}{D(\Omega)} \right] \Delta P_i = p_{0i} \Delta P_i \quad (61)$$

and

$$\Delta N^{P_i} = \frac{1}{\Gamma G_{N_0} P_0} [j\Omega + \Gamma \beta_0 P_0 + p_{0i} \Gamma \theta_{0i} P_0] \Delta P_i \quad (62)$$

where the factor  $D(\Omega) = -\Omega^2 + j\gamma_0 \Omega + \Omega_0^2$  is the resonant denominator, with  $\gamma_0$  and  $\Omega_0$  the damping factor and resonant frequency of the main mode [61]. These can be well approximated by the values obtained with single mode theory in the case of a DFB laser.

From equations (57) and (62), the phase fluctuation in mode  $i$  due to spontaneous emission in mode  $j$  is given by:

$$\Delta \phi_i^{P_j} = -\frac{\alpha_i}{2} \frac{G_{N_i}}{j\Omega} \Gamma \Delta N^{P_j} \quad (63)$$



Equation (61) shows the additional fluctuation in the photon density of the main mode, which is anti-correlated with the noise source  $\Delta P_i$  that originates it. Two physical effects are present: first, depletion of carriers due to spontaneous and stimulated emission into the  $i^{\text{th}}$  side mode, and second, compression of the gain of the main mode by the power in the side modes.

The effect of the side modes is only important at frequencies well below the relaxation resonance frequency of the main mode. Closer to resonance  $\Delta P_0^{P_0}$  dominates over  $\Delta P_0^{P_i}$  and  $\Delta P_i$ , and beyond resonance the side mode fluctuation is highly damped due to its low-pass characteristic, as seen in equation (58). At frequencies below  $1/\tau_c$  and  $\overline{G_0}$ , the inverse of the response time of carriers and photons, respectively, the carrier and photon density are adiabatically related, and since in this regime the carrier density is clamped,  $\Delta N$  is practically zero. Considering the effect of  $\Delta P_i$  separately, spontaneous emission into the side mode  $i$  tends to decrease the carrier density, as does stimulated emission into the side mode and the main mode. Hence the condition  $\frac{F_{P_i}}{V} + \overline{G_i} \Delta P_i + \overline{G_0} \Delta P_0^{P_i} \approx 0$  has to be satisfied. This relation can also be easily derived from the rate equations (55)-(57) if we ignore gain compression. Unless the side mode is so weak that the number of photons in the side mode is comparable to the number of photons originated by spontaneous emission, the factor corresponding to the stimulated gain dominates. Taking  $\overline{G_i} \approx \overline{G_0}$ , which is a valid approximation for the dominant side modes since the gain spectrum of semiconductor lasers is quite broad ( $\sim 50\text{nm}$ ), we end up with  $\Delta P_0^{P_i} \sim -\Delta P_i$ . This negative correlation between the noise caused by  $F_{P_i}$  in the main mode and the side mode is what causes cancellation of the mode partition noise *at the output of the laser* when we compute the total relative intensity noise (RIN).

For a multimode laser, the total detected intensity is the sum of the intensity in each mode. Since the different noise sources are uncorrelated, the spectral densities of the fluctuations are additive and therefore we can consider their effects individually.

The total RIN at the receiver in the case of a nearly-single-mode laser will then be given by:

$$RIN(\Omega, z) \approx RIN_0(\Omega, z) + \sum_{i \neq 0} \frac{\langle |H_0^{P_i} \Delta P_0^{P_i} + H_i^{P_i} \Delta P_i|^2 \rangle}{P^2} \quad (64)$$

where  $RIN_0$  is the RIN obtained with single-mode theory in [61], and the second term is the additional noise that comes from the side modes. We have used the fact that the magnitude of fluctuations caused by the conversion between the frequency chirp (FM) and the intensity modulation (AM) is weighted by the power in the mode (see equation (65) below). Consequently, the phase noise in the side modes,  $F_{\phi_i}$ , can be neglected. In equation (64),  $H_i^{P_i}(\Omega)$  is the small-signal transfer function for propagation of intensity variations of the mode  $i$  driven by  $F_{P_i}$ . This transfer function is a generalization of  $H_2(\Omega)$  in [61], which corresponds to  $H_0^{P_0}(\Omega)$  in the present notation, for the multimode case. In the case of propagation through dispersive optical fiber  $H_i^{P_i}(\Omega)$  is found to be:

$$H_i^{P_i}(\Omega) = \left[ \cos(\theta) - 2P_i \frac{\Delta \phi_i^{P_i}}{\Delta P_i^{P_i}} \sin(\theta) \right] \exp(j\vartheta_i) \quad (65)$$

where  $\theta = -\frac{1}{2}\beta_2\Omega^2 z$  and  $\vartheta_i = -\beta_2\Delta\omega_i\Omega z$ , with  $\beta_2$  the fiber group velocity dispersion coefficient,  $z$  the fiber length and  $\Delta\omega_i$  the optical frequency spacing between mode  $i$  and the main mode. The factor  $\exp(j\vartheta_i)$  accounts for the group delay of side modes relative to the main mode.

Substitution of (62) and (63) into (65) yields:

$$\begin{aligned} \frac{\langle |H_0^{P_i} \Delta P_0^{P_i} + H_i^{P_i} \Delta P_i|^2 \rangle}{P^2} &\cong |\cos(\theta)(\exp(j\vartheta_i) + p_{0i}) + p_{0i}\alpha_0 \sin(\theta)|^2 \frac{\langle |\Delta P_i|^2 \rangle}{P^2} \approx \\ &\approx \{4 \sin^2(\vartheta_i/2) [1 - \alpha_0 \beta_2 \Omega^2 z]\} \frac{\langle |\Delta P_i|^2 \rangle}{P^2} \end{aligned} \quad (66)$$

The approximation in the last line of (66) consists of neglecting the modal dependence of the linewidth enhancement parameter,  $\alpha_i$ , and the differential gain,  $G_{N_i}$ , and assumes a large SMSR. Also, since  $p_{0i}$  is close to -1, and the dependence of the nonlinear coefficients on wavelength is weak,  $p_{0i}\beta_0 + \theta_{0i} \approx 0$ . Equation (66) is one of the main results of this paper and explains why even highly suppressed side modes can contribute significantly to the RIN after propagation in dispersive fiber. As a consequence of the difference in group velocities of the longitudinal modes in dispersive fiber, fluctuations originating in the side modes no longer cancel out after propagation, but instead cause oscillations in the noise power at the receiver. Making the assumption  $p_{0i} \approx -1$ , which is, as justified above, a rough approximation for the frequency range where the effect becomes important, the contribution to the RIN from spontaneous emission into the side mode  $i$  after propagation is approximately given by:

$$\frac{\langle |H_0^{P_i} \Delta P_0^{P_i} + H_i^{P_i} \Delta P_i^{P_i}|^2 \rangle}{P^2} \approx \{4 \sin^2(\vartheta_i/2) [1 - \alpha_0 \beta_2 \Omega^2 z]\} \frac{\langle |\Delta P_i|^2 \rangle}{P^2} \quad (67)$$

Taking a mean value for the oscillating term, we see that there is an overall increase in the RIN that rolls off at high frequencies due to the low-pass characteristic of the noise source,  $\Delta P_i$ . The last approximation in equation (66) is valid for  $|\theta| \ll 1$ , that is, for small propagation distance and moderate frequencies. As in the single-mode case [61], excess noise for side modes is reduced after propagation when the product  $\alpha\beta_2 > 0$  is positive.

In order that MPN have a significant contribution at a given modulation frequency,  $\vartheta_i$  has to be close to  $\pi(1+2m)$  for one or several of the dominant side modes, where  $m$  is an integer. The frequency separation between the main mode and the  $i^{\text{th}}$  mode is given approximately by  $|\Delta\omega_i| \sim |i| \frac{2\pi c}{L}$ , with  $L$  the laser length,  $c$  the speed of light and  $i$  the mode index. Thus, assuming a typical value  $\beta_2 = -20 \text{ps}^2/\text{km}$  at

1.55  $\mu\text{m}$ , the condition above becomes  $\Omega \approx \frac{(1+2m)L/z}{|i|2c|\beta_2|} \approx 0.1 \frac{(1+2m)L(\mu\text{m})}{|i|z(\text{km})}$ . If the length of the laser in  $\mu\text{m}$  divided by the mode number,  $L(\mu\text{m})/|i|$ , is much larger than the propagation distance  $z$  in km, the frequencies at which the previous condition is satisfied are so high that an increase in RIN is no longer seen. These conditions hold for short lengths of fiber and side modes close to the main mode.

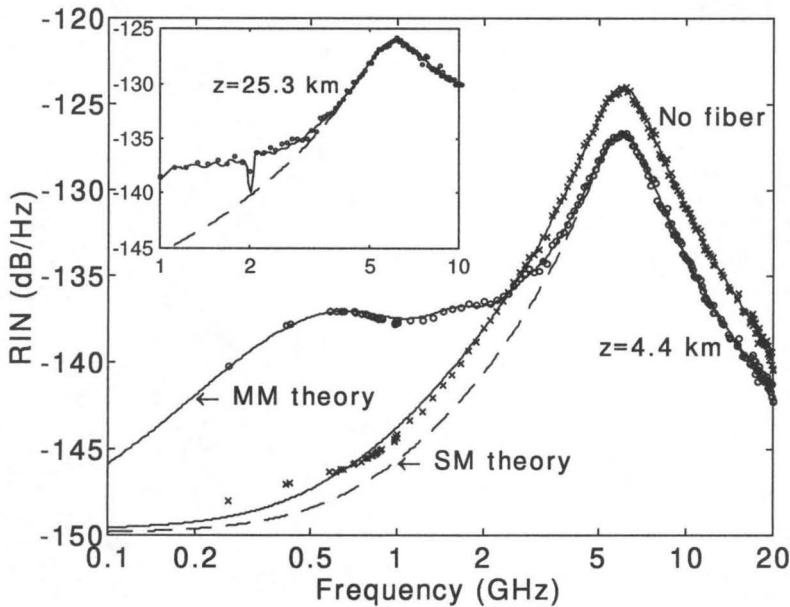
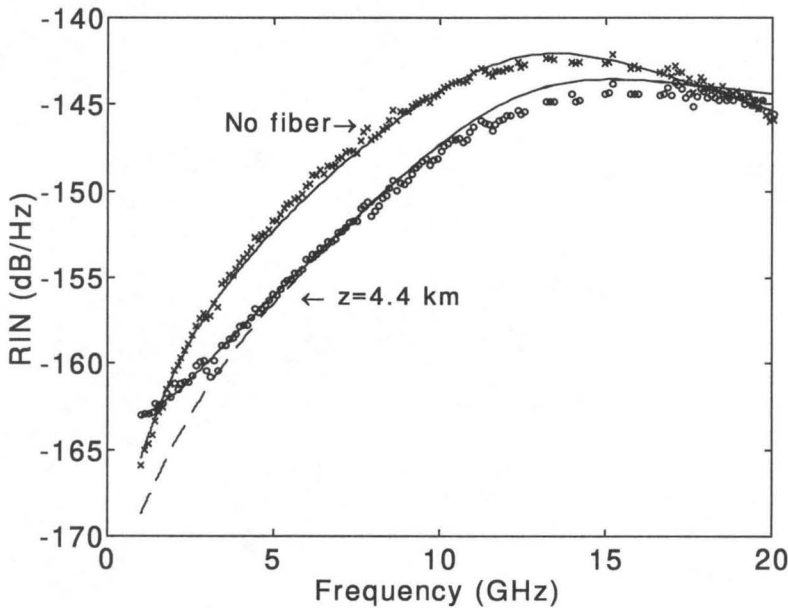


Figure 18: RIN at laser output (crosses) and after 4.4 km and 25.3 km of fiber (circles). The laser output power is  $P_{out}=3.4\text{mW}$ ,  $I_{bias}=1.6I_{th}$  and  $\text{SMSR}=27\text{dB}$ . The solid curve is the multimode (MM) theory and the dashed curve is the single-mode (SM) theory.

### III.3.2 Experiment

The relative intensity noise of the same laser used in the laser chirp experiment (section III.1) was measured before and after propagation in various lengths of standard single mode optical fiber (see Figure 18-Figure 19). A good fit to the standard single

mode theory was obtained before adding fiber. However, an increase in the RIN over the frequency range of 500 MHz to 5 GHz depending on fiber length and laser output power was observed when RIN after propagation was measured. This could not be explained using previous theories such as that by Su *et al.* [65]-[66],  $1/f$  noise [67] or noise originating from  $F'_N$  [68]. The theory presented above provides a very satisfactory explanation of all the features observed in the RIN.



**Figure 19:** RIN after 4.4 km of fiber. The laser output power is  $P_{out}=16.4\text{mW}$ ,  $I_{bias}=4.1I_{th}$  and SMSR=39dB. Same notation as in Figure 18.

Although the side modes in the stop band of the DFB laser are highly suppressed, there are many Fabry-Perot cavity modes that have similar power over a large bandwidth (Figure 20-Figure 21). Including only the strongest side mode in the calculations, the theory does not predict what is experimentally observed.

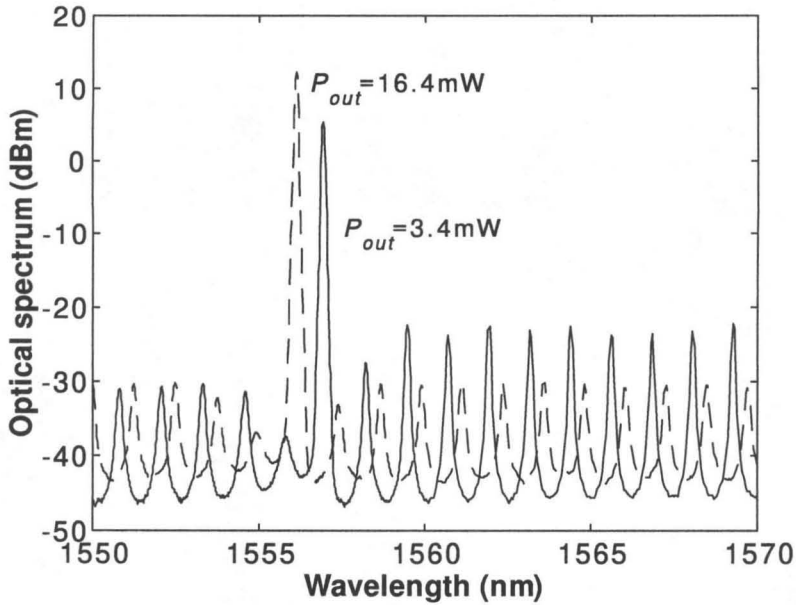


Figure 20: Measured optical spectrum at  $P_{out}=3.4\text{mW}$  (solid) and  $P_{out}=16.4\text{mW}$  (dashed) vs. wavelength.

The measured optical spectrum (Figure 20) was used to determine the power in  $\sim 40$  side modes together with their separation,  $\Delta\omega_i$ , from the main mode (Figure 21), and these data were input to our model. Since there is no need to numerically solve equations, a large number of side modes could be included in the analysis. Equation (66) was used, and the nonlinear gain coefficients were assumed to have a wavelength dependence as that in [66]. If we do not account for gain dispersion and mode dependent spontaneous emission rate, the effect of MPN is overestimated. Here both effects phenomenologically are included by subtracting a fitting parameter to the SMSR that came up between 0.5dB and 1.5dB depending on operation bias current. The measured RIN without fiber was used to determine  $R_{sp0}$ ,  $\gamma_0$  and  $\Omega_0$  at each operation point. The rest of the parameters were estimated from the RIN with fiber so as to obtain the best fits, yielding  $\alpha=-4.6$ ,  $\tau_c=0.27\text{ns}$ ,  $\tau_{ph}=5.5\text{ps}$  and  $\beta_2=-20\text{ps}^2/\text{km}$ .

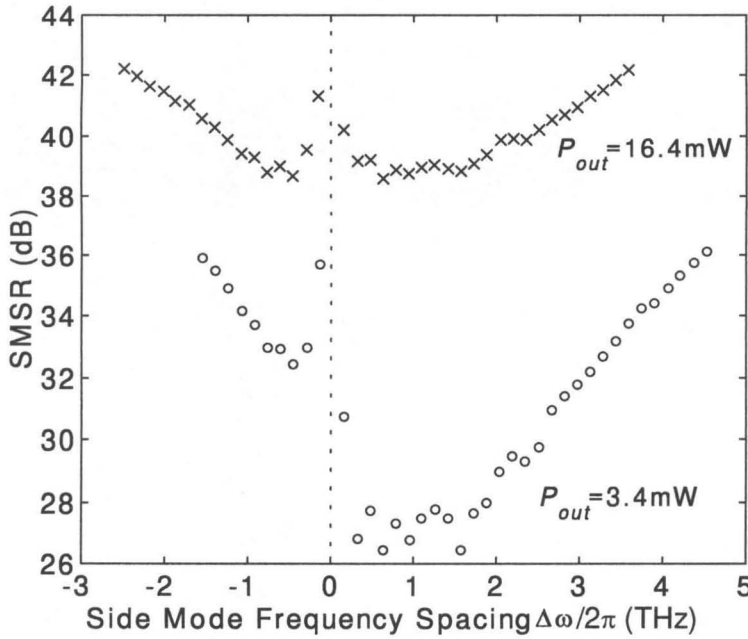


Figure 21: Side mode suppression ratio at  $P_{out}=3.4\text{mW}$  (circles) and  $P_{out}=16.4\text{mW}$  (crosses) vs. frequency deviation from the main mode.

The measured RIN after propagation in several fiber lengths and for different laser output powers is shown in Figure 18 and Figure 19. For some fiber lengths the single-mode theory predicts a reduction in RIN [61], which is not necessarily achieved experimentally due to these multimode effects. In the inset of Figure 18, the notch corresponds to the condition that  $\frac{1}{2}\beta_2\Delta\omega\Omega z$  is an integer multiple of  $\pi$ , with  $\Delta\omega$  the mean mode spacing, at which point all modes arrive at the detector in phase. The effect of MPN is observed even at high output powers and SMSR's (Figure 19).

A similar increase in RIN has also been observed when a grating is used as optical filter, and our model can be readily extended to treat this problem.

### III.4 REDUCTION OF LASER RIN AND RESHAPING OF MODULATION RESPONSE USING A FIBER BRAGG GRATING.

The relative intensity noise (RIN) can be a critical factor in determining the system signal-to-noise ratio. In addition, the laser modulation response (MR) exhibits a resonance peak and subsequent damping that can distort high-speed signals. It had been previously shown that transmission through a uniform grating can improve the laser modulation response [12] and affect the RIN [13], but simultaneous RIN reduction and improvement in MR was yet to be demonstrated.

In this section, it is theoretically shown that a fiber Bragg grating can indeed lead to a major reduction of laser RIN and at the same time shape the MR in an almost arbitrary way. This theory was applied to the experimental RIN reduction and MR flattening for one laser. The index of refraction profile required to obtain the desired grating reflectivity was synthesized by using the iterative Gel'fand-Levitan-Marchenko method [69], and a fiber grating was recorded according to it. The experimental results demonstrate reduction in RIN greater than 5dB over a frequency range of 15 GHz and improvement in the modulation bandwidth.

#### III.4.1 Theory

In a semiconductor laser, fluctuations in the photon density,  $\Delta P$ , are accompanied by variations in the phase of the optical field,  $\Delta\phi$ . Thus, for any mechanism, intentional (signal) or random (noise), which modulates the photon density, the laser output light exhibits correlated intensity modulation (IM) and frequency modulation (FM). In Chapter II, the small-signal theory for propagation of light with IM and FM in an optical filter with an optical transfer function  $t(\omega)$  was presented. It was shown that upon photodetection, the two modulation sidebands beat with the carrier to give the baseband signal at  $\Omega$ . In the optical domain, the amplitude and phase of the two



sidebands relative to the carrier can be independently controlled, which gives us four degrees of freedom that can be used to specify the magnitude and phase of the baseband transfer functions,  $H(\Omega, z)$ , for two different driving sources.

In this case,  $H(\Omega, z)$  is specified for the Langevin photon noise source  $F_p$ , and for a current modulation,  $\Delta I$ . Thus, the two conditions are cancellation of the RIN arising from  $F_p$ ,

$$H(\Omega, z)\Big|_{F_p} = H_e + 2i H_o PIR_{F_p} = 0 \quad (68)$$

and reshaping of the MR,

$$H(\Omega, z)\Big|_{\Delta I} = H_e + 2i H_o PIR_{\Delta I} = H_{\Delta I}(\Omega) \quad (69)$$

where  $PIR_{F_p}(\Omega)$  and  $PIR_{\Delta I}(\Omega)$  are the  $PIR$ 's corresponding to photon noise and modulation current driving sources.

The MR after propagation through the grating would be that before the gratings multiplied by  $H_{\Delta I}(\Omega)$ .

Using the expressions derived in Chapter II for  $H_e$  and  $H_o$ , the required transmission of the optical filter,  $t(\omega)$ , is found as:

$$t(\omega_0 + \Omega)t^*(\omega_0) = H_{\Delta I}(\Omega) \left( 1 + \frac{i}{2PIR_{F_p}(\Omega)} \right) \Bigg/ \left( 1 - \frac{PIR_{\Delta I}(\Omega)}{PIR_{F_p}(\Omega)} \right) \quad (70)$$

The value of  $t(\omega)$  at the laser frequency,  $\omega_0$ , yields the DC insertion loss,  $L_{DC}$ , as follows:

$$L_{DC} = \frac{1}{|t(\omega_0)|^2} = \left( 1 - \frac{PIR_{\Delta I}(0)}{PIR_{F_p}(0)} \right) \Bigg/ H_{\Delta I}(0) = \left( 1 + \frac{\kappa(0)}{\tau_c \Omega_0^2} \right) \Bigg/ H_{\Delta I}(0) \quad (71)$$

Equation (70) indicates that in principle any function  $H_{\Delta I}(\Omega)$  can be specified. The only constraint is that for a passive optical filter,  $|t(\omega)| < 1$ .  $H_{\Delta I}(\Omega)$  will have to be scaled by a factor so as to satisfy this condition, which results in enhanced insertion loss. In

addition, equation (71) shows that the insertion loss increases as the relaxation frequency decreases and as the DC adiabatic chirp is raised.

Lasers also exhibit phase noise uncorrelated with the photon noise, which can be converted to intensity noise after transmission through a dispersive element. However, this noise contribution is much smaller than the photon noise and can be neglected. In fact, optimization of  $t(\omega)$  so as to minimize the total noise from the photon and phase noise sources yields, for typical laser parameters, practically the same function as in (70).

The noise performance will deviate from this theory for lasers with large sidemodes. The bandwidth of optical filters is usually much less than the laser gain bandwidth, and usually even less than the side mode separation. As explained in section III.3, these side modes contribute noise at photodetection that is anticorrelated with noise in the main mode, and thus cancels it. The filter removes the side modes, and as a consequence all noise in the main mode is detected. This effect is especially important at low frequencies and for lasers with poor side mode suppression ratio (SMSR).

### III.4.2 Experiment

The application considered here is that of flattening the MR of the laser. This modulation response is characterized by a peak near the resonance frequency,  $\Omega_0$ , and subsequent damping at a rate  $\gamma_0$ . The baseband transfer function for a current modulation,  $H_{\Delta I}(\Omega)$ , was set to be the inverse of the MR. A laser similar to those used in the previous experiments but with a better SMSR was used in the measurement. The laser parameters,  $PIR_{F_p}(\Omega)$  and  $PIR_{\Delta I}(\Omega)$ , at a bias current of 110mA were determined by measuring the MR and RIN before and after propagation in dispersive fiber. Since compensation of the laser damping at high modulation frequencies can only be done at the expense of insertion loss, the bandwidth had to be limited to 15GHz. Using (70),  $t(\omega)$  was determined.

The desired  $t(\omega)$  was realized in the form of a fiber grating in reflection. In [69] it was theoretically demonstrated that the transfer function of a grating in reflection is

uniquely related to a profile of index of refraction, and a method was given, the iterative Gel'fand-Levitan-Marchenko method, to obtain the required profile of the index of refraction for any reflection coefficient. Here, this method was applied to obtain the profile of the index of refraction for the previously determined  $t(\omega)$ .

This work was done in collaboration with the Institute of Optical Research in Sweden, where the grating was written by using their multiple fringes printing technique as described in [70]. This consists of superposing a short interference pattern onto the fiber whose motion is controlled interferometrically. The fiber is moved slowly, and a pulsed UV laser is triggered every time the fiber has reached a desired position. The pulse duration is only 20ns and the fiber hardly moves during the exposure. The length of the interference pattern is typically 0.2 mm and determines the spatial resolution of the index and phase profiles that can be realized. Figure 22 shows the measured (circles) and specified (solid) reflection spectrum of the grating.

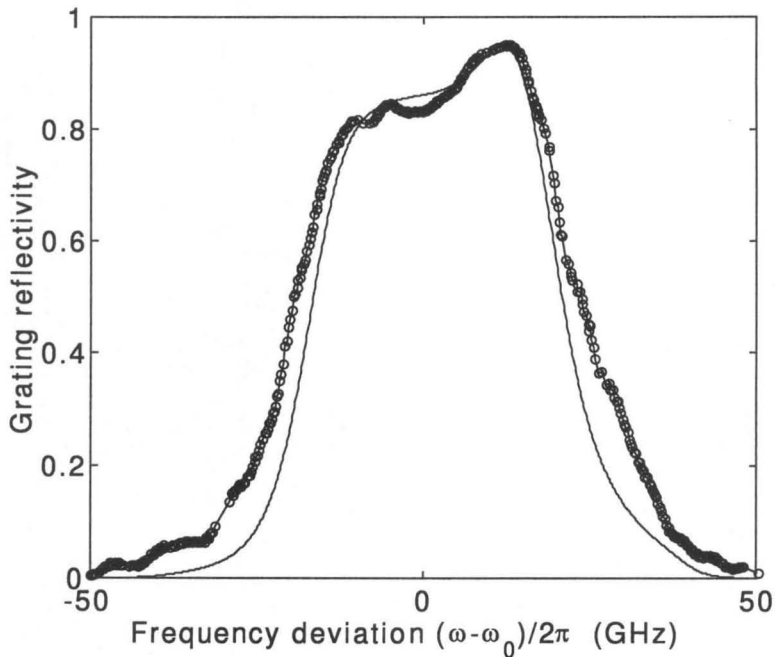


Figure 22: Reflection spectrum around the laser optical frequency.

The laser RIN and MR were measured at the laser output and after reflection from the fiber grating for bias currents from 50mA to 130mA. The laser wavelength had to be temperature tuned to match the grating Bragg wavelength at each bias current. For RIN measurements at the laser output the power was attenuated to the same value as that after the grating, so as to ensure that the power loss in the circulator was not affecting the RIN measurement. Reductions in RIN over 5dB were obtained in the frequency range from 3GHz to 20GHz at all bias currents. Using (70) it was found that indeed the filter performance in terms of RIN reduction is affected by changes in the carrier lifetime,  $\tau_c$ , in the low frequency range,  $\Omega < \tau_c$ , and the photon lifetime,  $\tau_{ph}$ , in the high frequency range,  $\Omega > \tau_{ph}$ , both of which are relative insensitive to the bias current. However, it was not affected so much by variations of other laser parameters such as resonance frequency,  $\Omega_0$ , damping coefficient,  $\gamma_0$ , or linewidth enhancement factor,  $\alpha$ . Thus, the same grating should perform well for different lasers with similar structure. On the contrary, the MR is highly dependent on  $\Omega_0$  and  $\gamma_0$ , since these determine at which frequency the MR peaks and how fast it damps. Changes in temperature of 0.2°C (at constant bias current) or changes in bias current of 1mA (at constant temperature), corresponding to a wavelength shift of  $\sim 0.2$  , did not significantly affect the filter performance.

Figure 23 and Figure 24 show the RIN and MR for bias currents 50mA and 110mA, respectively, at the laser output and after reflection from the grating. In both cases, reductions in RIN were achieved. The dotted line indicates the shot noise level. At high bias currents the RIN goes below the shot noise, and it becomes hard to measure. The MR in Figure 23 is flattened by the effect of the grating, whereas in Figure 24 an enhancement and increase in bandwidth is achieved.

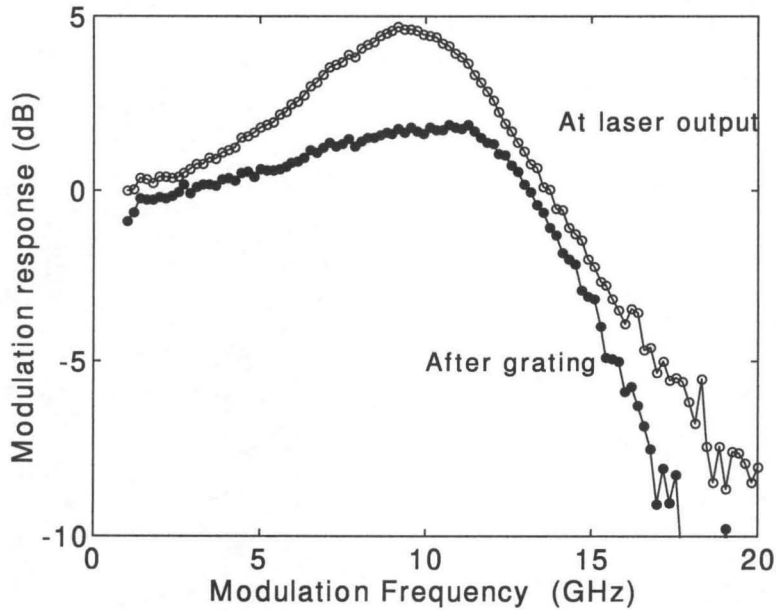
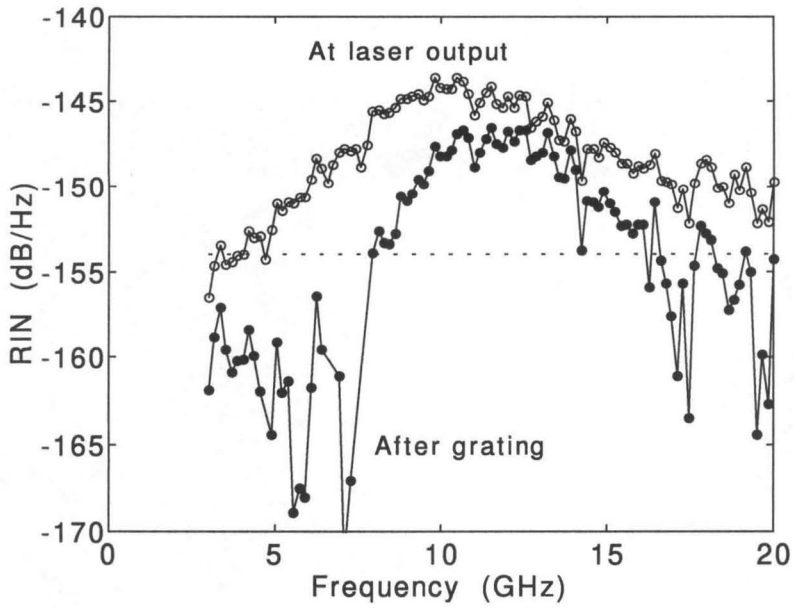


Figure 23: Laser RIN and modulation response at 50mA bias current.

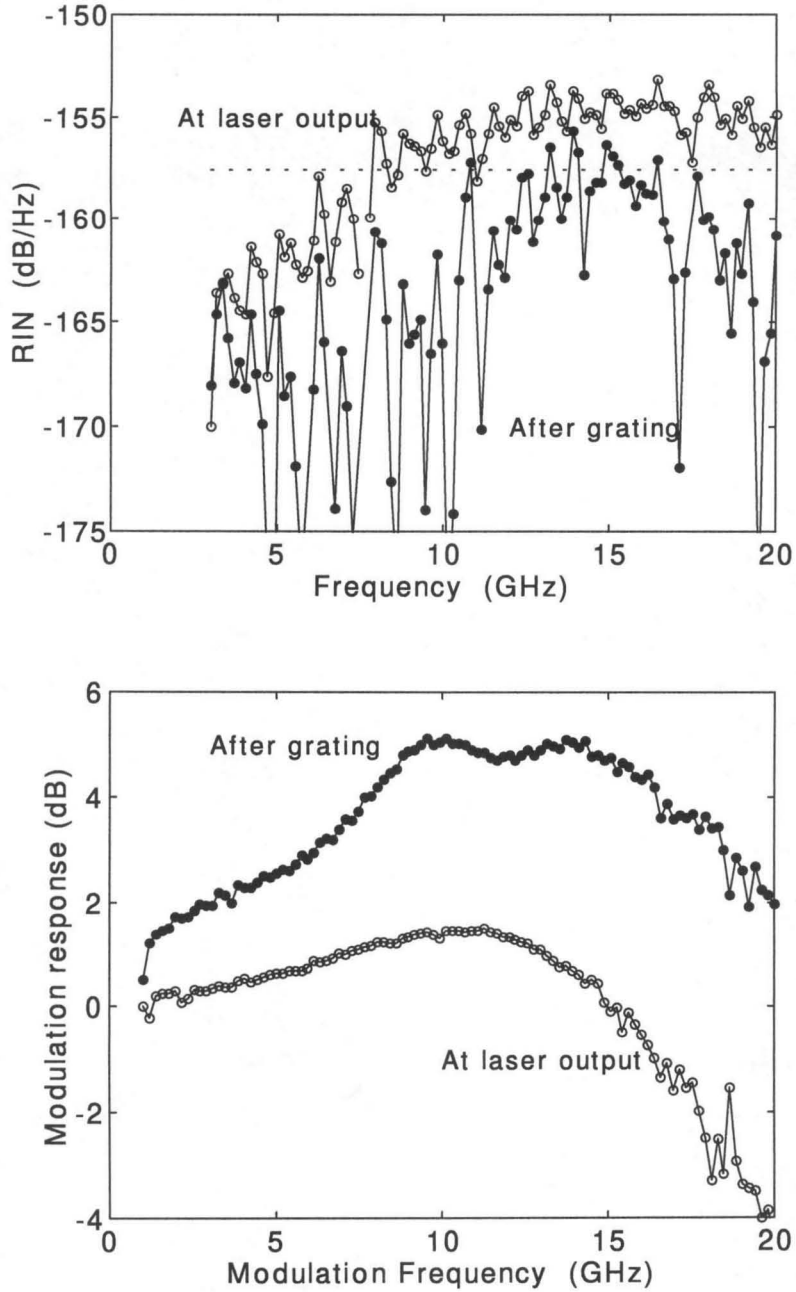


Figure 24: Laser RIN and modulation response at 110mA bias current.

## Appendix III.1 COMPARISON OF MODULATION RESPONSE AND INTERFEROMETER TECHNIQUES FOR DETERMINATION OF LASER CHIRP.

In this appendix, the experimental technique developed in section III.1.3.B to measure  $\kappa(\Omega)$  will be contrasted with an interferometer technique.

The power spectrum of the optical field was measured by a scanning Fabry-Perot for a wide range of modulation powers, and the IM index was determined using an electrical spectrum analyzer. As a first approximation, the microwave power can be adjusted so as to obtain known FM indices. For example, the amplitude of the carrier frequency is approximately zero for an FM index  $m_{FM} = 2.4$  [9]. However, the presence of IM complicates the expressions for the power in each of the side bands and this method could not be used. Here,  $\frac{m_{FM}}{m_{IM}}$  and  $\Delta\phi$  were obtained by fitting the power in the main and first side bands as a function of  $m_{IM}$ . From them, the real and imaginary parts of  $\kappa(\Omega)$  were derived for a given  $\alpha$ .

In Figure 25, the results from the interferometer technique and the modulation response technique have been plotted for comparison. The interferometer technique is noisier, especially at high frequencies, because the microwave source and amplifier that was used could only yield a maximum IM index of 0.25. Nevertheless, the same frequency dependence and order of magnitude is observed. Note that in the simple laser chirp model, the real part of  $\kappa(\Omega)$  would be a constant independent of  $\Omega$  and the imaginary part would be zero.

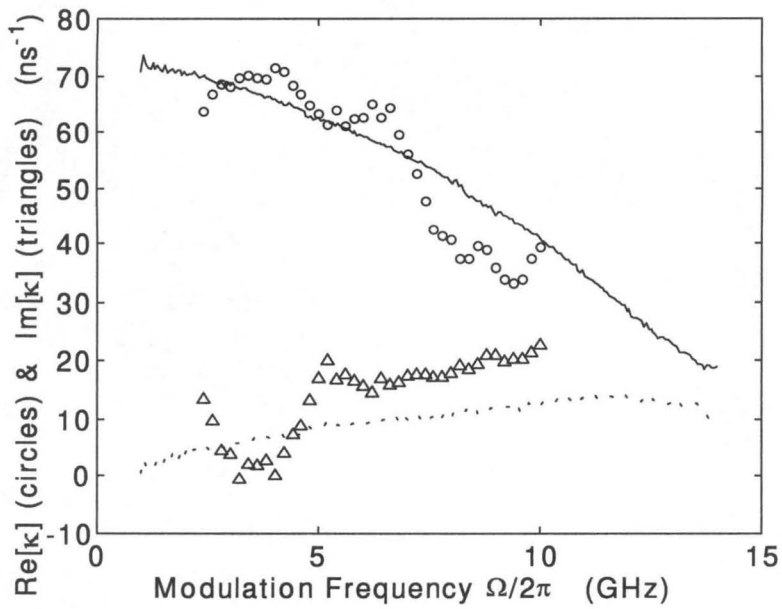


Figure 25: Real and imaginary part of  $\kappa(\Omega)$  obtained from modulation response (solid and dotted, respectively) and from optical spectrum side bands (circles and triangles, respectively).



## REFERENCES

- [1] L. Bjerkan, A. Royset, L. Hafskjaer, D. Myhre, "Measurement of laser parameters for simulation of high-speed fiberoptic systems," *J. Lightwave Technol.*, vol. 14, 2, pp. 839-850, May, 1996.
- [2] J. C. Cartledge, R. C. Srinivasan, "Extraction of DFB laser rate equation parameters for system simulation purposes," *J. Lightwave Technol.*, vol. 15, 5, pp. 852-860, May, 1997.
- [3] B. Wedding, "Analysis of fiber transfer function and determination of receiver frequency response for dispersion supported transmission," *Electron. Lett.*, vol. 30, 1, pp. 58-59, Jan., 1994.
- [4] A. Royset, L. Bjerkan, D. Myhre, L. Hafskjaer, "Use of dispersive optical fiber for characterisation of chirp in semiconductor lasers," *Electron. Lett.*, vol. 30, 9, pp. 710-712, Apr., 1994.
- [5] R. C. Srinivasan, J. C. Cartledge, "On using fiber transfer functions to characterize laser chirp and fiber dispersion," *IEEE Photon. Tech. Lett.*, vol. 7, 11, pp. 1327-1329, Nov., 1995.
- [6] T. L. Koch, R. A. Linke, "Effect of nonlinear gain reduction on semiconductor laser wavelength chirping," *Appl. Phys. Lett.*, vol. 48, 10, pp. 613-615, Mar., 1986.
- [7] E. Peral, W. K. Marshall, A. Yariv, "Precise measurement of semiconductor laser chirp using effect of propagation in dispersive fiber and application to simulation of transmission through fiber gratings," *J. Lightwave Technol.*, vol. 16, 10, pp. 1874-1880, Oct., 1998.
- [8] J. Kinoshita, K. Matsumoto, "Transient chirping in distributed feedback lasers: effect of spatial hole burning along the laser axis," *IEEE J. Quantum Electron.*, vol. 24, 11, pp. 2160-2169, Nov., 1988.
- [9] P. Vankwikelberge, F. Buytaert, A. Franchois, R. Baets, P. I. Kuinderma, C. W. Fredriksz, "Analysis of the carrier-induced FM response of DFB lasers: theoretical

- and experimental case studies," *IEEE J. Quantum Electron.*, vol. 25, 11, pp. 2239-2253, Nov., 1989.
- [10] R. F. S. Ribeiro, J. R. F. da Rocha, A. V. T. Cartaxo, H. J. A. da Silva, B. Franz, B. Wedding, "FM response of quantum-well lasers taking into account carrier transport effects," *IEEE Photon. Tech. Lett.*, vol. 7, 8, pp. 857-859, Aug., 1995.
- [11] C. Y. Tsai, F. P. Shih, T. L. Sung, T. Y. Wu, C. H. Chen, C. Y. Tsai, "A small signal analysis of the modulation response of high-speed quantum well lasers: effects of spectral hole burning, carrier heating, and carrier diffusion-capture-escape," *IEEE J. Quantum Electron.*, vol. 33, 11, pp. 2084-2096, Nov., 1997.
- [12] M. McAdams, E. Peral, D. Provenzano, W. K. Marshall, A. Yariv, "Improved laser modulation response by frequency modulation to amplitude modulation conversion in transmission through a fiber grating," *Appl. Phys. Lett.*, vol. 71, 7, pp. 879-881, Aug., 1997.
- [13] M. McAdams, D. Provenzano, E. Peral, W. K. Marshall, A. Yariv, "Effect of transmission through fiber gratings on semiconductor laser intensity noise," *Appl. Phys. Lett.*, vol. 23, 8, pp. 3341-3343, Dec., 1997.
- [14] J. Kinoshita, "Modeling of high-speed DFB lasers considering the spatial hole burning effect using three equations," *IEEE J. Quantum Electron.*, vol. 30, 4, pp. 929-938, Apr., 1994.
- [15] W. Huang, X. Li, T. Makino, "Analytical formulas for modulation responses of semiconductor DFB lasers," *IEEE J. Quantum Electron.*, vol. 31, 5, pp. 842-851, May, 1995.
- [16] G. Morthier, "An accurate rate-equation description for DFB lasers and some interesting solutions," *IEEE J. Quantum Electron.*, vol. 33, 2, pp. 231-237, Feb., 1997.
- [17] P. Vankwikelberge, G. Morthier, R. Baets, "CLADISS - A longitudinal multimode model for the analysis of the static, dynamic, and stochastic behavior of diode lasers with distributed feedback," *IEEE J. Quantum Electron.*, vol. 26, 10, pp. 1728-1741, Oct., 1990.

- [18] R. Schatz, "Dynamics of spatial hole burning effects in DFB lasers," *IEEE J. Quantum Electron.*, vol. 31, 11, pp. 1981-1993, Nov., 1995.
- [19] G. P. Agrawal, A. H. Bobeck, "Modeling of distributed feedback semiconductor lasers with axially-varying parameters," *IEEE J. Quantum Electron.*, vol. 24, 12, pp. 2407-2414, Dec., 1988.
- [20] B. Tromborg, H. E. Lassen, H. Olesen, "Traveling wave analysis of semiconductor lasers: modulation responses, mode stability and quantum mechanical treatment of noise spectra," *IEEE J. Quantum Electron.*, vol. 30, 4, pp. 939-956, Apr., 1994.
- [21] L. Olofsson, T. G. Brown, "Frequency dependence of the chirp factor in 1.55  $\mu\text{m}$  distributed feedback semiconductor laser," *IEEE Photon. Technol. Lett.*, vol. 4, 7, pp. 688-691, Jul., 1991.
- [22] H. Kogelnik, C. V. Shank, "Coupled-wave theory of distributed feedback lasers," *J. Appl. Phys.*, vol. 43, 5, pp. 2327-2355, May, 1972.
- [23] H. Ghafouri-Shiraz, B. S. K. Lo, *Distributed feedback laser diodes: principles and physical modelling*, John Wiley & Sons, Chichester, 1996.
- [24] C. H. Henry, "Theory of linewidth of semiconductor lasers," *IEEE J. Quantum Electron.*, vol. 18, 2, pp. 259-264, Feb., 1982.
- [25] C. H. Henry, "Phase noise in semiconductor lasers," *J. Lightwave Technol.*, vol. 4, 3, pp. 298-311, Mar., 1986.
- [26] C. H. Henry, "Theory of the phase noise and power spectrum of a single mode injection laser," *IEEE J. Quantum Electron.*, vol. 19, 9, pp. 1391-1397, Sep., 1983.
- [27] B. W. Hakki, T. L. Paoli, "Gain spectra in GaAs double-heterostructure injection lasers," *J. Appl. Phys.*, vol. 46, 3, pp. 1299-1306, Mar., 1975.
- [28] C. H. Henry, R. A. Logan, F. R. Merritt, "Measurements of gain and absorption spectra in AlGaAs buried heterostructure lasers," *J. Appl. Phys.*, vol. 51, 6, pp. 3042-3050, Jun., 1980.
- [29] A. H. Henry, R. A. Logan, K. A. Bertness, "Measurement of spectrum, bias dependence, and intensity of spontaneous emission in GaAs lasers," *J. Appl. Phys.*, vol. 52, 7, pp. 4453-4456, Jul., 1981.

- [30] C. H. Henry, R. A. Logan, H. Temkin, F. R. Merritt, "Absorption, emission, and gain spectra of 1.3 $\mu$ m InGaAsP quaternary lasers," *IEEE J. Quantum Electron.*, vol. 19, 6, pp. 941-946, Jun., 1983.
- [31] F. Girardin, G. H. Duan, "Characterization of semiconductor lasers by spontaneous emission measurements," *IEEE J. Sel. Top. Quantum Electron.*, vol. 3, 2, pp. 461-470, Apr., 1997.
- [32] R. Schatz, E. Berglind, L. Gillner, "Parameter extraction from DFB lasers by means of a simple expression for the spontaneous emission spectrum," *IEEE Photon. Tech. Lett.*, vol. 6, 10, pp. 1182-1184, Oct., 1994.
- [33] W. Fang, A. Hsu, S. L. Chuang, T. Tanbun-E, A. M. Sergent, "Measurement and modeling of distributed-feedback lasers with spatial hole burning," *IEEE J. of Sel. Top. Quantum Electron.*, vol. 3, 2, pp. 547-554, Apr., 1997.
- [34] J. Skagerlund, F. Pusa, O. Sahlen, *et al.*, "Evaluation of an automatic method to extract the grating coupling coefficient in different types of fabricated DFB lasers," *IEEE J. Quantum Electron.*, vol. 34, 1, pp. 141-146, Jan., 1998.
- [35] P. A. Morton, T. Tanbun-Ek, R. A. Logan, A. M. Sergent, P. F. Sciortino, Jr., D. L. Coblenz, "Frequency response subtraction for simple measurement of intrinsic laser dynamic properties," *IEEE Photon. Tech. Lett.*, vol. 4, 2, pp. 133-135, Feb., 1992.
- [36] R. S. Tucker, "High-speed modulation of semiconductor lasers," *J. Lightwave Technol.*, vol. 3, 6, pp. 1180-1192, Dec., 1985.
- [37] R. Olshansky, P. Hill, V. Lanzisera and W. Powazinik, "Frequency response of 1.3 $\mu$ m InGaAsP high speed semiconductor lasers," *IEEE J. Quantum Electron.*, vol. 23, 9, pp. 1410-1418, Sep., 1987.
- [38] G. P. Agrawal, N. K. Dutta, *Long-Wavelength Semiconductor Lasers*, Van Nostrand Reinhold Company, New York, 1986.
- [39] C. H. Henry, "Theory of spontaneous emission noise in open resonators and its application to lasers and optical amplifiers," *J. Lightwave Technol.*, vol. 4, 3, pp. 298-311, Mar., 1986.

- [40] T. Makino, "Transfer matrix formulation of spontaneous emission noise of DFB semiconductor lasers," *J. Lightwave Technol.*, vol. 9, 1, pp. 84-91, Jan., 1991.
- [41] K. J. Vahala, C. E. Zah, "Effect of doping on the optical gain and the spontaneous noise enhancement factor in quantum well amplifiers and lasers studied by simple analytical expressions," *Appl. Phys. Lett.*, vol. 52, 23, pp. 1945-1947, Jun., 1988.
- [42] T. A. DeTemple, C. M. Herzinger, "On the semiconductor laser logarithmic gain-current density relation," *IEEE J. Quantum Electron.*, vol. 29, 5, pp. 1246-1252, May, 1993.
- [43] W. Rideout, W. F. Sharfin, E. S. Koteles, M. O. Vassell, B. Elman, "Well-barrier hole burning in quantum well lasers," *IEEE Photon. Tech. Lett.*, vol. 3, 9, pp. 784-786, Sep., 1991.
- [44] K. Lau, "Dynamics of quantum well lasers" in *Quantum Well Lasers*, edited by Zory, San Diego, Academic Press, 1993
- [45] S. C. Kan, D. Vassilovski, T. C. Wu, K. Y. Lau, "On the effects of carrier diffusion and quantum capture in high-speed modulation of quantum-well lasers," *Appl. Phys. Lett.*, vol. 61, 7, pp. 752-754, Aug., 1992.
- [46] S. C. Kan, D. Vassilovski, T. C. Wu, K. Y. Lau, "Quantum capture and escape in quantum well lasers - implications on direct modulation bandwidth limitations," *IEEE Photon. Tech. Lett.*, vol. 4, 5, pp. 428-430, May, 1992.
- [47] S. C. Kan, D. Vassilovski, T. C. Wu, K. Y. Lau, "Quantum capture limited modulation bandwidth of quantum well-wire and dot lasers," *Appl. Phys. Lett.*, vol. 62, 19, pp. 2307-2309, May, 1993.
- [48] R. Nagarajan, T. Fukushima, S. W. Corzine, J. E. Bowers, "Effects of carrier transport on high-speed quantum well lasers," *Appl. Phys. Lett.*, vol. 59, 15, pp. 1835-1837, Oct., 1991.
- [49] S. C. Kan, K. Y. Lau, "Intrinsic equivalent circuit of quantum well lasers," *IEEE Photon. Tech. Lett.*, vol. 4, 6, pp. 528-530, Jun., 1992.

- [50] R. Nagarajan, M. Ishikawa, T. Fukushima, R. S. Geels, J. E. Bowers, "High speed quantum-well lasers and carrier transport effects," *IEEE J. Quantum Electron.*, vol. 28, 10, pp. 1990-2007, Oct., 1992.
- [51] R. Nagarajan, J. E. Bowers, "Effect of carrier transport on injection efficiency and wavelength chirping in quantum well lasers," *IEEE J. Quantum Electron.*, vol. 29, 6, pp. 1601-1608, Jun., 1993.
- [52] G. P. Agrawal, "Spectral hole burning and gain saturation in semiconductor lasers: strong-signal theory," *J. Appl. Phys.*, vol. 63, pp. 1232-1234, 1988.
- [53] G. P. Agrawal, "Gain nonlinearities in semiconductor lasers: theory and application to distributed feedback lasers," *IEEE J. Quantum Electron.*, vol. 23, 6, pp. 860-868, Jun., 1987.
- [54] G. P. Agrawal, "Effect of gain nonlinearities on the dynamic response of single-mode semiconductor lasers," *IEEE Photon. Tech. Lett.*, vol. 1, 12, pp. 419-421, Dec., 1989.
- [55] A. Yariv, *Optical electronics in modern communications*, Oxford University Press, New York, 1997.
- [56] T. Okoshi, K. Kikuchi, A. Nakayama, "Novel method for high resolution measurements of laser output spectrum," *Electron. Lett.*, vol. 16, pp. 630-631, 1980.
- [57] L. B. Mercer, "1/f frequency noise effects on self-heterodyne linewidth measurements," *J. Lightwave Technol.*, vol. 9, 4, pp. 485-493, Apr., 1991.
- [58] E. Peral, W. K. Marshall, D. Provenzano, A. Yariv, "Effect of many weak side modes on relative intensity noise of distributed feedback semiconductor lasers," *Appl. Phys. Lett.*, vol. 72, 8, pp. 888-890, Feb., 1998.
- [59] Bennett, Soref, Alamo, "Carrier induced change in refractive index of InP, GaAs, and InAsAsP," *J. Quantum Electron.* 26, 1, pp. 113-122, Jan. 1990.
- [60] J. Wang, U. A. Griesinger, F. Stolz, H. C. Schweizer, "Carrier capture times in quantum-well, -wire, and -box distributed feedback lasers characterized by dynamic lasing emission measurements," *IEEE J. Sel. Top. QE*, vol. 3, 2, pp. 223-229, Apr., 1997.

- [61] W. K. Marshall, J. Paslaski, A. Yariv, "Reduction of relative intensity noise of the output field of semiconductor lasers due to propagation in dispersive optical fiber," *Appl. Phys. Lett.*, vol. 68, 18, pp. 2496-2498, Apr., 1996.
- [62] R. A. Linke, B. L. Kasper, C. A. Burrus, I. P. Kaminow, J. S. Ko, T. P. Lee, "Mode power partition events in nearly single frequency lasers," *J. Lightwave Technol.*, vol. 3, 3, pp. 706-711, Jun., 1985.
- [63] R. H. Wentworth, G. E. Bodeep, T. E. Darcie, "Laser mode partition noise in lightwave systems using dispersive optical fiber," *J. Lightwave Technol.*, vol. 10, 1, pp. 84-87, Jan., 1992.
- [64] K. Petermann, *Laser modulation and noise*, (Boston, Kluwer, 1991).
- [65] C. B. Su, J. Schlafer, R. B. Lauer, "Explanation of low frequency relative intensity noise in semiconductor lasers," *Appl. Phys. Lett.*, vol. 57, 9, pp. 849-851, Aug., 1990.
- [66] X. Lu, C. B. Su, R. B. Lauer, G. J. Meslener, L. W. Ulbricht, "Analysis of relative intensity noise in semiconductor lasers and its effect on subcarrier multiplexed lightwave systems," *J. Lightwave Technol.*, vol. 12, 7, pp. 1159-1166, Jul., 1992.
- [67] K. Kikuchi, "Effect of  $1/f$  type FM noise on semiconductor laser linewidth residual in high power limit," *IEEE J. Quantum Electron.*, vol. 25, pp. 684-688, 1989.
- [68] G. P. Agrawal, R. Roy, "Effect on injection-current fluctuations on the spectral linewidth of semiconductor lasers," *Phys. Rev. A*, vol. 37, 7, pp. 2495-2501, Apr., 1988.
- [69] E. Peral, J. Capmany, J. Martí, "Iterative solution to the Gel'fand-Levitan-Marchenko equations and applications to synthesis of fiber gratings," *IEEE Quantum. Electron.*, vol. 32, 12, pp. 2078-2084, Dec., 1996.
- [70] A. Asseh, H. Storoy, B. Sahlgren, S. Sandgren, R. Stubbe, "A writing technique for long fiber Bragg gratings with complex reflectivity profiles," *J. Lightwave Technol.*, vol. 15, 8, pp. 1419-1423, Aug., 1997.





## Chapter IV.

# Nonlinear fiber propagation: effect of stimulated Brillouin scattering

**A**s the launched power into the fiber is raised, the fiber response departs increasingly from the linear behavior that was described in the two previous chapters. Among the nonlinear phenomena that can arise, self-phase modulation (SPM), four-wave mixing (FWM), stimulated Raman scattering (SRS) and stimulated Brillouin scattering (SBS) are the most important ones for optical communications systems [1]. Fiber nonlinearities may significantly degrade the performance of high-speed lightwave systems using high-power laser sources [2].

Stimulated Brillouin scattering (SBS) arises as the result of a nonlinear interaction between photons and acoustic phonons. As a consequence, part of the power in the forward propagating field is lost to a backward propagating optical field, that is downshifted from the forward propagating wave by the acoustic frequency. It has been shown through signal-to-noise ratio and bit-error rate measurements that the onset of SBS can be a major impairment in directly-modulated fiber-optic systems [3],[4].

Previous studies emphasized degradations resulting from power saturation [5], spontaneous Brillouin scattering noise [6], and the effect of the backward-propagating

signal on the laser source [2]. In this chapter it will be shown that, in addition, SBS can induce a phase shift of the optical carrier relative to its sidebands. This phase shift can lead to severe distortion of the modulation response (MR) and increase in relative intensity noise (RIN) at low frequencies due to conversion of laser frequency modulation (FM), i.e., laser chirp, to intensity modulation (IM).

In an optical fiber, the acoustooptic interaction between sound and optical waves differs from the Brillouin scattering in a bulk medium [7]. In a fiber, a large number of (longitudinal) acoustic modes are excited by the light, which are the eigenmodes of the cylindrical structure rather than plane waves, and this leads to a relaxation of the wave-vector selection rule. As a consequence, spontaneous Brillouin scattering in the forward direction was observed, and was called guided acoustic wave Brillouin scattering [7]. It has been recently found that this effect can contribute to timing jitter in soliton transmission systems [8] and affect propagation of NRZ pulse trains [9].

Here it will be demonstrated that the guided nature of the acoustic waves in optical fibers can also affect backward stimulated Brillouin scattering, inducing a phase shift of the optical waves. In order that significant acoustooptic interaction occur, not only the propagation constants have to be phase matched, but also there has to be significant overlap between the transverse profiles of acoustic and optical modes. The latter condition is satisfied for modes with phase velocity close to but greater than the longitudinal sound velocity,  $v_l$ . However, if the phase velocity is less than  $v_l$ , the acoustic mode becomes a surface wave with maximum amplitude near the surface of the cylinder, and will be hardly excited by the optical wave. It will be shown that this results in a slight asymmetry in the Brillouin gain spectrum, which can be observed in precise measurements of Brillouin gain spectra (see, e.g., Figure 4a in [10]), and a phase shift of the optical waves affected by SBS, in agreement with our experimental results. If most of the optical power is contained in the carrier and the modulation frequency is larger than the Brillouin gain bandwidth, only the carrier undergoes SBS, and thus suffers an additional phase shift relative to its sidebands. As a consequence, conversion of

frequency modulation to intensity modulation occurs, which is experimentally observed in measurements of modulation response and relative intensity noise.

Section IV.1 contains a theory of the acoustooptic interaction including the waveguiding effect of the optical fiber on the acoustic wave. It is shown that SBS induces a phase shift of the optical carrier relative to its sidebands. In section IV.2, experimental evidence is given that SBS induces a phase change in the optical carrier with respect to the sidebands that leads to an increase of the MR at low frequencies due to FM-to-IM conversion. Section IV.3 presents the effect of SBS on RIN. The SBS induced phase change causes an increase in RIN at low frequencies by conversion of phase noise to intensity noise. In addition, it is shown that SBS causes excess noise at frequencies around harmonics of the acoustic wave frequency for both forward and backward propagating waves.

## **IV.1 SCALAR THEORY OF THE ACOUSTOOPTIC INTERACTION IN OPTICAL FIBER.**

In an optical fiber, thermally generated acoustic field phonons initiate the process of SBS by providing the seed grating for the generation by Bragg reflection of a backward propagating field. This backward propagating field interacts with the forward propagating wave or pump wave to generate an acoustic wave through the phenomenon of electrostriction. This acoustic wave adds up to the initial field to backreflect more strongly, thus starting the stimulated process (see Figure 1). Conservation of both momentum and energy of the participating photons and phonons leads to a condition on the frequency of the backward propagating wave, and for silica fiber gives roughly 11GHz [1].

### IV.1.1 Acoustic wave equation.

The acoustic field variables that characterize particle motion and deformation in a vibrating material medium are the particle displacement vector,  $\mathbf{u}(\mathbf{r},t)$ , the strain tensor,  $\sigma(\mathbf{r},t)$ , and the accompanying elastic stress tensor,  $\tau(\mathbf{r},t)$ . The vector equations that describe these variables can be solved to yield the acoustic modes and from them the gain of the stimulated process can be found. This vector approach, which is more fully developed in Appendix IV.1, is quite involved, but can be greatly simplified by neglecting transverse variations of the material displacement and the electric field. This is a valid approximation for the case here considered of backward Brillouin scattering in a single mode optical fiber. In this case, the equation of motion can be expressed in terms of the material density variation,  $\rho$ , which, in analogy with hydrodynamics, is defined as:

$$\rho = -\rho_0 \nabla \cdot \mathbf{u} \quad (1)$$

where  $\rho_0$  is the material density.

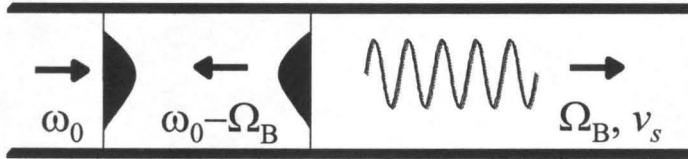


**Figure 1: Generation of an acoustic wave with frequency  $\Omega_B$  traveling at the speed of sound,  $v_s$ , and a backward propagating optical wave, downshifted by  $\Omega_B$  from the incident wave by the process of stimulated Brillouin scattering.**

The material density fluctuation,  $\rho$ , satisfies the wave equation driven through electrostriction by the electric field,  $\mathbf{E}$ , as follows (see Appendix IV.1):

$$\frac{\partial^2 \rho}{\partial t^2} = v_i^2 \left( 1 + \Gamma_s \frac{\partial}{\partial t} \right) \nabla^2 \rho - \frac{\gamma}{2} \nabla^2 E^2 \quad (2)$$

where  $v_l$  is the longitudinal sound velocity,  $\Gamma_s$  is the damping factor and  $\gamma$  quantifies the strength of the electrostrictive effect.

In the absence of electric field, only a discrete set of acoustic modes,  $\rho_n(r, \varphi)$ , can propagate in the fiber. From equation (2), assuming a harmonically varying acoustic wave at sound angular frequency  $\Omega_s$ , and neglecting the damping factor, these modes satisfy the wave equation:

$$\left(\frac{i\Omega_s}{v_l}\right)^2 \rho_n = [\nabla_t^2 + k_n^2] \rho_n \quad (3)$$

Here, the operator  $\nabla_t^2$  is the Laplacian acting on the transverse coordinates, and  $k_n$  are the eigenvalues or longitudinal propagation constants of the acoustic modes.

Only acoustic modes with no azimuthal variation will excite a polarization in a single mode fiber. These are usually referred to as dilatational or longitudinal acoustic modes [20]-[21] and have a radial dependence of the form:

$$\rho_n(r) = \frac{1}{(\pi a_{cl}^2)^{1/2}} \frac{J_0(k_{ln} r)}{(J_0^2(k_{ln} a_{cl}) + J_1^2(k_{ln} a_{cl}))^{1/2}} \quad (4)$$

where  $a_{cl}$  is the radius of the acoustic guide, which is usually the fiber cladding radius, and the eigenfunctions are normalized such that  $\langle \rho_n, \rho_n \rangle = 1$  (see Appendix IV.2). The value of the transverse propagation constant of the longitudinal acoustic modes,  $k_{ln}$ , follows from application of boundary conditions. If the cylindrical surface is assumed to be free of traction, i.e.,  $\tau \cdot \mathbf{n} = 0$ , the Pochhammer frequency equation [21] is derived,

from which  $k_n$  and  $k_{ln} = \sqrt{\left(\frac{\Omega_s}{v_l}\right)^2 - k_n^2}$  can be calculated. When the particle vibrates in

a longitudinal mode, radial and axial motions are coupled, and, contrary to what has been previously stated [8]-[9], the eigenfunctions (4), even though they form a complete set, are *not* orthogonal.

### IV.1.2 Acoustooptic interaction.

The acoustic wave originates a nonlinear polarization,  $\mathbf{P}^{NL}$ , given by:

$$\mathbf{P}^{NL} = \frac{\gamma}{\rho_0} \rho \mathbf{E} \quad (5)$$

Let us assume harmonically varying forward and backward propagating optical waves, that is:

$$\mathbf{E}(r, z, t) = \frac{1}{\sqrt{2}} \left[ a_1(z, t) e^{i(\omega_1 t - \beta_1 z)} \hat{\mathbf{e}}_1 + a_2(z, t) e^{i(\omega_2 t - \beta_2 z)} \hat{\mathbf{e}}_2 \right] E_0(r) + c.c. \quad (6)$$

where  $E_0(r)$  is the transverse distribution of the fundamental mode in single mode optical fiber, and  $\hat{\mathbf{e}}_1$  and  $\hat{\mathbf{e}}_2$  are unit vectors in the directions of the forward and backward propagating fields, respectively. Here we neglect fiber birefringence (see Appendix IV.1 for a discussion on birefringence induced by the acoustic wave), and assume linearly polarized electric fields, both along the same direction. The beating of these two fields gives rises to an acoustic wave at frequency  $\Omega_s = \omega_1 - \omega_2$  and with wavevector  $k_s = \beta_1 + \beta_2 \approx \frac{4\pi n_0}{\lambda_0}$ , where  $\lambda_0$  is the optical wavelength and  $n_0$  is the fiber modal index. Since the radius of the acoustic guide,  $a_{cl}$ , is much larger than the acoustic wavelength,  $\sim \frac{\lambda_0}{2n_0}$ , a large number of acoustic modes are excited. The acoustic modes form a complete set and therefore the acoustic wave can be expressed as a linear combination of the  $\rho_n(r, \varphi)$  such as:

$$\rho(r, \varphi, z, t) = a_1(z, t) a_2^*(z, t) \sum_n b_n(z, t) \rho_n(r, \varphi) e^{i(\Omega_s t - k_s z)} + c.c. \quad (7)$$

Inserting the expansion for the acoustic wave (7) into the density wave equation (2), and using (3) the coefficients  $b_n(z, t)$  can be obtained in a "least-squared" sense by solving the following system of linear differential equations:

$$\begin{aligned} \sum_n \left[ \left\{ v_l^2 (1 + i\Omega_s \Gamma_s) \left( k_n^2 - k_s^2 - 2ik_s \frac{\partial}{\partial z} \right) - i\Omega_s^3 \Gamma_s \right\} - 2i\Omega_s \frac{\partial}{\partial t} \right] b_n \langle \rho_n, \rho_m \rangle = \\ = -\frac{\gamma}{2} k_s^2 \langle E_0^2, \rho_m \rangle \end{aligned} \quad (8)$$

In writing (8) we have neglected derivatives of the electric field envelope amplitudes,  $a_1$  and  $a_2$ , second derivatives of the  $b_n$  and transverse derivatives of the electric field against longitudinal derivatives, and we have assume that the modulation frequency of the acoustic wave envelope is much smaller than  $\Omega_s$ . Analytical expressions for the inner products in (8) have been found and are included in Appendix IV.2 (these integrals appeared in a similar context in [8],[9] and were evaluated numerically). In practice, only modes with  $k_n \approx k_s$  will contribute significantly to the mode expansion (7), and only a reduced number of coefficients  $b_n$  is needed to perfectly describe the acoustic wave.

The evolution of the electric field envelope amplitudes can be found by substituting the electric field expansion (6) and the nonlinear polarization (5) into the optical wave equation. We obtain

$$\frac{\partial a_1}{\partial z} + v_g \frac{\partial a_1}{\partial t} + \frac{i}{2} \beta'' \frac{\partial^2 a_1}{\partial t^2} = \frac{\alpha_f}{2} a_1 - \frac{g_B}{2} |a_2|^2 a_1 \quad (9)$$

$$-\frac{\partial a_2}{\partial z} + v_g \frac{\partial a_2}{\partial t} + \frac{i}{2} \beta'' \frac{\partial^2 a_2}{\partial t^2} = \frac{\alpha_f}{2} a_2 + \frac{g_B^*}{2} |a_1|^2 a_2 \quad (10)$$

$$g_B = i \frac{\omega \gamma}{2 \rho_0} \sum_n b_n \langle \rho_n, E_0^2 \rangle \quad (11)$$

where  $\omega \cong \omega_1 \cong \omega_2$ ,  $\beta \cong \beta_1 \cong \beta_2$ ,  $v_g$  is the fiber group velocity,  $\beta''$  is the fiber dispersion parameter and  $\alpha_f$  is the fiber loss. The electric field is normalized to

$\langle E_0, E_0 \rangle = \frac{\omega \mu}{\beta}$  (see Appendix IV.2), so that the power in each optical field is given by

$$|a_i|^2.$$



From (9), the real part of  $g_B$  yields the Brillouin power gain, whereas the imaginary part of  $g_B$  is responsible for phase modulation of the optical field. In steady state, the pump wave undergoes a phase change,  $\Delta\phi_1$ , given by:

$$\Delta\phi_1(z) = -\frac{\text{Im}\{g_B\}}{2} \int_0^z |a_2|^2 dz \quad (12)$$

To a first approximation we can neglect spatial derivatives of  $b_n$  and can set  $\langle \rho_n, \rho_m \rangle \approx 0$  for  $n \neq m$ . In steady state the coefficients  $b_n$  are thus given by:

$$b_n \cong -\frac{\gamma}{2} \frac{k_s^2 \langle E_0^2, \rho_n \rangle}{v_l^2 (1 + i\Omega_s \Gamma_s) (k_n^2 - k_s^2) - i\Omega_s^3 \Gamma_s} \quad (13)$$

Under this approximation,  $g_B$  can be found as:

$$g_B = g_{B0} \sum_n \frac{e^{\frac{(k_{in} w)^2}{2}}}{\pi a_{cl}^2 [J_0^2(k_{in} a_{cl}) + J_1^2(k_{in} a_{cl})]} \frac{-i\Omega_B^3 \Delta\Omega}{(k_n^2 v_l^2 - \Omega_B^2) (\Omega_B^2 + i\Omega_s \Delta\Omega) - i\Omega_s^3 \Delta\Omega} \quad (14)$$

where  $\Omega_B = k_s v_l$ ,  $\Delta\Omega = \Gamma_s \Omega_B^2$  and  $g_{B0} = \frac{\mu \omega^2 k_s \gamma^2}{2\beta \rho_0 v_l \Delta\Omega} = \frac{4\pi^2 n_0^7 p_{12}^2}{c \rho_0 \lambda_0^2 v_l \Delta\Omega}$  are the approximate acoustic wave frequency, width and maximum gain of the Brillouin spectrum in the absence of waveguiding effects, i.e., for  $\Omega_B = k_s v_l \approx \Omega_s$ . A Gaussian approximation of the fundamental fiber mode was used, with beam mode waist  $w$  (see Appendix IV.2).

As stated above, the dispersion map for the acoustic modes, i.e., the variation of the longitudinal propagation constant of the acoustic modes,  $k_n$ , with the frequency,  $\Omega_s$ , can be obtained by solving the Pochhammer frequency equation [21]. Here only modes with real  $k_n$  are considered, since modes with imaginary  $k_n$  will attenuate very rapidly. On the contrary, the transverse propagation constants,  $k_{in}$ , can be either real or pure imaginary, depending on whether the phase velocity,  $\frac{\Omega_s}{k_n}$ , is greater or smaller than the longitudinal sound velocity,  $v_l$ . The latter case corresponds to surface waves, which have maximum amplitude near the surface of the cylinder. These surface waves



will hardly be excited, since the optical mode is concentrated near the core region. Similarly, when the magnitude of  $k_{ln}$  is large, the transverse profile of the acoustic mode becomes highly oscillatory and the overlap integral between the optical field and the acoustic mode is very small. Thus, only modes with  $k_n \approx k_s$  and  $\frac{\Omega_s}{k_n} \approx v_l$  will interact significantly with the optical field.

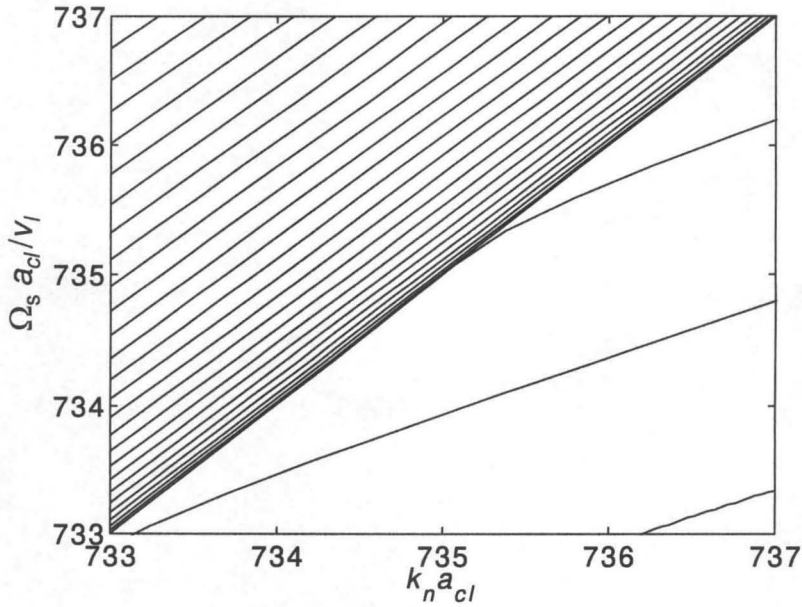


Figure 2: Dispersion map of longitudinal acoustic modes for  $v_l/v_t = 1.6032$ .

### IV.1.3 Numerical simulation.

Numerical calculations have been performed to obtain the Brillouin gain for standard single mode fiber with  $a_{cl}=62.5\mu\text{m}$  and at optical wavelength  $\lambda_0=1.55\mu\text{m}$ . The dispersion map in the region  $\Omega_s a_{cl}/v_l \approx k_s a_{cl} \approx 735$  is shown in Figure 2 for  $v_l/v_t = 1.6032$ . For  $\Omega_s/k_n \geq v_l$  the group velocity of the mode tends to the longitudinal sound velocity,  $v_l$ , from above, whereas when  $\Omega_s/k_n < v_l$  the mode becomes a surface

wave and the group velocity approaches the transverse sound velocity. The normalized overlap integral between the electric field and the acoustic modes,  $\frac{\beta}{\omega\mu} a_{cl} \langle E_0^2, \rho_n \rangle$ , is plotted in Figure 3 for several normalized frequencies. The asymmetry is due to the low overlapping between the optical mode and the surface waves.

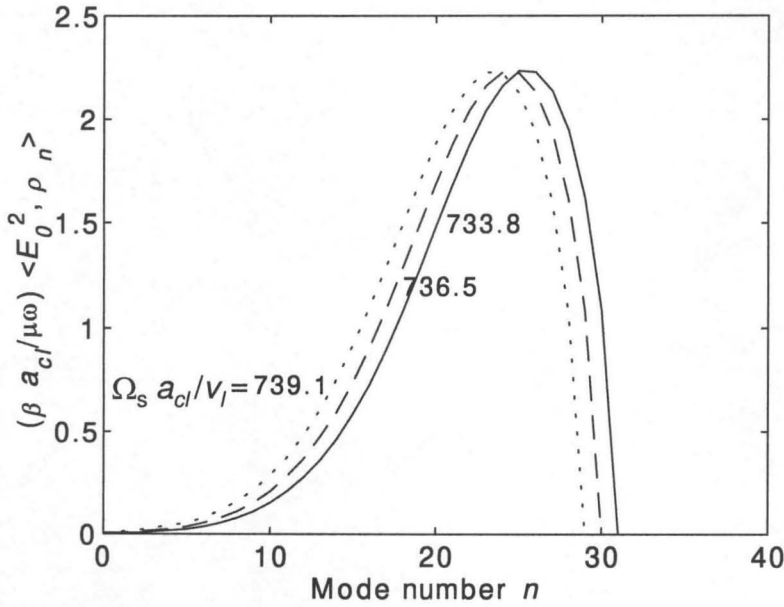


Figure 3: Normalized overlap integral between the optical and acoustic modes,

$\frac{\beta}{\omega\mu} a_{cl} \langle E_0^2, \rho_n \rangle$ , as a function of the (arbitrary) mode number,  $n$ , for

three different values of the normalized frequency,  $\Omega_s a_{cl} / v_l$ .

If the effect of waveguiding of the acoustic wave is ignored, the imaginary part of the Brillouin gain at the frequency at which the real part reaches its maximum value,  $\Omega_{s \max}$ , is given by:

$$\text{Im}\{g_B\}_{\max} = \text{Re}\{g_B\}_{\max} \frac{\Delta\Omega}{4\Omega_B} \quad (15)$$

Since  $\Delta\Omega \ll \Omega_B$ , this is very small. However, when the expression (11) is used, due to the low coupling to the surface waves, the  $\text{Re}\{g_B\}$  becomes slightly asymmetric, and  $\text{Im}\{g_B\}_{\max}$  is no longer negligible. Figure 4 shows the real and imaginary parts of  $\frac{g_B A_{\text{eff}}}{g_{B0}}$ , where  $A_{\text{eff}}$  is the fiber core effective area, for  $\Delta\Omega=15\text{MHz}$ . If waveguiding

effects are neglected,  $\frac{\text{Im}\{g_B\}}{\text{Re}\{g_B\}}_{\max} \approx 3 \times 10^{-4}$ , whereas here we obtain  $\frac{\text{Im}\{g_B\}}{\text{Re}\{g_B\}}_{\max} \approx 0.1$ .

The gain spectrum depends on fiber type [10], [15] and from the above discussion it is expected that the induced phase-shift will also exhibit a dependence.

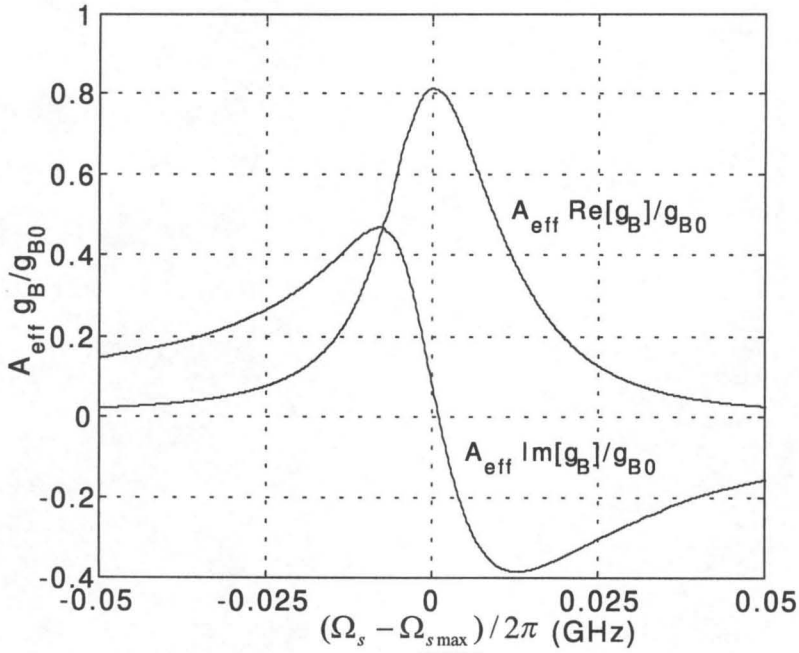


Figure 4: Real and imaginary part of the normalized gain,  $\frac{g_B A_{\text{eff}}}{g_{B0}}$ , for

$v_l/v_t = 1.6032$  as a function of deviation in frequency from that of maximum Brillouin gain,  $\Omega_{s\max}$ .

## IV.2 EFFECT OF SBS ON MODULATION RESPONSE

### IV.2.1 Theory

As discussed in the previous chapters, linear propagation in dispersive optical fiber produces a phase change of the sidebands relative to optical carrier due to group velocity dispersion, which results in partial conversion of FM into IM, which is photodetected at the fiber output [12],[13]. At low modulation frequencies the dispersion is very small and the change in modulation response (MR) after propagation is simply given by the fiber loss. However, our experimental results show that, as the optical power launched into the fiber increases, some optical power is backreflected by stimulated Brillouin scattering (SBS), and, correlated with this power loss, the MR at low frequencies is distorted. This distortion can be attributed to the phase change in the optical carrier induced by SBS. At high modulation frequency,  $\Omega$ , this small nonlinear phase change can be neglected compared to that resulting from dispersion. However, at low  $\Omega$  it becomes dominant and, as a consequence, the large adiabatic chirp that semiconductor lasers present at low  $\Omega$  is converted into intensity modulation.

#### IV.2.1.A Small-signal theory.

In this work, modulation frequencies  $\Omega/2\pi > 50\text{MHz}$  are considered. Since the spectrum of the Brillouin gain is very narrow ( $\sim 15\text{MHz}$ , as shown in section IV.3), it can be assumed that no cross-interactions between optical carrier and sidebands contribute to generation of Stokes waves. In addition, in the small-signal regime only two modulation sidebands need be taken into account. Since most of the optical power is contained in the carrier, the sidebands only suffer linear fiber loss and dispersion, whereas part of the power in the carrier is lost to SBS and undergoes an SBS-induced phase shift.

Let  $\theta(\Omega, z)$  be the dephasing between optical sideband at  $\Omega$  and the optical carrier due to both fiber dispersion and fiber nonlinearity, that is,

$$\theta(\Omega, z) = \theta_{disp}(\Omega, z) - \theta_{NL}(z) = -\frac{1}{2} \beta'' \Omega^2 z - \theta_{NL}(z) \quad (16)$$

where  $\theta_{NL}$  is the phase change that SBS induces in the optical carrier. Then, the detected photocurrent at a small-signal modulation frequency  $\Omega$  at the fiber output,  $I(\Omega, z)$ , is related to that that would be detected at the laser output,  $I(\Omega, 0)$ , by:

$$H(\Omega, z) \equiv [L_{DC}(z)L(\Omega, z)]^{1/2} \frac{I(\Omega, z)}{I(\Omega, 0)} = \cos\theta - 2 \sin\theta PIR(\Omega) \quad (17)$$

The electrical baseband transfer function  $H(\Omega, z)$  is normalized by the loss in the fiber, where  $L_{DC}(z)$  and  $L(\Omega, z)$  are the power loss suffered by the optical carrier and the sideband, respectively, due to both fiber attenuation and SBS. Since, as stated above, it is assumed that only the carrier undergoes SBS, then:

$$L(\Omega, z) = L_{Lin}(z) = e^{-\alpha_f z} \quad (18)$$

$$L_{DC} = L_{Lin} L_{NL} \quad (19)$$

#### IV.2.1.B Quasi-large-signal theory.

At higher modulation powers, but low enough so that  $m_{IM}$  is less than 2%, even though the small-signal theory would still be valid in the linear regime, it fails to predict the measured MR after propagation in fiber at high optical powers. As the modulation power is raised, the optical bandwidth increases due to a larger laser chirp, and the SBS is reduced. The consequence of this is twofold. First, since the FM index,  $m_{FM}$ , is a function of  $\Omega$ , the detected DC photocurrent fluctuates as  $\Omega$  is swept across. Second, the MR at sufficiently low  $\Omega$  and high modulation power returns to that of the linear regime.

Here a quasi-large-signal model is presented that explains the observed phenomena. As the laser chirp increases, the optical power is distributed among an increasing number of FM sidebands with weights  $c_n$  such as (see Chapter II):

$$\tilde{E} = P_0^{1/2} \sum_n c_n e^{in(\Omega t + \varphi_{IM})} \quad (20)$$

$$c_n(z=0) = e^{in\Delta\varphi} \left[ J_n(m_{FM}) + \frac{m_{IM}}{4} \left( J_{n+1}(m_{FM})e^{i\Delta\varphi} + J_{n-1}(m_{FM})e^{-i\Delta\varphi} \right) \right] \quad (21)$$

where  $J_n$  are Bessel functions and the fact was used that  $m_{IM}$  is small. Thus, after propagation in fiber, the coefficients  $c_n$  are given by:

$$c_n(z) = \sqrt{L(n\Omega, z)} e^{i\theta(n\Omega, z)} c_n(0) \quad (22)$$

The detected DC photocurrent,  $I_{DC}$ , can be obtained as:

$$I_{DC}(z) = R(0)P_0 \sum_n c_n(z)c_n^*(z) \quad (23)$$

where  $R(\Omega)$  is the photodiode responsivity, and the photocurrent at  $\Omega$  is given by:

$$I(\Omega, z) = R(\Omega)P_0 \sum_n c_{n+1}(z)c_n^*(z) \quad (24)$$

For intermediate values of  $m_{FM}$ , the power in some of the sidebands can be quite large, and even greater than the power in the carrier, thus undergoing SBS. For very large  $m_{FM}$ , the power is distributed in so many sidebands, that none of them carries enough power to experience significant SBS.

## IV.2.2 Experiment.

### IV.2.2.A Experimental set-up.

The diagram of the experimental set-up is shown in Figure 5. The optical source was a high-power MQW-DFB laser operating at  $1.55\mu\text{m}$ . This laser was biased at 300mA, yielding an output power at the laser pigtail of 14.4dBm, and had a threshold of 18mA. The laser was directly modulated with the signal from a network analyzer (NA) using a microwave probe. The laser light was attenuated and launched into an 85/15% fiber directional coupler. The 85% port was connected onto a spool of standard telecommunications fiber (from 25 to 75 km), the output signal was photodetected and then the MR was measured with the NA as described in Chapter II. The power spectra

of the forward and backward waves were measured using an ESA. Angled connectors were used to minimize reflections.

Measurements of MR and RIN before and after propagation in dispersive fiber, with the signal output attenuated to avoid nonlinear effects, were used to determine laser parameters [11],[12], such as  $PIR(\Omega)$ , resonance frequency  $\Omega_0=14\text{GHz}$ , damping factor  $\gamma_0=16\text{GHz}$ , linewidth enhancement factor  $\alpha=-4.6$ , photon lifetime  $\tau_{ph}=10\text{ps}$ , carrier lifetime  $\tau_c=0.12\text{ns}$ , and linewidth  $0.5\text{MHz}$ , and also the fiber dispersion parameter  $\beta'' = -20\text{ps}^2/\text{km}$ .

The amount of optical power launched into the fiber was controlled with a variable optical attenuator and measurements of MR and RIN were performed at several optical powers and modulation powers for the forward and backward propagating fields.

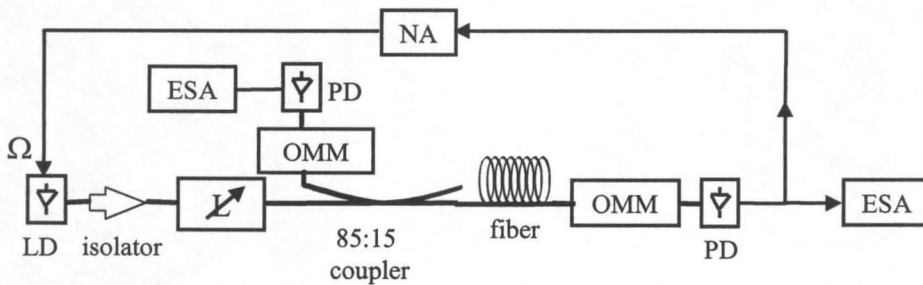


Figure 5: Experimental set-up. LD=laser diode, L=variable optical attenuator, OMM=optical multimeter, PD=photodetector, NA=network analyzer, ESA=electric spectrum analyzer.

#### IV.2.2.B Small-signal experiments

Figure 6 shows  $|H(\Omega, z)|^2$  for a small modulation power and several optical input powers. At low modulation frequencies, the laser chirp (see equation (4) in Chapter III) is dominated by the adiabatic term and varies as  $1/\Omega$ . A negative  $\theta_{NL}$

results in part of this chirp converted into IM, and  $|H(\Omega, z)|^2$  increases with decreasing  $\Omega$  as  $1/\Omega$ . At high  $\Omega$ , and using the normalization explained above,  $|H(\Omega, z)|^2$  approaches its linear regime value.

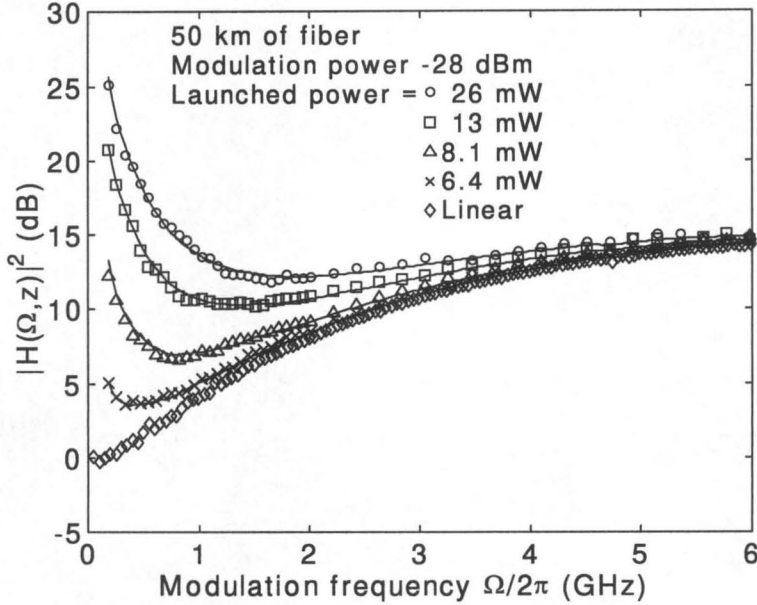


Figure 6: Change in modulation response,  $|H(\Omega, z)|^2$ , for 50 km of fiber, -28dBm modulation power, and several launched powers into the fiber. Diamonds is measured  $|H(\Omega, z)|^2$  in the absence of nonlinear effects. Solid is theory.

Since the modulation power is very small ( $m_{IM} \approx 0.08\%$ ), the small-signal approximation is valid and equation (17)-(19) can be used to determine the nonlinear phase change  $\theta_{NL}$ . Using  $\theta_{NL}$  as the only fitting parameter, the solid curves in Figure 6 are obtained, which indicate that the theory above accounts well for the experimental results.



Figure 7 shows the measured  $\theta_{NL}$  together with the backscattered and forward output powers as a function of the optical input power. Using  $g_{B0} / A_{eff} \approx 0.06 \text{mW}^{-1} \text{km}^{-1}$  and  $\int_0^L |a_2|^2 dz \approx |a_2(0)|^2 L_{eff} / 2$ , where  $|a_2(0)|^2$  is the backscattered power and  $L_{eff}$  is the fiber effective length, in equation (12), the dotted trace in Figure 7 is obtained for the nonlinear phase shift. Thus, it can be concluded that this effect has the correct sign and magnitude to produce the nonlinear phase change experimentally measured.

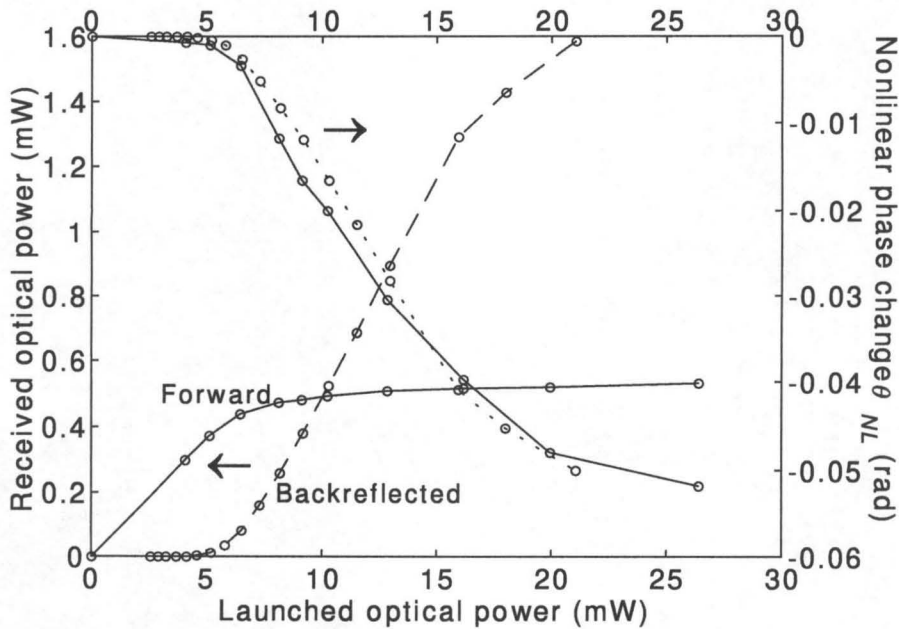
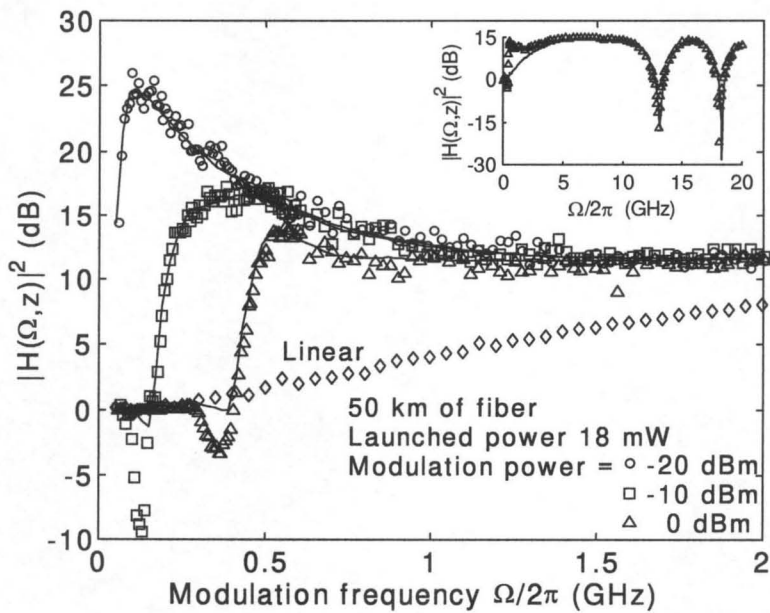


Figure 7: Left axis: forward (solid) and backscattered (dashed) optical powers for 50 km of fiber. Right axis: nonlinear phase change (solid is experimental, dotted is theoretical prediction as described in text).

#### IV.2.2.C Quasi-large-signal experiments

Figure 8 shows the measured  $|H(\Omega, z)|^2$  and received power for several modulation powers. Since  $L(\Omega, z)$  is difficult to measure, the same normalization as that

in the small-signal case is used as if the modulation sidebands only suffered linear fiber loss, i.e.,  $H(\Omega, z) \equiv (LL_{Lin})^{1/2} \frac{I(\Omega, z)}{I(\Omega, 0)}$ . This is not a valid assumption at large modulation powers and low  $\Omega$ , i.e., for large laser chirp. In fact, for  $m_{FM} \approx 2.4$  then  $J_0(m_{FM}) \approx 0$ , and most of the optical power is contained in the first sideband, which is then partly backscattered by SBS, and  $L(\Omega, z) > L_{Lin}$ . As a consequence of the normalization used,  $|H(\Omega, z)|^2$  becomes negative (in dB). As the bandwidth of the signal increases, the SBS is reduced, and the received power rises. The ripple in  $|H(\Omega, z)|^2$  and received power at low frequencies is due to the oscillatory behavior of the Bessel functions. On the contrary, the structure observed in the received power at  $\Omega/2\pi \sim 0.7$  GHz is due to the frequency response of the microwave probe employed to modulate the laser.



(a)

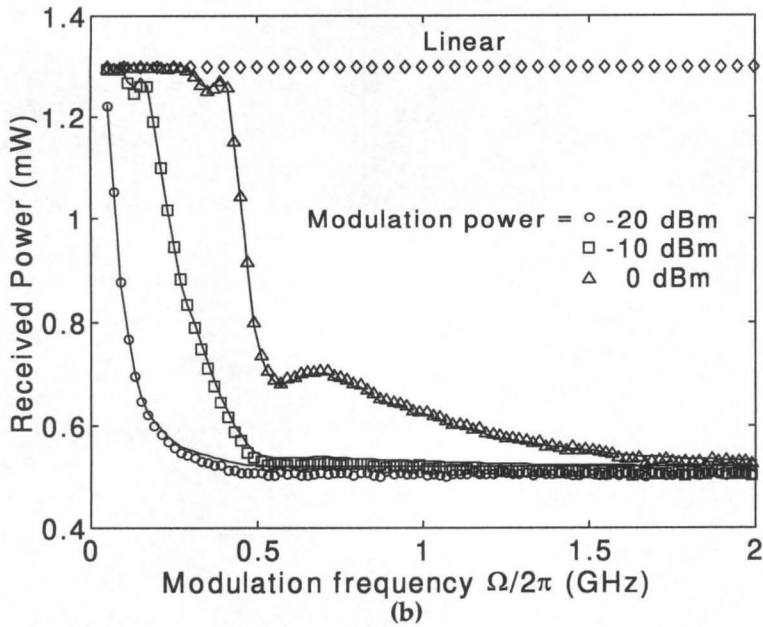


Figure 8: (a) Change in modulation response,  $|H(\Omega, z)|^2$  and (b) received power, as function of modulation frequency for 50km of fiber, 18mW of launched optical power and several modulation powers. Diamonds is measured data in the absence of nonlinear effects. Solid is theory. The inset in (a) shows  $|H(\Omega, z)|^2$  in an extended frequency range for 18mW optical power (triangles) and linear regime (solid) with 0dBm modulation power.

The large-signal theory described above was used to explain the experimental data and is represented in Figure 8 with a solid trace. To determine  $L(n\Omega, z)$  and  $\theta(n\Omega, z)$ , cross-interaction between sidebands is neglected, as in the small-signal case. Then, it can be assumed that the power loss and phase change in each FM sideband can be extracted from the previous data in Figure 7, for the given power in the FM band. Good agreement has been found between this simple model and the measurement. The main discrepancy occurs when  $|H(\Omega, z)|^2$  becomes negative in dB, which our model underestimates. This is attributed to the assumption of no cross-interaction.

The inset in Figure 8 shows  $|H(\Omega, z)|^2$  in an extended frequency range for both linear and nonlinear regimes. It is observed that at high  $\Omega$ , and with the normalization in (17)-(19), both curves coincide. Thus, the effect of self-phase-modulation (SPM) that was recently reported in [14], does not appear in our data, which indicates that SBS manifests at lower optical powers than SPM.

### IV.3 EFFECT OF SBS ON RELATIVE INTENSITY NOISE

#### IV.3.1 Theory.

The presence of stimulated Brillouin scattering (SBS) alters the relative intensity noise (RIN) in two ways. First, excess noise appears around 0Hz and around harmonics of the acoustic wave frequency for both backward and forward propagating fields [15]. Second, it is shown here that the SBS induced phase change in the optical carrier results in conversion of part of the FM noise into IM noise, which causes additional excess noise at low frequencies.

The FM-to-IM conversion of laser noise can be treated in a way similar to the case of MR in section IV.2. The *PIR* due to photon fluctuations, which are generated by a Langevin noise source  $F_p$ , is given by:

$$PIR|_{F_p} \equiv \frac{\Delta\phi}{\Delta P/P}|_{F_p} = -\frac{\alpha \Omega_0^2}{2 \Omega^2} \frac{1 + i\Omega\tau_{ph}}{1 + 1/(i\Omega\tau_c)} \quad (25)$$

As  $\Omega$  decreases the *PIR* increases, and a small phase change of the optical carrier can result in a strong enhancement of the noise.

The RIN spectrum of the forward (backward) wave exhibits excess noise around harmonics of  $\Omega_B$  due to mixing upon detection of the incident (Stokes) wave with small reflections of the Stokes (incident) wave caused by Rayleigh scattering [15]. When the laser is modulated at a frequency  $\Omega$ , SBS induces additional excess noise at frequencies  $m\Omega_B + n\Omega$ , with  $m$  and  $n$  integers.

### IV.3.2 Experiment.

Figure 9 shows the low-frequency increase in RIN for several launched powers in the fiber. Equations (17)-(19) together with (25) can be used to determine  $\theta_{NL}$ , which is shown in the inset. The slight discrepancy between experiment and theory is attributed to the simple model used to describe the RIN, which does not include the effect of side modes [16] and FM-to-IM noise conversion due to double Rayleigh scattering [17]. These two effects are independent of the launched power and explain why  $\theta_{NL}$  does not equal exactly zero at small launched powers. The excess noise induced by SBS near 0Hz reported in [15] would affect frequencies below the ones here considered and does not need to be included in the analysis.

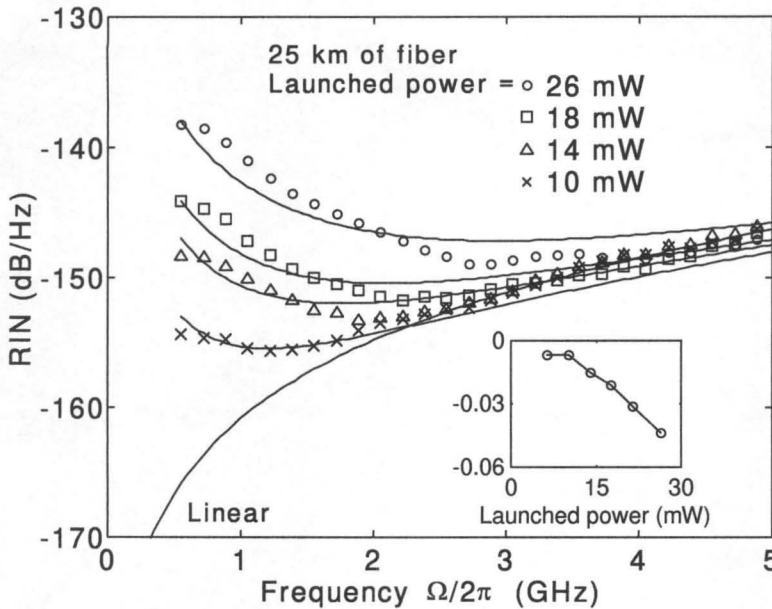
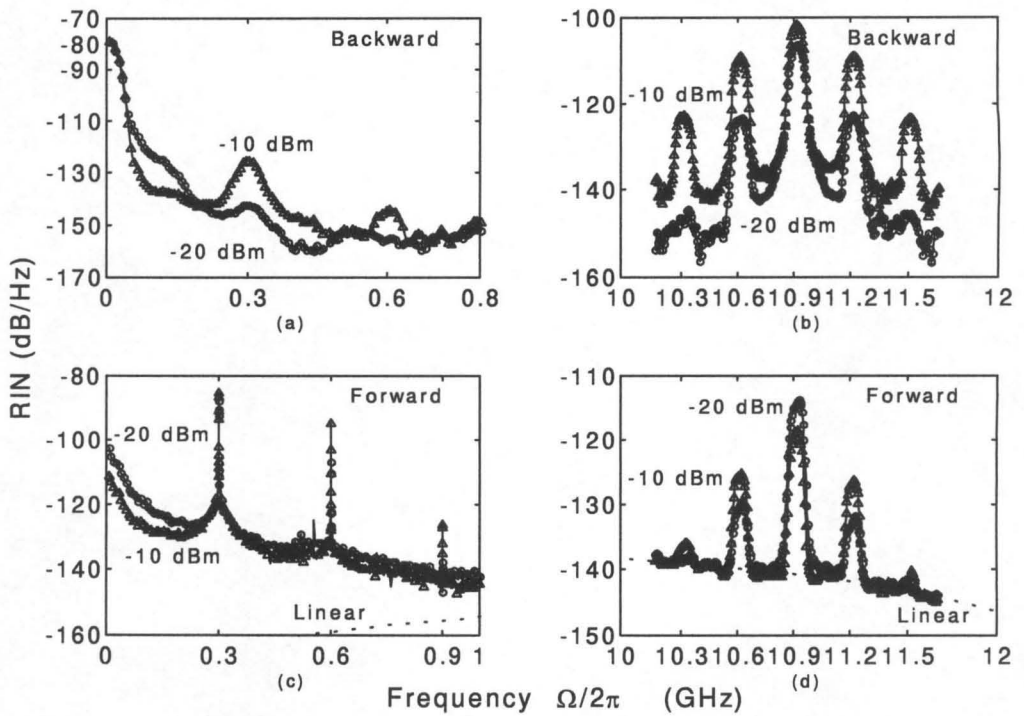


Figure 9: Relative intensity noise (RIN) for 25 km of fiber and several launched powers into the fiber. Solid line is theory. The inset shows the nonlinear phase change as a function of launched power.

Figure 10 displays the measured RIN of the forward and backward fields after propagation in 75 km of fiber for frequencies around 0Hz and  $\Omega_B$ . The power launched

into the fiber was 13dBm and the laser was directly modulated at 300MHz with several modulation powers. As can be observed in Figure 10a, the excess noise due to FM-to-IM conversion also appears at harmonics of the modulation frequency,  $n\Omega$ . As discussed in section IV.2, for sufficiently high modulation power and low modulation frequency the input optical power is distributed in many sidebands, and the SBS, and consequently the excess noise, is suppressed.



**Figure 10:** RIN of forward, (a) and (b), and backward, (c) and (d), propagating waves after 50 km of fiber at low frequencies, (a) and (c), and around  $\Omega_B$ , (b) and (d). The laser light was directly modulated at 300MHz with modulation powers (MP) -20dBm (circles) and -10dBm (triangles).

The RIN spectrum of the backward Stokes wave at 0Hz (Figure 10c) can be used to determine the spectrum of the Brillouin gain [18] and gives a rough estimate of the Brillouin bandwidth to be around 15MHz. The measured RIN level of the Stokes wave was approximately -80dB/Hz (irrespective of fiber length and launched power), which

can be related to the strength of the Langevin noise source that describes the thermal excitation of acoustic waves [19]. Residual excess noise at harmonics of the modulation frequency is due to SBS backscattering of the incident field sidebands rather than beating of the small reflection of the incident field with itself.

The excess noise of the Stokes wave around  $\Omega_B$  (Figure 10d) can be well explained as originating from mixing of the Stokes wave with a small reflection of the modulated incident wave caused by Rayleigh scattering. Thus, the complex electric field amplitude of the backward propagating wave at the fiber input,  $\tilde{E}_B$ , can be expressed approximately as:

$$\tilde{E}_B = P_S^{1/2} + \gamma_R \bar{P}_0^{1/2} \sum_n c_n e^{in(\Omega t + \varphi_{FM})} e^{i\Omega_B t} \quad (26)$$

where  $P_S$  is the backreflected Stokes power at the fiber input,  $\bar{P}_0$  is the integrated power of the forward propagating field along the fiber, and  $\gamma_R$  is the field reflection coefficient due to Rayleigh scattering. The RIN power (RINP) at  $\Omega_B + n\Omega$  can be determined experimentally by integrating the RIN over the spectral width of the spike (or by normalizing the RIN by the value at 0Hz). From equation (26), it can be derived that the RINP of the backward propagating field,  $RINP_B$ , is proportional to  $|c_n|^2$ , that is:

$$RINP_B(\Omega_B + n\Omega) = 2 \frac{\bar{P}_0}{P_S} |\gamma_R|^2 |c_n|^2 \quad (27)$$

Figure 11 shows the factor  $|\gamma_R|^2 |c_n|^2$  determined from the experimentally measured  $RINP_B$  and equation (27). The value of  $\bar{P}_0$  was estimated by assuming an exponential decay of the forward propagating field. By comparing this with  $|c_n|^2$  from (21) (dotted line in Figure 11), we obtain  $|\gamma_R|^2 = -35.5\text{dB}$ , which agrees well with the value expected for Rayleigh scattering.



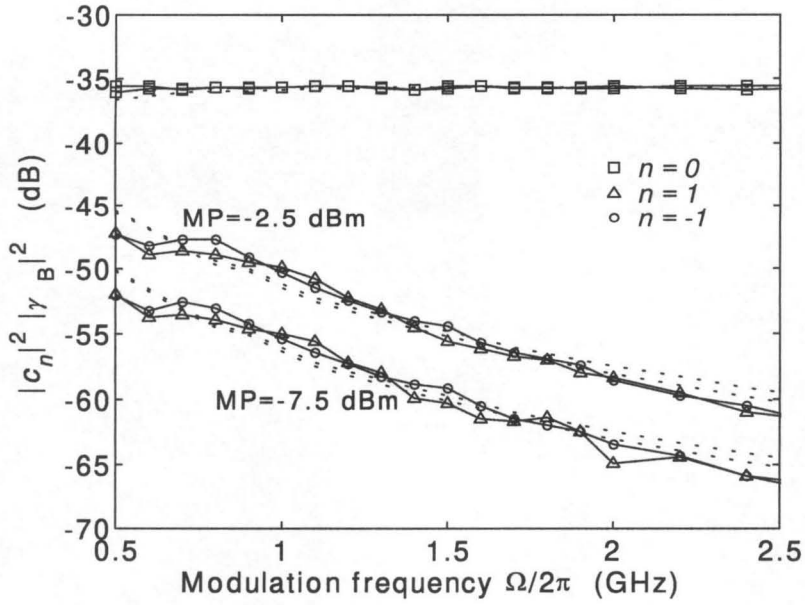


Figure 11: Factor  $|c_n|^2 |\gamma_B|^2$  derived from the measured RIN power of the backward propagating field at the fiber input at  $\Omega_B + n\Omega$  as a function of modulation frequency,  $\Omega/2\pi$ , for two different modulation powers (MP) after 75 km of fiber. The dashed line is obtained with  $|\gamma_R|^2 = -35.5$  dB and  $|c_n|^2$  as determined from the laser chirp and modulation power.



## Appendix IV.1 VECTOR THEORY OF THE ACOUSTOOPTIC INTERACTION IN OPTICAL FIBER

A solid can become strained when placed in an electric field through an effect known as electrostriction. In piezoelectric materials, the stress is linearly proportional to the applied electric field. However, isotropic materials such as glass are always non-piezoelectric. The reason for this is that reversing the sign of the electric field does not change the physical situation and the refractive index and strain should remain essentially unaltered. As a consequence, the linear effect vanishes, and the quadratic dependence of the stress on the electric field has to be considered. On the other hand, certain materials develop an electric moment under stress and, as a consequence, the dielectric constant is a function of the strain. In this case the linear effect does not vanish and is the first order effect. Physically, reversing the sign of the strain changes the state of the solid from tension to compression, and so, in general, modifies the dielectric constant.

The three field variables that characterize the acoustic wave, the particle displacement vector,  $\mathbf{u}(\mathbf{r},t)$ , the strain tensor,  $\sigma(\mathbf{r},t)$ , and the stress tensor,  $\tau(\mathbf{r},t)$  are related by the equation of motion [20]-[21],

$$\nabla \cdot \tau = \rho_0 \frac{\partial^2 \mathbf{u}}{\partial t^2} \quad (28)$$

the strain-displacement relation,

$$\sigma = \nabla_s \mathbf{u} \quad (29)$$

and the elastic constitutive equation or Hooke's law, which for a non-piezoelectric material is given by:

$$\tau = \mathbf{c} : \sigma + \eta : \frac{\partial \sigma}{\partial t} + \frac{1}{2} \gamma : (\mathbf{E} \cdot \mathbf{E}') \quad (30)$$

Here,  $\rho_0$  is the material density,  $\mathbf{c}$  is the elastic stiffness tensor,  $\eta$  is the viscosity tensor, which accounts for the existence of dissipative or frictional forces [22],  $\gamma$  is the

electrostriction tensor, which describes the stress resulting from the electric field,  $\mathbf{E}$ , and the operator  $\nabla_s$  takes the symmetric part of the displacement gradient, i.e.,

$$\sigma_{ij} = \frac{1}{2} \left( \frac{\partial u_i}{\partial x_j} + \frac{\partial u_j}{\partial x_i} \right) = \sigma_{ji}.$$

The change in optical dielectric constant tensor,  $\epsilon$ , induced by the acoustic wave is given by:

$$\Delta \left( \frac{\epsilon_0}{\epsilon} \right) = \mathbf{p} : \boldsymbol{\sigma} \quad (31)$$

where  $\mathbf{p}$  is the strain-optic tensor. It can be shown that the tensors  $\gamma$  and  $\mathbf{p}$  are proportional [23].

The form of the tensors that describe the acoustooptic interaction can be derived from considerations of the symmetry of the medium. In an isotropic material such as glass,  $\epsilon$  is described by just one parameter, which, under suitable axes, is the value in the diagonal. On the other hand, the 4<sup>th</sup> rank tensors,  $\mathbf{p}$ ,  $\eta$  and  $\gamma$ , have all the same form, and each of them can be reduced to just two constants. For the stiffness tensor, these are the Lamé's constants,  $\lambda$  and  $\mu$ . By substituting these tensors into (30) and (31), simplified expressions for the acoustic equation of motion, (28), and the nonlinear polarization,  $\mathbf{P}^{NL}$ , are obtained as:

$$\begin{aligned} \rho_0 \frac{\partial^2 \mathbf{u}}{\partial t^2} = & \\ = \left[ \rho_0 v_l^2 + \eta_{11} \frac{\partial}{\partial t} \right] \nabla (\nabla \cdot \mathbf{u}) - \left[ \rho_0 v_t^2 + \eta_{44} \frac{\partial}{\partial t} \right] \nabla \times \nabla \times \mathbf{u} + \frac{\gamma_{12}}{2} \nabla E^2 + \gamma_{44} \nabla \cdot (\mathbf{E} \cdot \mathbf{E}^T) \end{aligned} \quad (32)$$

$$\mathbf{P}^{NL} = -\gamma_{12} (\nabla \cdot \mathbf{u}) \mathbf{E} - 2\gamma_{44} (\nabla_s \mathbf{u}) \cdot \mathbf{E} \quad (33)$$

where  $v_l^2 = \frac{\lambda + 2\mu}{\rho_0}$ , and  $v_t^2 = \frac{\mu}{\rho_0}$  are the squared longitudinal and transverse sound velocities, respectively.

The electrostriction constants are given by [23]:

$$\begin{aligned}\gamma_{12} &= n_0^4 \varepsilon_0 p_{12} \\ \gamma_{44} &= n_0^4 \varepsilon_0 p_{44} = n_0^4 \varepsilon_0 \frac{1}{2}(p_{11} - p_{12})\end{aligned}\quad (34)$$

where  $p_{11}=0.121$  and  $p_{12}=0.270$  are the strain-optic coefficients for fused quartz, and  $n_0$  is the refractive index.

The problem described by equations (32) and (33) is quite involved, but can be greatly simplified by neglecting transverse against longitudinal variations of the material displacement and the electric field, which is a valid approximation for the case considered here of backward Brillouin scattering in a single mode optical fiber. As shown below, in this case it is sufficient to consider the effect of  $\gamma_{12}$ , neglecting the contribution of  $\gamma_{44}$ , and we can express the equation of motion in terms of the material density variation,  $\rho$ , which, in analogy with hydrodynamics, is defined as:

$$\rho = -\rho_0 \nabla \cdot \mathbf{u} \quad (35)$$

Substituting  $\rho$  in (32)-(33) the acoustic wave equation for the material density fluctuation (2) is derived, where  $\gamma=\gamma_{12}$  and  $\Gamma_s=\eta/\rho_0$ .

When the contribution of  $\gamma_{44}$  is included, the derivation continues as follows. In order to determine which acoustic modes are excited by the electric field  $\nabla E^2$  and  $\nabla \cdot (\mathbf{E} \cdot \mathbf{E}^T)$  have to be evaluated. The terms oscillating at  $\Omega_s$  are given by:

$$\nabla E^2(r, z, t) = a_1(z, t) a_2^*(z, t) \hat{\mathbf{e}}_1 \cdot \hat{\mathbf{e}}_2^* \begin{bmatrix} \frac{\partial E_0^2(r)}{\partial r} \\ 0 \\ -ikE_0^2(r) \end{bmatrix} e^{i(\Omega_s t - k_s z)} \quad (36)$$

$$\begin{aligned} \nabla \cdot (\mathbf{E} \cdot \mathbf{E}^T)(r, \varphi, z, t) &= \frac{1}{2} a_1(z, t) a_2^*(z, t) \frac{\partial E_0^2(r)}{\partial r} e^{i(\Omega_s t - k_s z)} \\ &\left\{ \begin{bmatrix} e_{1x} e_{2x}^* + e_{1y} e_{2y}^* \\ 0 \\ 0 \end{bmatrix} + \begin{bmatrix} \cos(2\varphi)(e_{1x} e_{2x}^* - e_{1y} e_{2y}^*) + \sin(2\varphi)(e_{1x} e_{2y}^* + e_{1y} e_{2x}^*) \\ \cos(2\varphi)(e_{1x} e_{2x}^* + e_{1y} e_{2y}^*) + \sin(2\varphi)(e_{1x} e_{2y}^* - e_{1y} e_{2x}^*) \\ 0 \end{bmatrix} \right\} \end{aligned} \quad (37)$$

where the three vector components are directed along  $\hat{\mathbf{r}}$ ,  $\hat{\boldsymbol{\phi}}$  and  $\hat{\mathbf{z}}$ . Thus, the electric field will excite acoustic modes with no azimuthal variation,  $\mathbf{u}_{0n}$ , and modes varying sinusoidally as  $2\varphi$ ,  $\mathbf{u}_{2n}$ .

Next the nonlinear polarization (33) is analyzed to determine which acoustic modes can excite the fundamental fiber mode. The necessary condition is that  $\nabla \cdot \mathbf{u}$  and  $\nabla_s \mathbf{u}$  have no azimuthal variation. For  $\nabla \cdot \mathbf{u}$  this is only satisfied for modes  $\mathbf{u}_{0n}$ . Let's examine now  $\nabla_s \mathbf{u}$ :

$$\begin{aligned} \nabla_s \mathbf{u} = & \frac{1}{2} \left\{ \left( \frac{\partial u_r}{\partial r} + \frac{u_r}{r} + \frac{1}{r} \frac{\partial u_\varphi}{\partial r} \right) (\hat{\mathbf{x}}\hat{\mathbf{x}} + \hat{\mathbf{y}}\hat{\mathbf{y}}) + 2 \frac{\partial u_z}{\partial r} \hat{\mathbf{z}}\hat{\mathbf{z}} + \right. \\ & + \left( \frac{\partial u_r}{\partial r} - \frac{u_r}{r} - \frac{1}{r} \frac{\partial u_\varphi}{\partial r} \right) [\cos(2\varphi)(\hat{\mathbf{x}}\hat{\mathbf{x}} - \hat{\mathbf{y}}\hat{\mathbf{y}}) + \sin(2\varphi)(\hat{\mathbf{x}}\hat{\mathbf{y}} - \hat{\mathbf{y}}\hat{\mathbf{x}})] + \\ & + \left( r \frac{\partial}{\partial r} \left( \frac{u_\varphi}{r} \right) + \frac{1}{r} \frac{\partial u_r}{\partial \varphi} \right) [\sin(2\varphi)(-\hat{\mathbf{x}}\hat{\mathbf{x}} + \hat{\mathbf{y}}\hat{\mathbf{y}}) + \cos(2\varphi)(\hat{\mathbf{x}}\hat{\mathbf{y}} + \hat{\mathbf{y}}\hat{\mathbf{x}})] + \\ & \left. + \left( \frac{\partial u_z}{\partial r} + \frac{\partial u_r}{\partial z} \right) [\cos(\varphi)\hat{\mathbf{x}}\hat{\mathbf{z}} + \sin(\varphi)\hat{\mathbf{y}}\hat{\mathbf{z}}] + \left( \frac{\partial u_\varphi}{\partial z} + \frac{\partial u_z}{\partial \varphi} \right) [-\sin(\varphi)\hat{\mathbf{x}}\hat{\mathbf{z}} + \cos(\varphi)\hat{\mathbf{y}}\hat{\mathbf{z}}] \right\} \end{aligned} \quad (38)$$

From (38) it can be concluded that modes  $\mathbf{u}_{0n}$  in combination with factors in (38) with no azimuthal variation and modes  $\mathbf{u}_{2n}$  in combination with factors in (38) varying as  $2\varphi$  will excite the fundamental fiber mode.

The approximation in section IV.1 is justified from (38) since the only terms from  $\nabla_s \mathbf{u}$  that contribute to  $\mathbf{P}_{NL}$  are proportional to transverse variations of the material displacement. Similarly, only transverse derivatives of the electric field appear in the expression for  $\nabla \cdot (\mathbf{E} \cdot \mathbf{E}^T)$  in (37).

The material displacement in the presence of excitation can be expanded in terms of the eigenmodes as was done in equation (7), yielding:

$$\mathbf{u}(r, \varphi, z, t) = a_1(z, t) a_2^*(z, t) \left[ \sum_n c_n(z, t) \mathbf{u}_{0n}(r, \varphi) + d_n(z, t) \mathbf{u}_{2n}(r, \varphi) \right] e^{i(\Omega_s t - k_s z)} + \text{c.c.} \quad (39)$$

A similar approach to that in section IV.1 can be followed to determine the coefficients of this expansion.

Equations (33),(38) show that, even though the material is isotropic, due to the acoustooptic interaction it becomes anisotropic and birefringent.

## Appendix IV.2 SOME USEFUL INTEGRALS

The inner product used in this work is defined as

$$\langle \rho_n, \rho_m \rangle = \int_0^{2\pi} \int_0^a r \rho_n(r, \varphi) \rho_m^*(r, \varphi) dr d\varphi \quad (40)$$

Using

$$\int_0^1 r J_\nu(pr) J_\nu(qr) dr = \begin{cases} \frac{1}{2} (J_\nu^2(pr) - J_{\nu+1}(pr) J_{\nu-1}(pr)) & \text{if } p = q \\ \frac{p J_{\nu+1}(pr) J_\nu(qr) - q J_\nu(pr) J_{\nu+1}(qr)}{p^2 - q^2} & \text{if } p \neq q \end{cases} \quad (41)$$

we find

$$\langle \rho_n, \rho_m \rangle = 2 \frac{k_{ln} J_1(k_{ln} a_{cl}) J_0(k_{lm} a_{cl}) - k_{lm} J_0(k_{ln} a_{cl}) J_1(k_{lm} a_{cl})}{[k_{ln}^2 - k_{lm}^2] [J_0^2(k_{ln} a_{cl}) + J_1^2(k_{ln} a_{cl})]^{\frac{1}{2}} [J_0^2(k_{lm} a_{cl}) + J_1^2(k_{lm} a_{cl})]^{\frac{1}{2}}}, \quad (42)$$

$n \neq m$

By using a Gaussian approximation for the fundamental fiber mode with mode beam

waist  $w$ ,  $E_0(r) = \left( \frac{\omega\mu}{\pi w^2 \beta} \right)^{\frac{1}{2}} \exp\left(-\frac{r^2}{2w^2}\right)$ , where  $E_0(r)$  is normalized so that  $|a_i|^2$  equals

the power carried by mode  $i$ , i.e.,  $\langle E_0, E_0 \rangle = \frac{\omega\mu}{\beta}$ , we obtain

$$\langle E_0^2, \rho_m \rangle \cong 2\pi \int_0^\infty r E_0^2(r) \rho_m(r) dr = \frac{\omega\mu}{\beta} \frac{e^{-\left(\frac{k_{lm} w}{2}\right)^2}}{(\pi a_{cl}^2)^{\frac{1}{2}} [J_0^2(k_{lm} a_{cl}) + J_1^2(k_{lm} a_{cl})]^{\frac{1}{2}}} \quad (43)$$

## REFERENCES


- [1] G. P. Agrawal, *Nonlinear fiber optics*, Academic Press, London, 1995.
- [2] A. R. Chraplyvy, "Limitation on lightwave communications imposed by optical fiber nonlinearities," *J. Lightwave Technol.*, vol. 8, 10, pp. 1548-1557, 1990.
- [3] D. A. Fishman, J. A. Nagel, "Degradations due to stimulated Brillouin scattering in multigigabit intensity-modulated fiber-optic systems," *J. Lightwave Technol.*, vol. 11, 11, pp. 1721-1728, Nov., 1993.
- [4] H. Yoshinaga, M. Kagami, K. Kikushima, K. Suto, "Nonlinear distortion due to stimulated Brillouin scattering and its suppression in SCM video-transmission systems," *OFC/IOOC*, pp. 257-258, 1993.
- [5] R. G. Smith, "Optical power handling capacity of low loss optical fibers as determined by stimulated Brillouin and Raman scattering," *Appl. Opt.*, vol. 11, 11, pp. 2489-2492, 1972.
- [6] J. Stone, A. R. Chraplyvy, "Spontaneous Brillouin noise in long-distance high-bandwidth optical-fiber transmission," *Electron. Lett.*, vol. 19, 8, pp. 275-277, 1983.
- [7] R. M. Shelby, M. D. Levenson, P. W. Bayer, "Guided acoustic-wave Brillouin scattering," *Phys. Rev. B*, vol. 31, 8, pp. 5244-5252, Apr., 1985.
- [8] E. M. Dianov, A. V. Luchnikov, A. N. Pilipetskii, A. N. Starodumov, "Long-range interaction of soliton pulse trains in a single-mode fibre," *Sov. Lightwave Commun.*, vol. 1, pp. 37-43, 1991.
- [9] A. Fellegara, S. Wabnitz, "Electrostrictive cross-phase modulation of periodic pulse trains in optical fibers," *Opt. Lett.*, vol. 23, 17, pp. 1357-1359, Sep., 1998.
- [10] N. Shibata, R. G. Waarts, R. P. Braun, "Brillouin gain spectra for single mode fibers having pure silica, GeO<sub>2</sub> doped, and P<sub>2</sub>O<sub>5</sub> doped cores," *Opt. Lett.*, vol. 12, 4, pp. 269-271, Apr., 1987.
- [11] E. Peral, W. K. Marshall, A. Yariv, "Precise measurement of semiconductor laser chirp using effect of propagation in dispersive fiber and application to simulation

- of transmission through fiber gratings," *J. Lightwave Technol.*, vol. 16, 10, pp. 1874-1880, Oct. 1998.
- [12] A. Royset, L. Bjerkan, D. Myhre, L. Hafskjaer, "Use of dispersive optical fiber for characterisation of chirp in semiconductor lasers," *Electron. Lett.*, vol. 30, 9, pp. 710-712, Apr., 1994.
- [13] B. Wedding, "Analysis of fiber transfer function and determination of receiver frequency response for dispersion supported transmission," *Electron. Lett.*, vol. 30, 1, pp. 58-59, Jan., 1994.
- [14] A. Cartaxo, B. Wedding, W. Idler, "Influence of fiber nonlinearity on the phase noise to intensity noise conversion in fiber transmission: theoretical and experimental analysis," *J. Lightwave Technol.*, vol. 16, 7, pp. 1187-1193, Jul., 1998.
- [15] M. Horowitz, A. R. Chraplyvy, R. W. Tkach, J. L. Zyskind, "Broadband transmitted intensity noise induced by Stokes and anti-Stokes Brillouin scattering in single-mode fibers," *IEEE Photon. Technol. Lett.*, vol. 9, 1, pp. 124-126, Jan., 1997.
- [16] E. Peral, W. K. Marshall, D. Provenzano, A. Yariv, "Effect of many weak side modes on relative intensity noise of distributed feedback semiconductor lasers," *Appl. Phys. Lett.*, vol. 72, 8, pp. 888-890, Feb., 1998.
- [17] S. Wu, A. Yariv, "Theoretical and experimental investigation of conversion of phase noise to intensity noise by Rayleigh scattering in optical fibers," *App. Phys. Lett.*, vol. 59, 10, pp. 1156-1158, Sep., 1991.
- [18] A. D. Kersey, M. A. Davis, "Brillouin bandwidth determination from excess-noise characteristics of SBS signals in single-mode fibers," *OFC/IOOC*, pp. 206, 1993.
- [19] R. W. Boyd, K. Rzazewski, "Noise initiation of stimulated Brillouin scattering," *Phys. Rev. A*, vol. 42, 9, pp. 5514-5521, Nov., 1990.
- [20] B. A. Auld, *Acoustic fields and waves in solids*, Krieger, Malabar, 1990.
- [21] J. D. Achenbach, *Wave propagation in elastic solids*, N. Holland, Amsterdam, 1973.
- [22] Landau, Lifshitz, *Theory of Elasticity*, Pergamon Press, Oxford, 1986.
- [23] J. F. Nye, *Physical properties of crystals*, Clarendon Press, Oxford, 1957.



## Chapter V.

# New schemes of mode conversion

 Optical waveguides can confine optical energy in one or more optical modes, which are characterized by a number of mode parameters such as the spatial distribution of optical energy, the propagation constant, and the polarization state. Two different modes may couple to each other and exchange energy under proper conditions. Mode conversion refers to the complete transfer of energy in one optical mode to another. Such mode conversion can be used to perform various optical operations on guided optical waves and has been applied in optical communications and optical sensor devices.

Coupling between interacting optical modes is usually treated using coupled mode theory [1], [2]. In section V.1, this coupled mode theory is generalized to the case of multimode waveguide structures (with one or more waveguides), and the propagating eigenmodes, the so-called supermodes, of the structure are derived. The supermode theory allows simple analysis of complex devices such as those including adiabatic transitions.

In sections V.2 a new approach for mode conversion between copropagating modes is proposed, where the mode conversion is mediated by a third mode. It will be shown that this additional mode affords additional flexibility and as a result the devices are less sensitive to fabrication parameters compared to previous devices. Low insertion

loss, low polarization sensitivity and both narrow-band and broadband operation can be obtained.

## **V.1 SUPERMODES OF MULTIMODE WAVEGUIDE STRUCTURES.**

### **V.1.1 Introduction**

The theory of coupled modes for guided wave optics [1], [2] was developed for treating interactions between, mostly, confined modes of optical waveguides which are mediated by refractive index perturbations. Two of the most important examples are those of periodic index perturbation (DFB lasers [3] Bragg fiber gratings [4]) and coupling via evanescent fields in parallel waveguide systems [5].

As a result of the perturbation, the modes of the structure are modified, and the propagating eigenmodes, the so-called supermodes, of the perturbed structure [5], [6] have to be found. For quasi-periodic perturbations, these are the Floquet-Bloch modes [7]-[9].

The use of supermodes becomes a practical necessity in analyzing a new and emerging class of WDM-related devices [10] based on adiabatic transitions and/or where several waveguide modes might be involved.

Here formal expressions for the supermodes of waveguide structures with an arbitrary number of modes will be derived. The supermodes, in these cases, become the natural new building blocks in which to analyze phenomena and devices. A metric is derived from considerations of power flux conservation to ensure orthonormality of the supermodes.

### V.1.2 Generalized coupled mode theory

The transverse modes of a dielectric waveguide, which form a complete orthonormal set, cease to be proper modes when a spatial modulation of the index of refraction or the gain (loss) is present, and the new eigenmodes, the so-call supermodes, have to be determined.

Consider a dielectric structure consisting of an array of several waveguides supporting one or several modes, totaling  $N$  modes. Assuming that the waveguides are weakly guiding, the modes of the individual waveguides in isolation and in the absence of refractive index perturbation are transverse and can be expressed as:

$$\vec{E}_k(x, y, z, t) = \vec{E}_k(x, y) e^{-i\beta_k z} e^{i\omega t} \quad k = 1, \dots, N \quad (1)$$

where the  $\beta_k$  are the propagation constants of the waveguide modes, with  $\beta_k > 0$  for forward propagating modes, and  $\beta_k < 0$  for modes propagating in the  $-z$  direction. The  $\vec{E}_k(x, y)$  describe the transverse profile of the fields, and satisfy the following wave equation:

$$\nabla_t^2 \vec{E}_k(x, y) + (k_0^2 n_k^2 - \beta_k^2) \vec{E}_k(x, y) = 0 \quad k = 1, \dots, N \quad (2)$$

where  $\nabla_t^2$  is the laplacian operator in the transverse coordinates,  $k_0 = 2\pi/\lambda$  is the wavevector in free space, and  $n_k$  is the refractive index of the isolated and unperturbed waveguide  $k$ . For weakly guiding waveguides, (2) can be simplified to:

$$\nabla_t^2 \vec{E}_k(x, y) + 2k_0 n_0 (k_0 (n_k - n_0) - (\beta_k - k_0 n_0)) \vec{E}_k(x, y) = 0 \quad k = 1, \dots, N \quad (3)$$

These waveguide modes are *not* necessarily orthogonal (only waveguide modes of the same waveguide are always orthogonal) and are *not* the modes of the dielectric structure, which consists of all waveguides with possibly an additional perturbation of the refractive index. The electric field in the structure can be expressed as a superposition of its own modes, known as supermodes, as follows:

$$\vec{E}(x, y, z, t) = \sum_{k=1}^N \hat{A}_k \vec{E}_k(x, y) e^{-i\hat{\beta}_k z} e^{i\omega t} \quad (4)$$

where the  $\hat{\beta}_k$  and  $\vec{E}_k(x, y)$  are the propagation constants and transverse profiles of the supermodes and  $\hat{A}_k$  are the supermode amplitudes.

In general, it is difficult to obtain the exact supermodes using analytical techniques. But if the coupling between the waveguides and the perturbation in the refractive index are weak enough, it is possible to express the electric field approximately as a superposition of the modes of the unperturbed waveguides in isolation as follows [5], [11]:

$$\vec{E}(x, y, z, t) = \sum_k A_k(z) \vec{E}_k(x, y) e^{-i\beta_k z} e^{i\omega t} \quad (5)$$

Substitution of this expansion in the wave equation yields:

$$\sum_k \left( -is_k \frac{dA_k(z)}{dz} + k_0 n_0 (n - n_k) A_k(z) \right) \vec{E}_k(x, y) e^{-i\beta_k z} = 0 \quad (6)$$

where  $n$  is the refractive index of the perturbed dielectric structure and  $s_k$  equals +1 for forward propagating modes and -1 for backward propagating modes. In deriving (6), the slowly-varying envelope approximation for the mode amplitude coefficients,  $A_k$ , and the weakly-guiding approximations were used.

Multiplying (6) by  $\vec{E}_j(x, y)$  and integrating over the transverse surface, we obtain

$$\sum_k is_k \rho_{jk} \frac{dA_k(z)}{dz} e^{-i(\beta_k - \beta_j)z} = \sum_k \tilde{\kappa}_{jk} A_k(z) e^{-i(\beta_k - \beta_j)z} \quad (7)$$

where the coupling coefficient,  $\tilde{\kappa}_{jk}$ , and the overlap integral,  $\rho_{jk}$ , are defined as

$$\tilde{\kappa}_{jk} = \iint_S k_0 n_0 (n - n_0) \vec{E}_k(x, y) \cdot \vec{E}_j(x, y) dS \quad (8)$$

$$\rho_{jk} = \iint_S \vec{E}_k(x, y) \cdot \vec{E}_j(x, y) dS \quad (9)$$

It will be assumed that the fields are normalized as

$$\iint_S |\vec{E}_k(x, y)|^2 dS = 1 \quad (10)$$

so that  $\rho_{kk} = 1$ .

In general,  $n = n(x, y, z)$  is a function of the three spatial coordinates. Here, the more important case is considered of a quasi-periodic dependent perturbation in the longitudinal coordinate,  $z$ , as follows:

$$n - n_0 = \Delta n_{0k}(x, y) \Delta n_k(z) \left( 1 + \cos \left( \frac{2\pi}{\Lambda_k} z + \phi(z) \right) \right) \quad (11)$$

Equations (7) and (11) indicate that strong interaction or coupling between two modes with propagation constants  $\beta_k$  and  $\beta_j$  will only occur around wavelengths at which the so-called Bragg condition is satisfied:

$$\beta_k - \beta_j \pm \frac{2\pi}{\Lambda_k} \approx 0 \quad (12)$$

This phase-matching condition is equivalent to momentum conservation, where the momentum required to couple the modes is provided by the spatial perturbation. Only when  $\beta_k \approx \beta_j$  can exist interaction between modes  $k$  and  $j$  in the absence of grating.

In a dielectric structure there can coexist several gratings that couple different waveguide modes. Let  $\Lambda_{jk}$  be the period of some quasi-periodic perturbation or grating coupling modes  $k$  and  $j$  ( $\Lambda_{jk} = \infty$  for non grating-assisted coupling). Then, from (7), the coupled wave equations can be expressed as

$$\sum_k i\rho_{jk} \frac{dA_k(z)}{dz} e^{-i(\beta_k - \beta_j)z} = \sum_k S_k \kappa_{jk} A_k(z) e^{-i\delta_{jk}z} \quad (13)$$

where the detuning,  $\delta_{jk}$ , is defined as

$$\delta_{jk} = \beta_k - \beta_j \pm \frac{2\pi}{\Lambda_{jk}} \quad (14)$$

Here, the sign is chosen so as to satisfy the Bragg condition, i.e., to minimize the detuning  $\delta_{jk}$  at the wavelength of operation. In writing (13) the sinusoidally varying

part of the coupling coefficient has been removed and from (13), (8) and (11),  $\kappa_{jk}$  for grating-assisted coupling is given by

$$\kappa_{jk} = \frac{1}{2} \Delta n_k(z) e^{\mp i\phi(z)} \iint_S k_0 \Delta n_{0k}(x, y) \vec{E}_k(x, y) \cdot \vec{E}_j(x, y) dS \quad (15)$$

and for non grating-assisted coupling,

$$\kappa_{jk} = \Delta n_k(z) \iint_S k_0 \Delta n_{0k}(x, y) \vec{E}_k(x, y) \cdot \vec{E}_j(x, y) dS \quad (16)$$

It is convenient to remove the oscillatory term in the coupled mode equations (13) and use new mode amplitudes defined as

$$a_k = A_k \exp(-i\delta_k z) \quad (17)$$

where the reference detunings,  $\delta_k$ , have yet to be determined. On substitution in the coupled mode equations (13), the new equations are given by

$$\begin{aligned} & \sum_k i\rho_{jk} \frac{da_k}{dz} e^{-i(\beta_k - \beta_j - \delta_k + \delta_j)z} = \\ & = \sum_k \rho_{jk} \delta_k a_k e^{-i(\beta_k - \beta_j - \delta_k + \delta_j)z} + s_k \kappa_{jk} a_k e^{-i(\delta_{jk} - \delta_k + \delta_j)z} \end{aligned} \quad (18)$$

### V.1.3 On supermodes, orthogonality and power conservation.

In this section, the supermodes of multimode dielectric structures will be derived and important issues such as supermode orthogonality and power conservation will be discussed. Two particular cases that will be relevant in the following sections will be considered. First, coupling of modes propagating in several adjacent single-mode waveguides. In this case, it is assumed that all modes are copropagating and that the coupling is realized through the evanescent field, without gratings. The second example deals with grating-assisted coupling among modes in one multimode waveguide. In this case, we will consider modes which can be copropagating or counterpropagating.

### V.1.3.A Non grating-assisted coupling among the forward-propagating modes of several single-mode waveguide.

#### 1) *Supermodes.*

In this case,  $\Lambda_{jk} = \infty$  for all  $j$  and  $k$ . In addition, since all modes are copropagating,  $s_k = 1$  for all  $k$ . From (18), and choosing the reference detunings as  $\delta_k = \beta_k$ , the coupled mode equations are given by

$$\sum_k i\rho_{jk} \frac{da_k}{dz} = \sum_k (\rho_{jk}\beta_k + \kappa_{jk})a_k \quad (19)$$

which can be expressed in matrix notation as

$$iR \frac{da}{dz} = (RB + K)a \quad (20)$$

Here,  $a = [a_1 \ a_2 \ \dots \ a_N]^T$ , where the superscript  $T$  means transpose,  $[R]_{jk} = \rho_{jk}$ ,  $[K]_{jk} = \kappa_{jk}$ , and  $B$  is a diagonal matrix where the diagonal elements are the propagation constants,  $[B]_{kk} = \beta_k$ .

Equation (20) can also be written as

$$i \frac{da}{dz} = Ha \quad (21)$$

where the system matrix  $H$  is given by

$$H = B + R^{-1}K \quad (22)$$

If the coupling coefficients,  $\kappa_{ij}$ , do not depend on  $z$ , or vary very slowly (as in an adiabatic transition), it can be postulated that the vectors evolve as

$$a(z) = a(0)\exp(-i\hat{\beta}z) \quad (23)$$

which when used in (21) leads to

$$Ha = \hat{\beta}a \quad (24)$$

This is an eigenvalue equation that yields the (adiabatic) eigenvectors or supermodes and the eigenvalues,  $\hat{\beta}$ , or propagation constants of the supermodes. Thus, if the eigenvector  $k$  is  $\hat{E}_k = [\hat{E}_{1k} \ \hat{E}_{2k} \ \cdots \ \hat{E}_{Nk}]^T$ , corresponding to the eigenvalue  $\hat{\beta}_k$ , then the transverse profile of the supermode  $k$  is given by

$$\tilde{E}_k(x, y) = \sum_{j=1}^N \hat{E}_{jk} \bar{E}_k(x, y) \quad (25)$$

## 2) Orthogonality of supermodes.

In the previous section the supermodes of a grating-coupled multimode waveguide were derived. However, in order that any field can be easily expanded as a superposition of these modes, it is convenient that these supermodes are also orthonormal among themselves. In general,  $\kappa_{jk} \neq \kappa_{kj}$  and as a consequence it is not obvious from (20) and (21) that the eigenvectors, and thus the supermodes, are orthogonal. In the following it will be shown that the supermodes are indeed orthogonal.

Equation (2) is satisfied for any waveguide two modes  $j$  and  $k$ . Multiplication of equation (3) for mode  $j$  by  $\bar{E}_k(x, y)$ , and (3) for mode  $k$  by  $\bar{E}_j(x, y)$ , subtraction of the two resulting equations and integration along the transverse dimensions yields:

$$\iint_S (\bar{E}_k \cdot \nabla_t^2 \bar{E}_j - \bar{E}_j \cdot \nabla_t^2 \bar{E}_k) dS + 2k_0 n_0 \iint_S [(k_0(n_j - n_k) - (\beta_j - \beta_k)) \bar{E}_k \cdot \bar{E}_j] dS \quad (26)$$

$k \neq j = 1, \dots, N$

Green's theorem and the fact that the fields  $\bar{E}_j$  and  $\bar{E}_k$  are continuous and decay exponentially away from the waveguide can be applied to conclude that the first integral in (26) is zero. Then, from (26), and the definitions of the coupling coefficient and the overlap integral, (8) and (9), we find:

$$\kappa_{kj} - \kappa_{jk} = (\beta_j - \beta_k) \rho_{jk} \quad (27)$$

In matrix notation this can be written as



$$K^T - K = BR - RB \quad (28)$$

The orthogonality condition between any two supermodes  $\hat{E}_j$  and  $\hat{E}_k$  is given by

$$\sum_{m,n} \hat{E}_{jm}^* \hat{E}_{kn} \iint_S \vec{E}_k(x,y) \cdot \vec{E}_j(x,y) dS = \sum_{m,n} \hat{E}_{jm}^* \rho_{mn} \hat{E}_{kn} = 0 \quad (29)$$

which can be expressed in matrix notation as

$$\hat{E}_j^{\cong} R \hat{E}_k = 0 \quad (30)$$

where the superscript  $\cong$  denotes hermitian conjugate, i.e.,  $[A^{\cong}]_{ij} \equiv A_{ji}^*$ .

By defining the proper inner product<sup>1</sup>,

$$\langle a, b \rangle = a^{\cong} R b \quad (31)$$

where the matrix  $R$  is usually referred to as the metric, equation (31) can also be written as

$$\langle \hat{E}_j, \hat{E}_k \rangle = 0 \quad (32)$$

It can be shown [12] that the eigenvectors of the system matrix  $H$  in (22) are orthogonal if  $H$  is  $R$ -Hermitian, that is, if  $H$  equals its  $R$ -adjoint,  $H^{\#}$ , which is defined as

$$H^{\#} \equiv R^{-1} H^{\cong} R \quad (33)$$

From (22)  $H^{\#}$  is given by

$$H^{\#} = R^{-1} (B + K^T R^{-1}) R = B + R^{-1} K^T \quad (34)$$

where the fact that  $R$  is symmetric was used. Substitution of (28) in the equation above yields:

$$H^{\#} = H \quad (35)$$

---

<sup>1</sup> An inner product is proper when  $\langle a, a \rangle$  is real and positive for any  $a$  except the null vector.

This is always satisfied in an expression like (31) providing the matrix  $R$  is Hermitian and positive definite.

Thus, the supermodes are orthogonal.

### 3) Power conservation.

The total power flow along the structure is given by:

$$P = \sum_k P_k = \sum_k |\hat{A}_k|^2 \langle \hat{E}_k, \hat{E}_k \rangle \quad (36)$$

where  $P_k$  is the power carried by each supermode. The principle of power conservation implies that the power remain the same at any position along the direction of propagation, that is,

$$\frac{dP_k}{dz} = 0 \quad (37)$$

The requirement of power conservation, (37), again imposes the condition that the system matrix  $H$  be  $R$ -Hermitian. This can be shown using (36) and (21):

$$\begin{aligned} \frac{dP_k}{dz} &= \frac{d\hat{E}_k}{dz} R \hat{E}_k + \hat{E}_k R \frac{d\hat{E}_k}{dz} = \\ &= i\hat{E}_k (H^+ R - HR) \hat{E}_k = 0 \end{aligned} \quad (38)$$

## V.1.3.B Grating-assisted coupling among modes in one multimode waveguide.

### 1) Supermodes.

When the perturbed modes are confined in one waveguide, then the unperturbed waveguide modes are orthogonal, and as a consequence the overlap integrals are  $\rho_{jj} = 1$  and  $\rho_{j \neq k} = 0$ . In addition, from (15),  $\kappa_{jk} = \kappa_{kj}$ . Thus, (18) simplifies to:

$$i \frac{da_j}{dz} = \delta_j a_j + \sum_k s_k \kappa_{jk} a_k e^{-i(\delta_{jk} - \delta_k + \delta_j)z} \quad (39)$$

If the number of coupling coefficients,  $\kappa_{jk}$ , different from zero is less than or equal to the number of modes,  $N$ , which is always satisfied for bimodal or trimodal structures, the reference detunings,  $\delta_i$ , can be chosen so that

$$\delta_{jk} - \delta_k + \delta_j = 0 \quad (40)$$

Otherwise, the coupling term includes a linear phase.

Equation (40) is actually valid for many cases of interest, and will be assumed to be satisfied in the following. Using (40), the coupled mode equations (39) can be written in matrix notation as

$$i \frac{da}{dz} = (D + KS)a \quad (41)$$

where  $D$  and  $S$  are diagonal matrices where the diagonal elements are the reference detunings,  $[D]_{kk} = \delta_k$ , and the sign indicating direction of power flux,  $[S]_{kk} = s_k$ , respectively.

Equation (41) can also be expressed as in (21) where the system matrix  $H$  in this case is given by

$$H = D + KS \quad (42)$$

For adiabatic transitions, it can be assumed that the mode amplitudes evolve as in (23) resulting in the eigenvalue equation (24). Solution of this equation yields, as before, the supermodes and their propagation constants.

## 2) Supermode orthogonality and power conservation.

Following a similar approach to that used in section V.1.3.A, a new metric or inner product will be derived in this section from considerations of power flow conservation. However, if there are counterpropagating fields, this inner product is *not* proper, which has important consequences.

The power carrier by each supermode  $\hat{E}_k$  is given by

$$P_k = \hat{E}_k^\dagger S \hat{E}_k = \langle \hat{E}_k, \hat{E}_k \rangle \quad (43)$$

where the inner product is defined as

$$\langle a, b \rangle = a^{\dagger} S b \quad (44)$$

and  $S$  is the metric.  $S$  is a parity matrix consisting of  $\pm 1$  in the main diagonal. Thus, (44) is an improper product, i.e.,  $S$  is indefinite, and the inner product can be a negative number. This would correspond physically to power flowing in the direction of negative  $z$ . Again, power conservation is satisfied provided that  $H$  is  $S$ -Hermitian, which can be shown by direct substitution in (42).

It can be shown [12] that the eigenvalues,  $\hat{\beta}_k$ , of  $S$ -hermitian matrices are either real or else occur in complex conjugate pairs. If  $\hat{\beta}_k$  is the eigenvalue associated with the eigenvector  $\hat{E}_k$ , then  $\hat{E}_k$  is  $S$ -orthogonal to all the other eigenvectors,  $\hat{E}_j$ , with eigenvalue  $\hat{\beta}_j$  different from  $\hat{\beta}_k^*$ , that is

$$\begin{aligned} \langle \hat{E}_k, \hat{E}_j \rangle &= 0 \quad \text{for all } j \text{ such that } \hat{\beta}_k \neq \hat{\beta}_j^* \\ \langle \hat{E}_k, \hat{E}_j \rangle &\neq 0 \quad \text{for } j \text{ such that } \hat{\beta}_k = \hat{\beta}_j^* \end{aligned} \quad (45)$$

Thus, the eigenvector associated with a complex eigenvalue is orthogonal to itself but is not orthogonal to the eigenvector associated with the complex conjugate eigenvalue.

If the eigenvalues are not degenerate, then the eigenvectors form a complete set and any vector can be expressed as a linear combination of them. The coefficients of the linear expansion can be obtained using (68).

## V.2 MODE CONVERSION BETWEEN COPROPAGATING MODES VIA A MEDIATING MODE.

Most current optical couplers and switches are based on coupling between two copropagating modes through some perturbation [13]. This coupling leads to periodic exchange of energy between them along the direction of propagation. The device length can be designed so that complete energy transfer from one waveguide mode to the other

waveguide mode occurs. In practice, however, it is not only difficult to fabricate devices with a specific length, but also the coupling length has a strong wavelength and polarization sensitivity, and this renders the device polarization sensitive, with large insertion loss and crosstalk and narrow-band.

Here, a new scheme of mode conversion between two copropagating modes using a mediating mode is analyzed [14], which overcomes some of the previous limitations. The device has two coupling regions. The first region couples the output mode and the mediating mode, and the second one couples the mediating mode and the input mode (see Figure 1 and Figure 2). Under some conditions, as described below, all the energy in the input mode can be transferred to the output mode, with no energy loss to the mediating mode. This idea of using “counterintuitive” coupling, where the name comes from the order of the coupling regions, has been borrowed from the stimulated Raman process in three level systems [15]. There, the coupling mechanism is a temporal perturbation that couples two populations. An analogy can be established between the temporal populations and the spatial waveguide modes. In our case, the perturbation is a spatial variation of the refractive index.

In this mode converter, the precise length of the coupling regions is not critical, which facilitates fabrication and improves the conversion efficiency. Also, stronger coupling coefficients and/or longer coupling regions always improve coupling and, in the case of adiabatic transitions, help ensure that the adiabaticity condition is satisfied. Thus, if the coupling coefficients are strong enough to produce enough coupling between both optical polarizations, the device would be polarization insensitive. In the case of adiabatic coupling between phase-matched modes (usually travelling in identical waveguides), broadband operation can be achieved as long as the coupling coefficient is strong enough to ensure adiabatic coupling in the desired wavelength range.

The coupling can be achieved through evanescent fields in adjacent waveguides or assisted by a perturbation or grating. The mediating mode can be copropagating or counterpropagating with the input and output modes. In addition, two modes of operation are possible depending on whether the coupling coefficients vary slowly

along the structure (adiabatic coupling coefficients) or the transition between coupling and non-coupling regions is abrupt (non-adiabatic coupling coefficients).

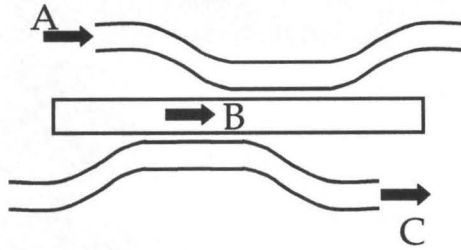


**Figure 1: Adiabatic mode converter in adjacent waveguides through the evanescent fields.**

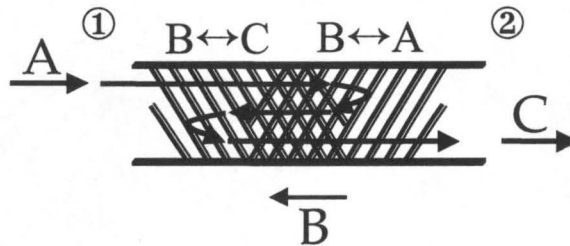


**Figure 2: Mode converter mediated by backward Bragg scattering.**

In section V.2.1 the principle of operation of the proposed three-mode structure is explained using the supermode theory introduced in V.1. Then, two examples are more fully developed. First, in section V.2.2 the mediating mode copropagates with input and output mode and it can only operate in the adiabatic regime. On the contrary, in the device presented in section V.2.3 mode conversion is mediated by a backward propagating mode, where the coupling is grating-assisted. For the effective operation of this device adiabatic transitions are not required.

### V.2.1 Principle of operation.

Coupling between three modes is realized through two coupling regions (see Figure 1 and Figure 2). The first region couples the output mode (mode C) and the mediating mode (mode B), and the second one couples the mediating mode (mode B) and the input mode (mode A). Modes A and C are forward propagating, whereas mode B can be forward (Figure 1) or backward (Figure 2) propagating. The optical field can be expressed as a mode superposition as in (5), where the mode amplitudes are described by coupled-wave equations as in (21), and the system matrix  $H$  can be expressed as

$$H = \begin{bmatrix} 0 & \pm \kappa_{ab} & 0 \\ \kappa_{ba} & \delta_b & \kappa_{bc} \\ 0 & \pm \kappa_{cb} & \delta_c \end{bmatrix} \quad (46)$$

The upper sign corresponds to mode B forward propagating and the lower sign for B backward propagating. In (46) it was assumed that the overlap coefficients,  $\rho_{j \neq k}$ , and the self-coupling coefficients,  $\kappa_{kk}$ , are negligible. In (21),  $a = [a_A \ a_B \ a_C]^T$  and  $a_i$  for  $i = A, B, C$  are the mode amplitudes for the respective modes. The reference detuning  $\delta_a$  was arbitrarily set to zero so that from (40),

$$\begin{aligned} \delta_b &= -2\delta_{ab} \\ \delta_c &= -2(\delta_{ab} - \delta_{cb}) \end{aligned} \quad (47)$$

In order to find the eigenvalues of  $H$ , the following characteristic equation has to be solved:

$$\hat{\beta}^3 - \hat{\beta}^2(\delta_b + \delta_c) + \hat{\beta}(\delta_b\delta_c \pm \kappa_{ab}\kappa_{ba} \pm \kappa_{cb}\kappa_{bc}) \mp \delta_c\kappa_{ab}\kappa_{ba} = 0 \quad (48)$$

Although an analytic solution exists in the general case, it is very involved and difficult to interpret. Here only the important case of  $\delta_c = 0$  is considered, i.e., modes A and C are phase-matched. In this case, which will be denoted as *two-photon resonance*, the eigenvalues are given by

$$\begin{aligned}
\hat{\beta}_0 &= 0 \\
\hat{\beta}_+ &= \frac{\delta_b}{2} + \sqrt{\left(\frac{\delta_b}{2}\right)^2 \pm \kappa_0^2} \\
\hat{\beta}_- &= \frac{\delta_b}{2} - \sqrt{\left(\frac{\delta_b}{2}\right)^2 \pm \kappa_0^2}
\end{aligned} \tag{49}$$

where  $\kappa_o^2 = \kappa_{ab}\kappa_{ba} + \kappa_{cb}\kappa_{bc}$ . The corresponding unnormalized eigenmodes, or supermodes, are given by:

$$\hat{E}_i = \left[ \pm \kappa_{ab} \quad \hat{\beta}_i \quad \pm \kappa_{cb} \right]^T \quad \text{where } i = 0, +, - \tag{50}$$

If a "canonical basis" is defined in terms of the uncoupled waveguide modes:

$$E_A = \begin{bmatrix} 1 \\ 0 \\ 0 \end{bmatrix}, \quad E_B = \begin{bmatrix} 0 \\ 1 \\ 0 \end{bmatrix}, \quad E_C = \begin{bmatrix} 0 \\ 0 \\ 1 \end{bmatrix} \tag{51}$$

then, the normalized supermode corresponding to the zero eigenvalue,  $\hat{E}_0$ , is given by:

$$\hat{E}_0 = \frac{1}{\sqrt{\kappa_{ab}^2 + \kappa_{cb}^2}} (\pm \kappa_{ab} E_A \mp \kappa_{cb} E_C) \tag{52}$$

For the "counterintuitive" coupling sequence in the device here considered, we have

$$\begin{aligned}
\lim_{z \rightarrow -\infty} \frac{\kappa_{ab}(z)}{\kappa_{cb}(z)} = 0 &\Rightarrow \hat{E}_0 \rightarrow E_A \quad \text{for } z \rightarrow -\infty \\
\lim_{z \rightarrow +\infty} \frac{\kappa_{cb}(z)}{\kappa_{ab}(z)} = 0 &\Rightarrow \hat{E}_0 \rightarrow E_C \quad \text{for } z \rightarrow +\infty
\end{aligned} \tag{53}$$

The analysis above enables us to predict the behavior of the device in the adiabatic regime. At the input, and according to Figure 1 and Figure 2,  $\kappa_{ab}$  tends to zero, and if the canonical mode  $E_A$  is incident in the mode converter, then the supermode  $\hat{E}_0$  will be excited. The supermode  $\hat{E}_0$  corresponds to eigenvalue zero, so in the adiabatic approximation, if excited initially, it will propagate along the structure unperturbed. Thus, provided that the  $z$ -dependent perturbation is introduced slowly enough, the



energy remains in the supermode  $\hat{E}_0$ , and is adiabatically transferred totally to the waveguide mode  $E_C$ , with  $E_B$  not being ever excited. This is true regardless of the possible phase mismatch between  $E_B$  and  $E_A$  and between  $E_B$  and  $E_C$ . We notice that the process does not depend on the behavior of  $\lim_{z \rightarrow -\infty} \kappa_{cb}(z)$  and  $\lim_{z \rightarrow -\infty} \kappa_{ab}(z)$ , since these coefficients couple modes that ideally have not been excited. If  $E_A$  and  $E_C$  are not phase-matched, the eigenvalue  $\hat{\beta}_0$  does not equal zero. For the effective operation of the device, the coupling regions have to overlap in space.

## V.2.2 Adiabatic mode conversion mediated by a forward propagating mode.

### V.2.2.A Theory.

Many technologically important optical devices such as optical couplers, switches and modulators are based on the transfer of energy between two optical waveguides that are sufficiently close to each other so that the optical fields overlap in some region. Since the required coupling length for complete transfer of energy usually has a strong dependence on both the wavelength and the polarization, the above device may only operate in a narrow band and has a strong polarization sensitivity, large insertion loss and cross-talk.

Adiabatic waveguide transitions, i.e., transitions that take place gradually with propagation distance, have already been used successfully to overcome these limitations [10]. Figure 1 illustrates a new type of adiabatic coupler that consists of three waveguide and two adiabatic coupling regions. The waveguide C has a segment close to the waveguide B to allow evanescent coupling therebetween to form the first coupling region. Similarly, the waveguide A has a segment close to a second portion of the waveguide B to form the second coupling region. These two coupling regions partially overlap. If the coupling regions satisfy the adiabatic condition, and if the waveguides A

and C are phase-matched, all the energy in the waveguide A can be transferred to the waveguide C, and the mode in waveguide B is never excited. No phase-matching between A and B or between B and C is required to achieve complete energy transfer between A and C.

The coupled mode theory of this type of structure was developed in section V.1.3.A. There it was argued that the waveguide modes are not orthogonal, and the non-zero overlap coefficients should be taken into account. However, as a first approximation,  $\rho_{j \neq k}$  and  $\kappa_{kk}$  can be neglected, and thus  $R$  equals the identity matrix. Also, it will be assumed that  $\kappa_{jk} = \kappa_{kj}$ . This is not necessary but it greatly simplifies the notation and does not change the conclusions qualitatively.

With the simplifications above, this problem is the exact spatial analogy of the stimulated Raman process in three level systems [15]. The eigenmodes at and off resonance can be found in [16], [17].

### V.2.2.B On the adiabaticity condition.

Since the devices and phenomena considered in this section depend on adiabatic transitions, it is important to understand the adiabaticity. This can be evaluated by introducing a higher-order correction to the system matrix describing the evolution of the adiabatic eigenmodes.

The total field is given by:

$$\vec{E}(x, y, z, t) = \begin{bmatrix} \vec{E}_+(x, y) & \vec{E}_0(x, y) & \vec{E}_-(x, y) \end{bmatrix} \begin{bmatrix} | & | & | \\ \hat{E}_+ & \hat{E}_0 & \hat{E}_- \\ | & | & | \end{bmatrix} \begin{bmatrix} \hat{a}_+ \\ \hat{a}_0 \\ \hat{a}_- \end{bmatrix} e^{i\omega t} \quad (54)$$

Here, the matrix  $\hat{E}$ , defined as:

$$\hat{E} = \begin{bmatrix} | & | & | \\ \hat{E}_+ & \hat{E}_0 & \hat{E}_- \\ | & | & | \end{bmatrix} \quad (55)$$

is the matrix containing the eigenmodes and the vector  $\hat{a} = [\hat{a}_+ \quad \hat{a}_0 \quad \hat{a}_-]^T$  contains the amplitudes of the eigenmodes.

The system matrix  $H$  can be transformed from the canonical basis to the basis composed of the adiabatic supermodes. Let the vector  $\hat{b}$  be

$$\hat{b} = \hat{E} \hat{a} \quad (56)$$

Then, using (21)

$$i \frac{d\hat{b}}{dz} = H\hat{b} = i \frac{d\hat{E}}{dz} \hat{a} + i\hat{E} \frac{d\hat{a}}{dz} \quad (57)$$

From the equation above, the mode amplitudes  $\hat{a}_0$  and  $\hat{a}_\pm$  satisfy the equation:

$$i \frac{d\hat{a}}{dz} = H_{ad} \hat{a} \quad (58)$$

where the adiabatic system matrix,  $H_{ad}$ , is given by

$$H_{ad} = \hat{E}^{-1} H \hat{E} - i \hat{E}^{-1} \frac{d}{dz} \hat{E} = \hat{B} - i \hat{E}^{-1} \frac{d}{dz} \hat{E} \quad (59)$$

Here,  $\hat{B}$  is a diagonal matrix with the eigenvalues in the main diagonal,  $[\hat{\beta}_+ \quad \hat{\beta}_0 \quad \hat{\beta}_-]$ .

The adiabatic system matrix  $H_{ad}$  can be obtained by substitution of the eigenmodes and eigenvalues in (59) and is given by [16]

$$H_{ad} = \begin{bmatrix} \kappa_0 \cot \varphi & i\dot{\theta} \sin \varphi & i\dot{\varphi} \\ -i\dot{\theta} \sin \varphi & 0 & -i\dot{\theta} \cos \varphi \\ -i\dot{\varphi} & i\dot{\theta} \cos \varphi & -\kappa_0 \tan \varphi \end{bmatrix} \quad (60)$$

where the angles  $\varphi$  and  $\theta$  are defined as

$$\tan \theta = \frac{\kappa_{ab}}{\kappa_{cb}} \quad (61)$$

$$\tan 2\varphi = \frac{2\kappa_0}{\delta_b} \quad (62)$$

Adiabatic evolution takes place if the adiabatic supermode  $\hat{E}_0$  is effectively decoupled from the other two adiabatic supermodes  $\hat{E}_+$  and  $\hat{E}_-$ . According to equation (60), this will be the case if the non-diagonal elements involving  $\dot{\theta}$  are small compared to the non-zero terms in the diagonal. On resonance,  $\varphi = \pi/4$ , and the adiabaticity condition takes the simple form

$$|\dot{\theta}| \ll \kappa_0 \quad (63)$$

From (61),

$$\dot{\theta} = \frac{\dot{\kappa}_{ab}\kappa_{cb} - \dot{\kappa}_{cb}\kappa_{ab}}{\kappa_0^2} \quad (64)$$

Then, the adiabaticity condition becomes:

$$\left| \frac{\dot{\kappa}_{ab}\kappa_{cb}}{\kappa_0^2} - \frac{\dot{\kappa}_{cb}\kappa_{ab}}{\kappa_0^2} \right| \ll \kappa_0 \quad (65)$$

If the two coupling coefficients are roughly of equal magnitude, then  $\dot{\theta}$  is independent of the coupling coefficient amplitude and inversely proportional to the speed of spatial variation of the coupling coefficients. Then, the adiabaticity condition is satisfied if the total area of the coupling coefficients is large enough and the relative change with  $z$  is smooth enough.

As the detuning increases,  $\varphi$  is not constant, and the adiabaticity condition becomes more restrictive and the adiabatic approximation is increasingly less valid.

### V.2.2.C Simulation.

One of the advantages of the scheme here presented over existing devices is the flexibility in coupling coefficient profile. As long as the coupling coefficients follow a "counterintuitive" sequence, and the adiabaticity condition is satisfied, efficient transfer of power is achieved. Figure 3 displays the power in the different modes at the output of the device for two different choices of coupling coefficients and a function of the detuning between A and B, with A and C on resonance (the plots are symmetric for

negative detuning between A and B). The coupling coefficients are normalized so as to have same area, defined as  $Area = \int_0^L \kappa_{cb} dz$ , in both cases. The shape of  $\kappa_{cb}$  and  $\kappa_{ab}$  is the same. In addition, in both cases,  $\kappa_{cb}$  is nearly zero at the point where  $\kappa_{ab}$  is maximum and vice versa. In the left column, the coupling coefficient is a supergaussian,  $\kappa_{cb} \propto \exp(-az^4)$ , and in the right column the coupling coefficient is  $\kappa_{cb} \propto \cos^2(az)$ . In Figure 3 it can be observed that, even though the coupling coefficients are substantially different, the mode power transfer is nearly the same. In addition, the analysis presented above remains valid even at large values of detuning between A and B, indicating that only A and C need to be on resonance.

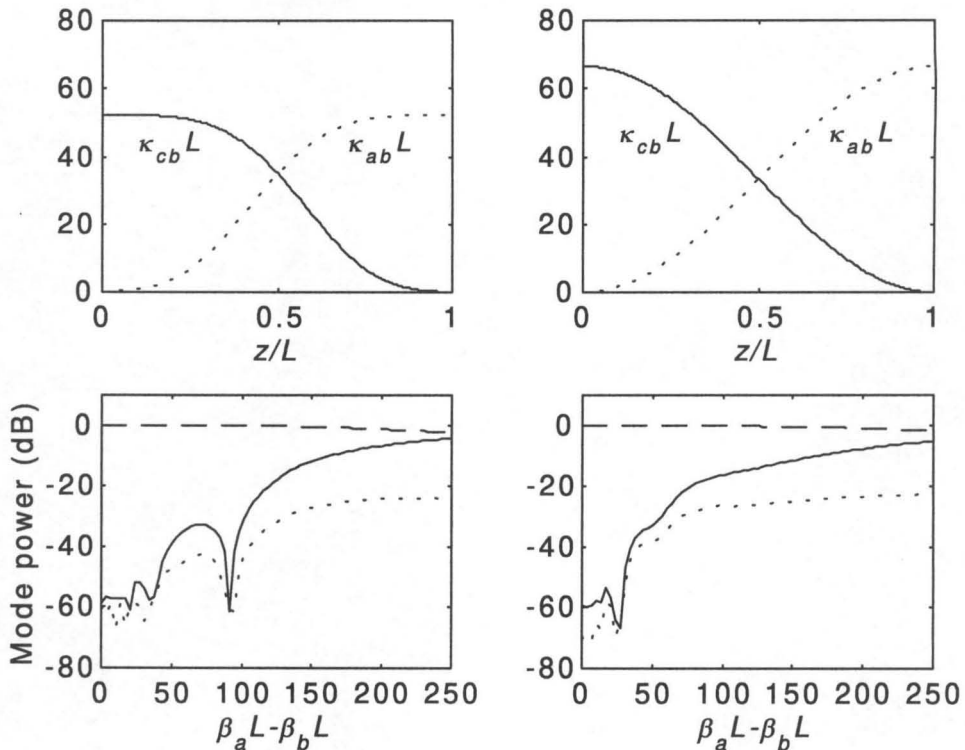


Figure 3: Mode power (bottom plots) on two-photon resonance, i.e.,  $\beta_a = \beta_c$ , as a function of the detuning between mode A and B for the two coupling coefficients displayed in the upper plots. Input mode A is solid, mediating mode B is dotted and output mode C is dashed curve.

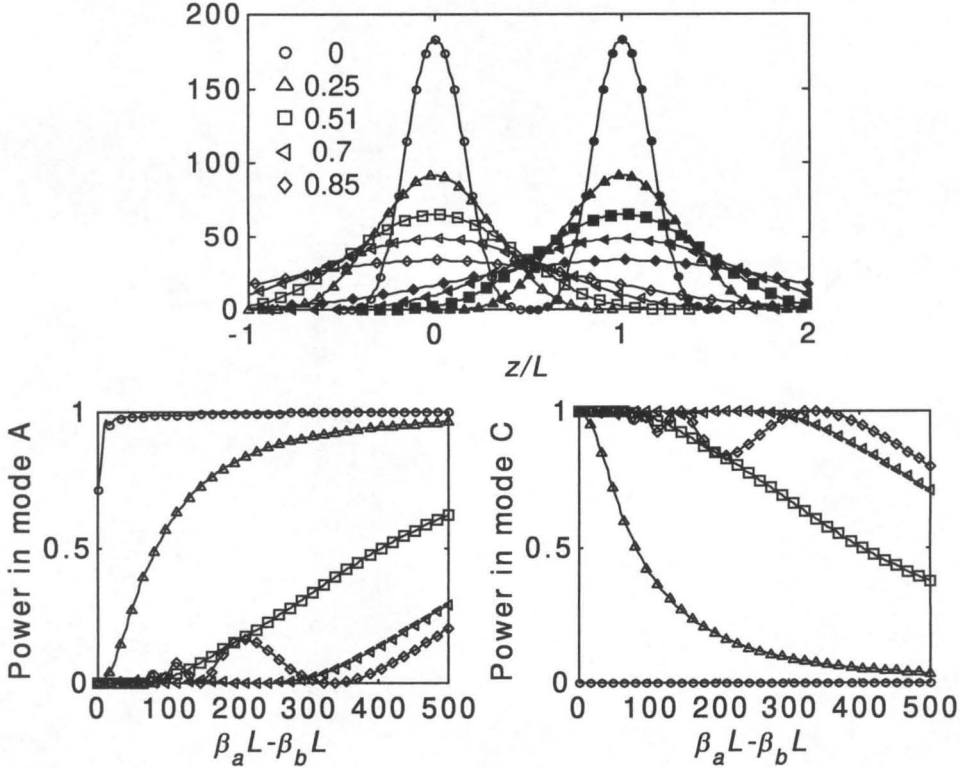


Figure 4: Power in input mode A (bottom left) and output mode C (bottom right) on two-photon resonance, i.e.,  $\beta_a = \beta_c$ , as a function of the detuning between mode A and B for the coupling coefficients displayed in the upper plot. All coupling coefficients have same shape and area, but different overlap. The number in the upper plot is the ratio between  $\kappa_{cb}$  and  $\kappa_{ab}$  at the point where  $\kappa_{ab}$  is maximum for the different coupling coefficients.

An important parameter for ensuring proper operation of the device is the overlap between  $\kappa_{cb}$  and  $\kappa_{ab}$ . It is required that  $\kappa_{cb}$  and  $\kappa_{ab}$  overlap to some extent, and the degree to which they overlap might affect the device performance. Figure 4 shows the power in input and output modes at two-photon resonance as a function of the detuning between A and B for several coupling coefficients.  $\kappa_{cb}$  and  $\kappa_{ab}$  have the

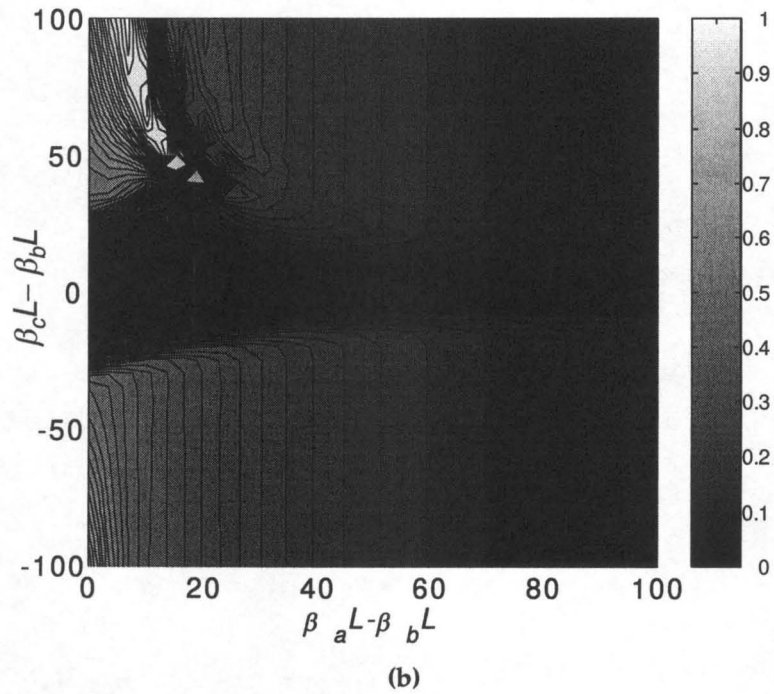
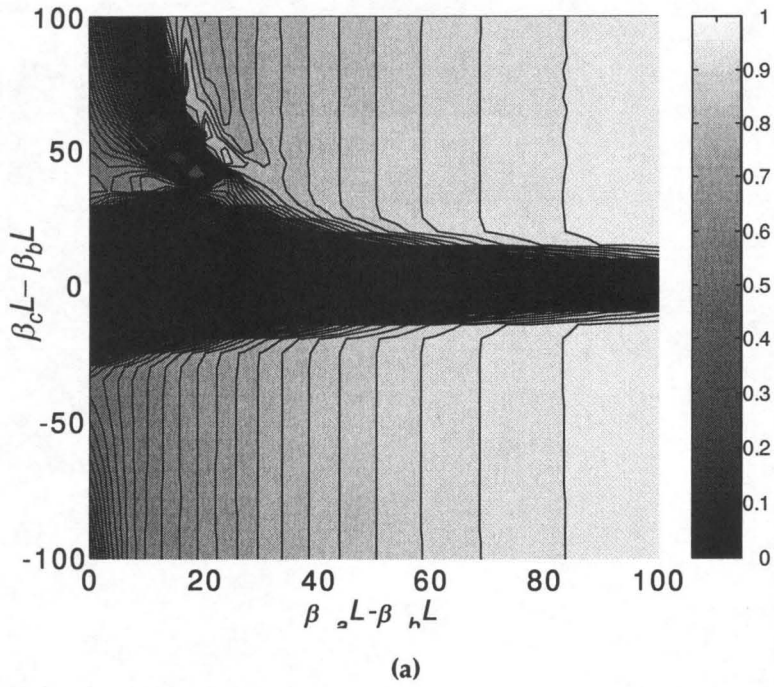
same shape and  $\kappa_{cb} \propto \cos^4(az)$ . The value of  $a$  is different in each case and determines the amount of overlap. The coupling coefficients in all cases are normalized so as to have same area. The number in the upper plot indicates the ratio between  $\kappa_{cb}$  and  $\kappa_{ab}$  at the point where  $\kappa_{ab}$  is maximum for the different values of  $a$ . It can be observed that when the coupling coefficients do not overlap (circles), there is not power transfer to mode C, which remains zero even on full resonance  $\beta_A = \beta_B = \beta_C$ . As the overlap between  $\kappa_{cb}$  and  $\kappa_{ab}$  increases, the power transfer efficiency improves, and the allowable detuning between modes A and B (or equivalently C and B) increases. When the overlap becomes very large,  $\kappa_{cb}$  has a non-negligible value at the point where  $\kappa_{ab}$  reaches its maximum. As a consequence, the limits in (53) are less valid, and the power transfer exhibits an oscillatory behavior (diamonds) that becomes worse as the overlap increases (or equivalently the ratio between  $\kappa_{cb}$  and  $\kappa_{ab}$  at the point where  $\kappa_{ab}$  is maximum increases).

The detailed frequency dependence of the mode power at the device output has been depicted in Figure 5. The gray scale indicates the mode power and the horizontal and vertical axes are the detunings between A and B and between A and C, respectively. These plots have been calculated for the coupling coefficient on the left upper plot in Figure 3. It is observed that as the detuning between A and B (or equivalently C and B) increases, the device becomes narrow-band in the sense that a small detuning between modes A and C can spoil the mode conversion.

This is further observed in Figure 6, which illustrates the power in modes A (circles), B (triangles) and C (squares) on two-photon resonance, i.e., modes A and C phase-matched, (empty markers) compared to that for some detuning between A and C (solid markers). On two-photon resonance, the power in mode A is efficiently transferred to mode C even for large detunings between A and B. However, if all three modes are detuned, then the power transfer is spoiled and the power remains mainly in



mode A with some loss to mode B, which decreases as the detuning between A and B is raised.





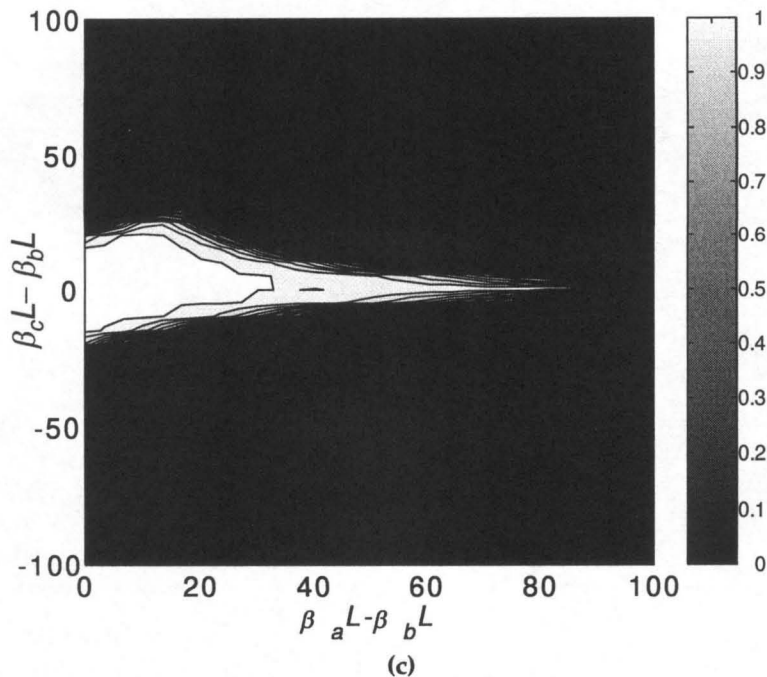


**Figure 5:** Contour plots of mode power in input mode A (a), mediating mode B (b) and output mode C (c) as a function of detuning between A and B (horizontal axis) and detuning between A and C (vertical axis).

The frequency behavior outlined above can be used to an advantage in a variety of applications. Two of these will be described in the following.

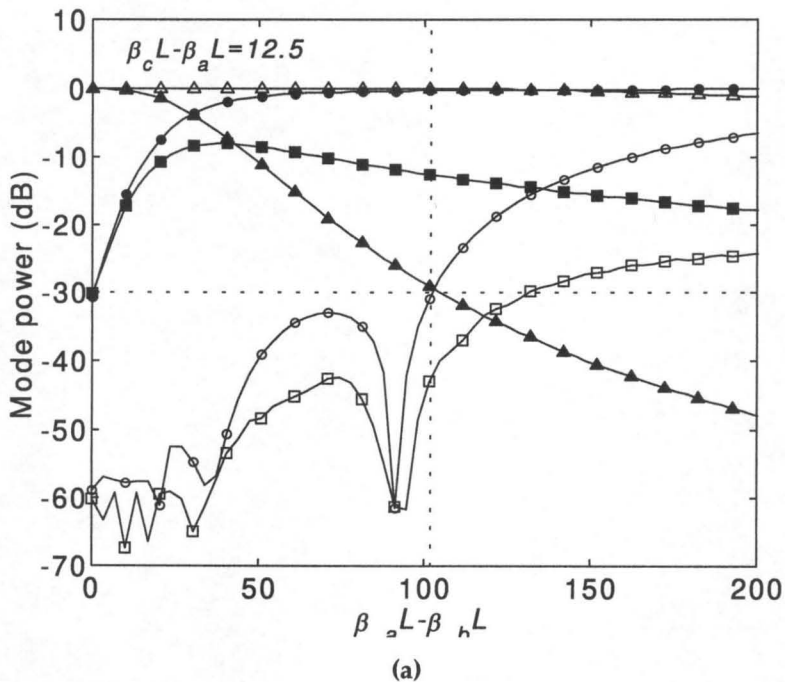
### 1) *Optical switch*

An optical switch with low insertion loss and cross-talk can be realized using the mode conversion mechanism here presented. The middle waveguide, corresponding to mode B, should have different propagation constant than the input and output waveguides, which can be achieved by proper design of waveguide dimensions and index of refraction profiles. The input and output waveguides should be identical in order to be phase-matched.

According to the previous discussion, even for some detuning between A and B, efficient energy transfer occurs from input to output mode. In addition, with a relatively

small change in the propagation constant of mode C, which could be achieved through some nonlinear phenomenon, the mode conversion would be spoilt. For instance, if a system requirement is that the cross-talk is less than 30dB, then, as shown in Figure 6 with the dotted lines, detunings  $\beta_a L - \beta_b L \approx 100$  and  $\beta_c L - \beta_a L \geq 12.5$  are required. There is some insertion loss ( $< .5\text{dB}$ ) of power transferred to mode B, but which does not result in cross-talk.

This type of mode conversion has an additional advantage over other devices. Since there is no coupling between input and output modes, the loss that can accompany the change in refractive index in the cross-state, does not affect the input mode, which travels unaffected. In addition, all other benefits of adiabatic structures such as low polarization sensitivity also apply. The optical switch will be broadband if the detuning between A and C is large enough at all wavelengths of interest.



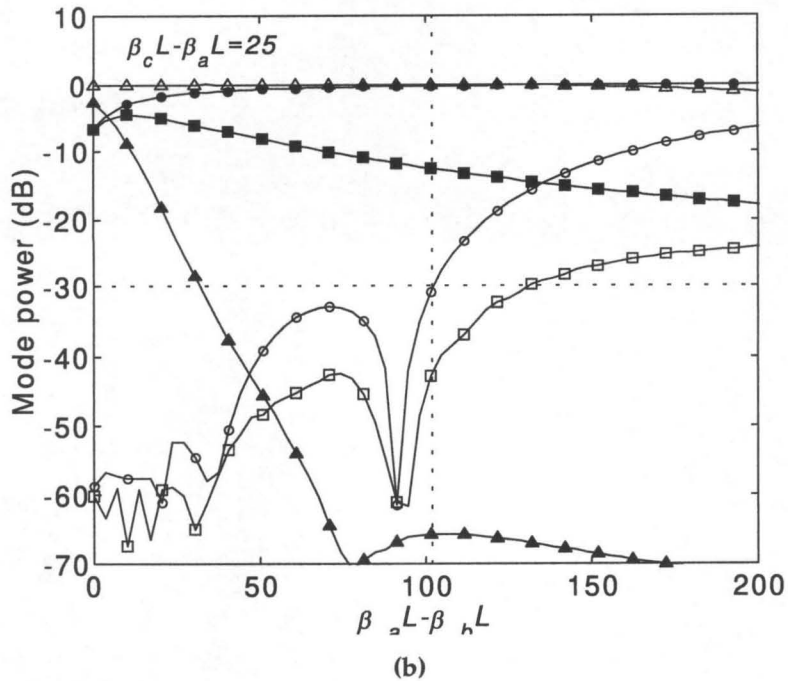


Figure 6: Mode power in modes A (circles), B (triangles) and C (squares) for  $\beta_a = \beta_c$  (empty), and  $\beta_a \neq \beta_c$  (solid). (a) is for  $\beta_c L - \beta_a L = 12.5$  and (b) is for  $\beta_c L - \beta_a L = 25$ . The coupling coefficients are those on the left upper plot in Figure 3.

## 2) Wavelength-selective coupler

Recent applications require devices that couple light from one waveguide to another over a specific wavelength band, but leave the rest of the spectrum unaffected. Some of these include wavelength-division-multiplexing of the transmission bands at 1310nm and 1550nm, and demultiplexers of pump and signal waves for erbium-doped fiber amplifiers. Most of the current designs use coupling between two dissimilar waveguides. This approach suffers from the same drawbacks mentioned before such as polarization sensitivity and poor efficiency. In addition, since the coupling efficiency varies sinusoidally with wavelength, it is difficult to nullify the coupling outside the band of interest, and the cross-talk can be significant.

Using three dissimilar waveguides, the refractive index profile and waveguide dimensions can be chosen so that waveguides A and C are only phase-matched at the band of interest. Outside this band, waveguides A, B and C are not phase-matched and no coupling occurs, leaving the input mode unaffected. As before, this device would exhibit low polarization sensitivity, low cross-talk and good coupling efficiency.

### V.2.3 Non-adiabatic mode conversion mediated by a Bragg backward propagating mode.

#### V.2.3.A Theory.

The structure of the mode converter is shown in Figure 2. The device should be fabricated in a waveguide that supports three propagating modes. In this case, adiabatic coupling is not required, and the principle of operation can be explained as follows. When mode A is incident on port ①, it travels forward unaffected by the first grating. When mode A reaches the second grating, it is reflected back into mode B. Mode B then travels backward and reaches the first grating, where it is reflected back into mode C. Mode C travels forward along the second grating, which has no effect on it. As a result mode C emerges from port ②. In addition, if mode C were incident on port ①, it would be very strongly reflected.

Since efficient coupling only occurs at the Bragg-wavelength, this device is narrow-band. If the coupling coefficients are strong enough to produce enough coupling between both optical polarizations, the device would be polarization insensitive.

The system matrix associated with this device is given by:

$$H = \begin{bmatrix} 0 & \kappa_{ab} & 0 \\ -\kappa_{ab}^* & \delta_b & -\kappa_{cb}^* \\ 0 & \kappa_{cb} & \delta_c \end{bmatrix} \quad (66)$$

One of these eigenvalues,  $\hat{\beta}_0$ , is always real, whereas the other two,  $\hat{\beta}_\pm$ , can be complex conjugate, inside the so-called forbidden region, or both real, outside of the forbidden region. On the boundary the two supermodes  $\hat{E}_\pm$  are degenerate.

The eigenvectors are given by

$$\hat{E}_i = \left[ \begin{array}{c} \hat{\beta}_i \\ \kappa_{ab} \end{array} \frac{-|\kappa_{ab}|^2 + (\delta_b - \hat{\beta}_i)\hat{\beta}_i}{\kappa_{cb}^*} \right]^T \quad \text{where } i = 0, +, - \quad (67)$$

In consideration of the discussion in section V.1.3.B, inside the forbidden region the eigenvectors  $\hat{E}_0$  and  $\hat{E}_\pm$  can be normalized so as to satisfy the following orthonormality relations:

$$\begin{aligned} \langle \hat{E}_0, \hat{E}_\pm \rangle &= 0, & \langle \hat{E}_0, \hat{E}_0 \rangle &= 1 \\ \langle \hat{E}_\pm, \hat{E}_\pm \rangle &= 0, & \langle \hat{E}_\pm, \hat{E}_\mp \rangle &= 1 \end{aligned} \quad (68)$$

whereas outside of the forbidden region

$$\begin{aligned} \langle \hat{E}_0, \hat{E}_\pm \rangle &= 0, & \langle \hat{E}_0, \hat{E}_0 \rangle &= 1 \\ \langle \hat{E}_\pm, \hat{E}_\mp \rangle &= 0, & \langle \hat{E}_\pm, \hat{E}_\pm \rangle &= 1 \end{aligned} \quad (69)$$

On the boundary, the eigenvalues are degenerate, and the eigenvectors do not form a complete set.

The characteristic equation (48) is a cubic equation that has an analytical solution [18]. If we define the parameters

$$\begin{aligned} p &= \frac{1}{3}(\delta_b \delta_c + |\kappa_{ab}|^2 + |\kappa_{cb}|^2) - \frac{1}{9}(\delta_b + \delta_c)^2 \\ q &= -\frac{1}{27}(\delta_b + \delta_c)^3 + \frac{1}{6}(\delta_b + \delta_c)(\delta_b \delta_c + |\kappa_{ab}|^2 + |\kappa_{cb}|^2) - \frac{1}{2}\delta_c |\kappa_{ab}|^2 \end{aligned} \quad (70)$$

then the discriminant is given by  $q^2 + p^3$ . If the discriminant is positive, then one root is real and two are complex conjugates. If the discriminant is zero, then there are three real roots, of which at least two are equal. If the discriminant is negative, then there are three

unequal real roots. Thus the equation  $q^2 + p^3 = 0$  describes the boundary of the forbidden region. The eigenvalues are given by

$$\begin{aligned}\hat{\beta}_0 &= \frac{1}{3}(\delta_b + \delta_c) + \lambda_+ \\ \hat{\beta}_\pm &= \frac{1}{3}(\delta_b + \delta_c) - \frac{1}{2}\lambda_+ \pm i\frac{\sqrt{3}}{2}\lambda_-\end{aligned}\quad (71)$$

where

$$\lambda_\pm = \left(-q + \sqrt{q^2 + p^3}\right)^{1/3} \pm \left(-q - \sqrt{q^2 + p^3}\right)^{1/3}\quad (72)$$

The eigenvalue  $\hat{\beta}_0$  is always real whereas  $\hat{\beta}_\pm$  are complex conjugate inside the forbidden region, i.e., for  $q^2 + p^3 > 0$ , are real outside of it, and are equal at the boundary.

In the following only the case of *two-photon resonance* is considered, i.e.,  $\delta_c = -2(\delta_{ab} - \delta_{cb}) = 0$ . Further, the analysis will be restricted to the region inside the forbidden gap, that is

$$|\kappa_{ab}|^2 + |\kappa_{cb}|^2 > \left(\frac{\delta_b}{2}\right)^2\quad (73)$$

To simplify notation, it will be assumed that the coupling coefficients,  $\kappa_{ab}$  and  $\kappa_{cb}$ , are real and positive. Normalized parameters can be defined

$$\begin{aligned}r &= \frac{\kappa_{cb}}{\kappa_{ab}} \\ \Delta &= \frac{\delta_b}{2\kappa_{ab}}\end{aligned}\quad (74)$$

so that the eigenvalues take the form

$$\begin{aligned}\hat{\beta}_0 &= 0 \\ \hat{\beta}_\pm &= \kappa_{ab} \left( \Delta \pm i\sqrt{1 + r^2 - \Delta^2} \right)\end{aligned}\quad (75)$$

and the corresponding normalized eigenvectors satisfying (68) are

$$\begin{aligned}\hat{E}_0 &= \frac{1}{\sqrt{1+r^2}} [r \quad 0 \quad -1]^T \\ \hat{E}_\pm &= \frac{e^{\mp i\alpha/2}}{\sqrt{2\cos\alpha}\sqrt{1+r^2}} \begin{bmatrix} 1 & \mp i\sqrt{1+r^2}e^{\pm i\alpha} & r \end{bmatrix}^T\end{aligned}\quad (76)$$

where

$$\sin\alpha = -\frac{\Delta}{\sqrt{1+r^2}}, \quad \alpha \in \left[-\frac{\pi}{2}, \frac{\pi}{2}\right] \quad (77)$$

The “canonical basis” in terms of the uncoupled waveguide modes, (51), will be used. These three vectors are orthogonal and normalized to unity power flow, and correspond to the unperturbed waveguide modes A, B and C. This is an unusual basis in the sense that the power flow associated with the second mode,  $E_B$ , is negative, whereas modes  $E_A$  and  $E_C$  carry positive power flow. The eigenvectors can be expressed as combination of these canonical modes:

$$\begin{aligned}\hat{E}_0 &= \frac{1}{\sqrt{1+r^2}} (rE_A - E_C) \\ \hat{E}_\pm &= \frac{e^{\mp i\alpha/2}}{\sqrt{2\cos\alpha}\sqrt{1+r^2}} (E_A \mp i\sqrt{1+r^2}e^{\pm i\alpha} E_B + rE_C)\end{aligned}\quad (78)$$

The analysis above enables us to predict the behavior of the device in the adiabatic regime. At the input, and according to Figure 2,  $r$  tends to infinity, and if the canonical mode  $E_A$  is incident in the mode converter, then the supermode  $\hat{E}_0$  will be excited. As explained above, in the adiabatic approximation, this mode, if excited initially, will propagate along the structure unperturbed, and the canonical mode  $\hat{E}_C$  will emerge at the output.

### V.2.3.B On the adiabaticity condition.

A similar analysis to that in V.2.2.B will be followed. The matrix  $e$  in (55) can be expressed in a more convenient way by defining the angles  $\theta$  and  $\varphi$  such that:

$$\begin{aligned}\sin\theta &= \frac{1}{\sqrt{1+r^2}}, & \cos\theta &= \frac{r}{\sqrt{1+r^2}} \\ \sin\varphi &= \frac{e^{-i\alpha/2}}{\sqrt{2\cos\alpha}}, & \cos\varphi &= \frac{e^{i\alpha/2}}{\sqrt{2\cos\alpha}}\end{aligned}\quad (79)$$

Thus,

$$\hat{E} = \begin{bmatrix} \sin\theta \sin\varphi & \cos\theta & \sin\theta \cos\varphi \\ -i \cos\varphi & 0 & i \sin\varphi \\ \cos\theta \sin\varphi & -\sin\theta & \cos\theta \cos\varphi \end{bmatrix}\quad (80)$$

This is similar to a rotation with angles  $\theta$  and  $\varphi$ . However, in this case  $\varphi$  is a complex angle, and the transformation is not  $S$ -unitary because, as mentioned above, the canonical modes are not all normalized to the same value.

Using the orthonormality relations (68), it can be shown that

$$\hat{E} \approx S \hat{E} = \tilde{I}\quad (81)$$

where

$$\tilde{I} = \begin{bmatrix} 0 & 0 & 1 \\ 0 & 1 & 0 \\ 1 & 0 & 0 \end{bmatrix}\quad (82)$$

Thus,

$$\hat{E}^{-1} = \tilde{I} \hat{E} \approx \hat{E}\quad (83)$$

and substituting  $\hat{E}$  from (80) we get

$$\hat{E}^{-1} = \begin{bmatrix} \sin\theta \sin\varphi & i \cos\varphi & \cos\theta \sin\varphi \\ \cos\theta & 0 & -\sin\theta \\ \sin\theta \cos\varphi & -i \sin\varphi & \cos\theta \cos\varphi \end{bmatrix}\quad (84)$$

Then, substituting  $\hat{E}$  and  $\hat{E}^{-1}$  in (59), we obtain



$$H_{ad} = i \begin{bmatrix} \kappa_{ab} \frac{-\sin 2\varphi + \cos 2\varphi \cot \varphi}{\sin \theta} & \dot{\theta} \sin \varphi & \dot{\varphi} - \kappa_{ab} \frac{\cos 2\varphi}{\sin \theta} \\ -\dot{\theta} \sin \varphi & 0 & -\dot{\theta} \cos \varphi \\ -\dot{\varphi} - \kappa_{ab} \frac{\cos 2\varphi}{\sin \theta} & \dot{\theta} \cos \varphi & \kappa_{ab} \frac{\sin 2\varphi + \cos 2\varphi \tan \varphi}{\sin \theta} \end{bmatrix} \quad (85)$$

where an overdot indicates derivative with respect to  $z$ .

On resonance the matrix above simplifies to:

$$H_{ad} = \frac{i}{\sqrt{2}} \begin{bmatrix} -\sqrt{2}\kappa_{ab} \cos \epsilon c \theta & \dot{\theta} & 0 \\ -\dot{\theta} & 0 & -\dot{\theta} \\ 0 & \dot{\theta} & \sqrt{2}\kappa_{ab} \cos \epsilon c \theta \end{bmatrix} \quad (86)$$

and the adiabaticity condition takes the simple form:

$$|\dot{\theta}| \ll \frac{\kappa_{ab}}{\sin \theta} \quad (87)$$

or equivalently, substituting  $\theta$  and  $\dot{\theta}$  from (79),

$$\left| \frac{\dot{\kappa}_{cb}}{\kappa_{cb}} - \frac{\dot{\kappa}_{ab}}{\kappa_{ab}} \right| \ll \left( \kappa_{ab}^{2/3} \left( \frac{\kappa_{ab}}{\kappa_{cb}} \right)^{2/3} + \kappa_{cb}^{2/3} \left( \frac{\kappa_{cb}}{\kappa_{ab}} \right)^{2/3} \right)^{3/2} \quad (88)$$

The same conclusions as in section V.2.2.B can be drawn. The adiabaticity condition is satisfied if the area of the coupling coefficient is large enough and the relative change with  $z$  is smooth enough.

### V.2.3.C Simulation.

Most of the conclusions drawn in section V.2.2.C for the case of adiabatic transitions with mode B forward propagating are also valid when mode B is backward propagating. In Figure 7 another example is given. Here, the power in the different waveguide modes has been plotted along the direction of propagation for adiabatic Gaussian-shaped coupling coefficients (shown in the upper plot) with several strengths. As expected, the backward mode, B, is hardly excited. As the magnitude of the coupling coefficient increases, the adiabaticity condition is more valid (as explained in section

V.2.3.B), and the energy transfer to mode B decreases substantially, as well as the mode conversion efficiency improves.

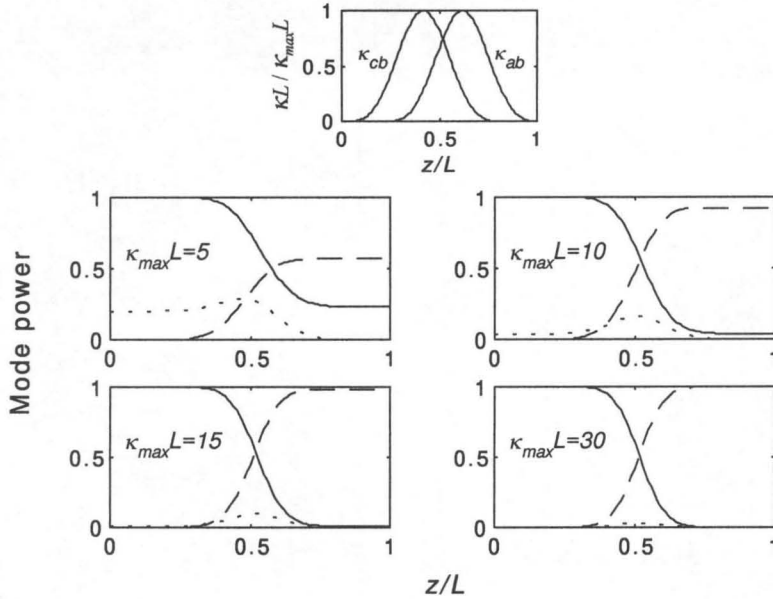


**Figure 7: Spatial evolution of mode power for adiabatic grating-assisted mode converter on resonance for several coupling strengths. Mode A is solid, mode B is dotted and mode C is dashed curve. The upper plot shows the coupling coefficients.**

In the case of uniform coupling coefficients, an analytic solution can be obtained for the propagating field by using the supermodes previously derived. If the two gratings do not overlap completely, three regions are distinct, and the field is a superposition of the supermodes, where the coefficients are found by applying the boundary conditions. Figure 8 shows the reflection coefficient at the input of a device with two overlapping uniform gratings as a function of the frequency deviations,  $\delta_{ab}$  and  $\delta_{cb}$ . The boundary of the forbidden region was calculated by using (70) and the theory in section V.2.3.A, and is shown with a thick solid line. Near resonance for both gratings, the reflection coefficient decreases because part of the input mode A is

converted into mode C. When the first grating that couples B and C is off resonance, there is a large reflection due to the second grating. Inside the forbidden region, the reflection coefficient is expected to be uniform, whereas outside it, all the eigenvalues are real, and the reflectivity has an oscillatory behavior.

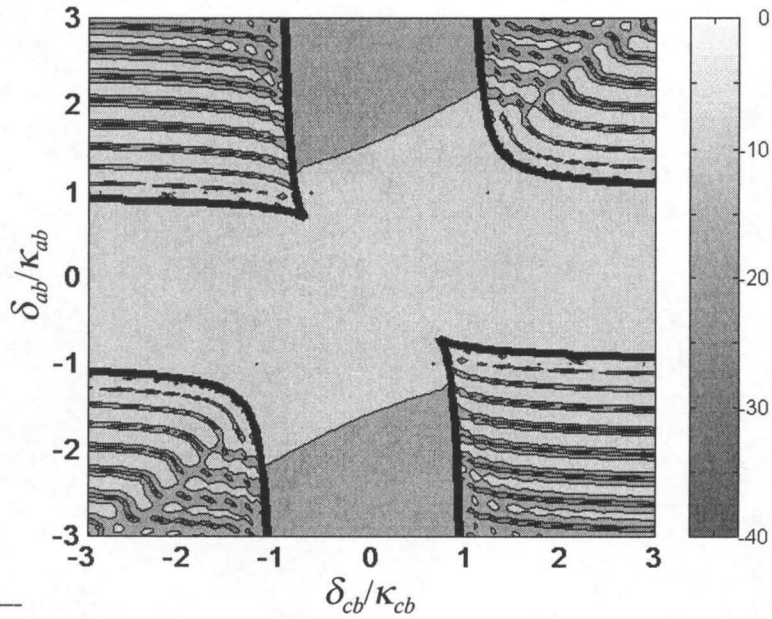


Figure 8: Contour plot of the reflection coefficient (in dB) at the input of a uniform grating-assisted mode converter with  $\kappa_{cb}L = \kappa_{ab}L = 20$ . The thick solid line indicates the boundary of the forbidden region.

## REFERENCES

- [1] A. Yariv, "Coupled Mode Theory for Guided Wave Optics," *IEEE J. Quantum Electron.*, vol. 9, 919 (1973).
- [2] E. Marcatili, "Improved coupled-mode equations for dielectric guides," *IEEE J. Quantum Electron.*, vol. 22, 6, pp. 988-993, Jun., 1986.
- [3] H. Kogelnik, C. V. Shank, "Coupled Wave Theory of Distributed Feedback Lasers," *J. Appl. Phys.*, vol. 43, 2328 (1972).
- [4] G. Meltz, W. W. Morey, W. H. Glenn, "Formation of Bragg gratings in optical fiber by a transverse holographic method," *Opt. Lett.*, vol. 14, 15, pp. 823-825, 1989.
- [5] A. Yariv, *Optical Electronics In Modern Communication*, Fifth Edition, Oxford University Press, New York, Ch. 13.
- [6] E. Kapon, J. Katz, A. Yariv, "Supermode Analysis of Phase-locked Arrays of Semiconductor Lasers," *Opt. Lett.*, vol. 9, 125 (1984).
- [7] P. St. J. Russell, "Bloch Wave Analysis of Dispersion and Pulse Propagation in Distributed Feedback Structures," *J. Modern Opt.*, vol. 38, 1599 (1991).
- [8] E. Peral, J. Capmany, "Generalized Bloch wave analysis for fiber and wave-guide gratings," *J. Lightwave Technol.*, vol. 15, 8, pp. 1295-1302, Aug., 1997.
- [9] A. Yariv, P. Yeh, *Optical Waves In Crystals*, J. Wiley and Sons-Interscience, 1984, Ch. 6.
- [10] A. S. Kewitsch, G. A. Rakuljic, P. A. Willems, A. Yariv, "All Fiber Zero-Insertion Loss Add-Drop Filter for Wavelength-Division Multiplexing," *Opt. Lett.*, vol. 23, 206 (1998).
- [11] D. Marcuse, *Theory of dielectric optical waveguides*, Academic Press, p. 106 (1974).
- [12] M. C. Pease, *Method of matrix algebra*, Academic Press, New York, 1965.
- [13] K. O. Hill, B. Malo, K. A. Vineberg, F. Bilodeau, D. C. Johnson, I. Skinner, "Efficient mode conversion in telecommunication fiber using externally written gratings," *Electron. Lett.*, vol. 26, 16, pp. 1270-1272, Aug., 1990.

- [14] E. Peral, A. Yariv, "Supermodes of grating-coupled multimode waveguides and application to mode conversion between co-propagating modes mediated by backward Bragg scattering," *J. Lightwave Technol.*, 17, 5, pp. 942-947, May 1999.
- [15] U. Gaubatz, P. Rudecki, S. Schiemann, K. Bergmann, "Population transfer between molecular vibrational levels by stimulated Raman scattering with partially overlapping laserfields. A new concept and experimental results.," *J. Chem. Phys.*, vol. 92, 9, pp. 5363-5376, May, 1990.
- [16] T. A. Laine, S. Stenholm, "Adiabatic processes in three-level systems," *Phys. Rev. A*, vol. 53, 4, pp. 2501-2512, Apr., 1996.
- [17] M. P. Fewell, B. W. Shore, K. Bergmann, "Coherent population transfer among three states: full algebraic solutions and the relevance of nonadiabatic processes to transfer delayed pulses," *Aust. J. Phys.*, vol. 50, pp. 281-308, 1997.
- [18] M. Abramowitz, I. Stegun, *Handbook of mathematical functions : with formulas, graphs, and mathematical tables*, Dover, New York, 1976.

